# Theory of Resonant Photoemission in Typical Systems with Strong and Weak Electron Correlation.

Takashi Nakano

DISSERTATION IN PHYSICS

THE OSAKA UNIVERSITY

GRADUATE SCHOOL OF SCIENCE

TOYONAKA, OSAKA

# Theory of Resonant Photoemission in Typical Systems with Strong and Weak Electron Correlation

by

Takashi Nakano

1987

Contents

Abstract

Resonant photoemission spectra in typical systems with strong and weak electron correlation are studied theoretically. As a typical system with strong electron correlation, Ce oxides ($CeO_2$ and $Ce_2O_3$) are studied. The hybridization between a Ce 4f electron and an O 2p electron and the Coulomb correlation between Ce 4f electrons are taken into account. Resonant photoemission spectrum in $\gamma$-Ce, as well as core and valence photoemission spectra in Ce oxides, is also analyzed. As a typical system with weak electron correlation, black phosphorus is studied, where the valence electron correlation is disregarded.

First, the 3d core photoemission spectra, the valence photoemission spectra and the bremsstrahlung isochromat spectra for Ce oxides are theoretically analyzed by use of the impurity Anderson model with a filled valence band. For $CeO_2$, some previous analyses are improved to obtain better agreement with experimental data. For $Ce_2O_3$, recent experimental data are analyzed for the first time. The calculated spectra are in satisfactory agreement with experimental data by choosing appropriately the parameter values in the model. It is found that $Ce_2O_3$ is in the almost trivalent state, whereas $CeO_2$ is in the mixed valence state.

Secondly, resonant photoemission spectra are calculated for Ce oxides. It is shown that the resonant photoemission can be analyzed consistently with the above mentioned various spectra. The agreement between the theoretical and experimental results gives, especially for $Ce_2O_3$, support to our estimation of parameter values. A similar analysis of the resonant photoemission is

also made for Y-Ce.

Thirdly, the resonant photoemission spectra are calculated for black phosphorus by using a realistic density of states of conduction and valence bands and by taking into account the effect of a core hole potential. From comparison of the calculated spectra with recent experimental data, it is shown that a core exciton plays an important role both in Fano type resonance and the enhancement of the Auger electron intensity at the core electron excitation threshold.

## I. General Introduction

Photoemission is a phenomenon in which incident photons are absorbed by a solid (more generally by any materials) and electrons are emitted out of the solid.[1] The first observation of this phenomenon was made in 1887, when Hertz observed that a spark between two electrodes occurs more easily when the negative electrode is illuminated by ultraviolet radiation.[2] Afterward, the electron was discovered by Thomson,[3] and the essential mechanism of photoemission was understood due to the famous theory of the photoelectric effect by Einstein.[4] Since the emitted photoelectron brings important information on the electronic state in solids from which it was excited by photon, the photoemission is used to study the electronic structure and many body effects in solids.[1] Since 1960's, photoemission experiments have remarkably been developed with the use of the synchrotron radiation, which is the most ideal light source for photoemission. Now, the photoemission is one of the most important domain in solid state physics.

Let us consider the photoemission process where photons are incident with the energy $\omega$, the incident direction $\hat{q}$ and the polarization direction $\hat{\eta}$, and electrons are emitted with the energy $\varepsilon$, the emitted direction $\hat{k}$ and the spin $\sigma$. The photoelectron current I is generally represented as a function of $\omega$, $\hat{q}$, $\hat{\eta}$, $\varepsilon$, $\hat{k}$ and $\sigma$:

$$I=F(\varepsilon,\hat{k},\sigma;\omega,\hat{q},\hat{\eta}). \qquad (I.1)$$

In usual photoemission spectra, only a few of the variables $\omega$, $\hat{q}$, $\hat{\eta}$, $\varepsilon$, $\hat{k}$ and $\sigma$ are varied, while others are either kept constant or integrated. Depending on the information desired and the available experimental equipment, the running variable is chosen appropriately. If $\varepsilon$ is resolved and all other parameters are fixed or integrated, we get the energy distribution curve (EDC), from which the information of the electronic density of states in solids is obtained. We often use the binding energy ($E_B$) instead of $\varepsilon$, where $E_B$ is defined by

$$E_B = \omega - \varepsilon. \qquad (I.2)$$

If $\hat{k}$ is resolved, we get the angle resolved photoelectron spectrum, which includes the information of the electronic energy dispersion in solids. If $\sigma$ is resolved, we get the spin polarized photoelectron spectrum, which provides us with the information of the electronic spin polarization in solids. If $E_B$ is kept constant while $\omega$ is swept, we get the constant initial state spectrum (CIS), which gives the information of the final state of the photoexcitation (in view of the one electron picture). If $\varepsilon$ is kept constant while $\omega$ is swept, we get the constant final state spectrum (CFS), which gives the information of the initial state. Various kinds of photoemission spectra mentioned here have played an important role in the study of many body effects in transition metals, rare earth metals and their compounds, as described below.

A well known example where the photoemission played an important role is the study of strong 3d electron correlation in

Ni metal. The photoemission data in Ni was found to be anomalous in the following points: (i) The 3d band width determined by the angle resolved photoemission[5] is much smaller than that of the band calculation.[6] (ii) The exchange splitting of the 3d band determined by the spin polarized photoemission[7] is also much smaller than that of the band calculation.[6] (iii) In the EDC of 3d band, a satellite occurs about 6 eV below the Fermi level.[8] After a long standing controversy, these anomalies are well explained by taking account of the strong electron correlation in the 3d band and by interpreting that the satellite corresponds to the final state where two 3d holes are bound in a single atomic site (so called two-hole bound state).

In 1977, Guillot et al.[9] discovered that the intensity of the " 6 eV satellite " in Ni is resonantly enhanced when the incident photon energy approaches the 3p excitation threshold. This phenomenon is named " resonant photoemission". The resonant photoemission is interpreted as the following second order quantum process[10]: First, a 3p core electron is excited to the 3d band by absorbing the incident photon. Then, the super Coster-Kronig transition occurs, where a 3d electron makes a transition to the 3p level and another 3d electron is excited to become a photoelectron. Therefore, in the final state of the resonant photoemission, two 3d holes are left behind and they form the two-hole bound state, resulting in the resonant enhancement of the 6 eV satellite. In this way, the observation of the resonant photoemission in Ni gave strong support on the 3d electron correlation picture, i.e., the two-hole bound state formation. In order to interpret the experimental CIS of the resonant photo-

emission, it is important to take account of the interference effect (Fano effect)[11] between the direct 3d photoemission and the resonant second order process.[10] A strong spin polarization of the resonant photoemission was also observed experimentally,[12] and well explained theoretically by the above mentioned electron correlation picture.[10] A similar resonant photoemission has also been observed in Cu metal and various transition metal compounds.[13]

Recently, the rare earth systems call much attention because of the strange behavior of 4f electrons such as the mixed valence and heavy electron behavior. The photoemission technique is also found to be very powerful means to study the 4f electron state of these systems. By the analysis of photoemission data, the 4f states of intermetallic compounds $CeRh_3$, $CeRu_2$, $CeCo_2$, etc., as well as an insulating compound $CeO_2$, were found to be in the mixed valence state, whereas they had been considered traditionally in the tetravalent ($Ce^{4+}$) state. For example, the 3d core photoemission spectrum (3d-XPS) of $CeO_2$[14,15,17,18] exhibits three peaks aside from the spin orbit splitting of the 3d level. In the final state of 3d-XPS, a 3d core hole is left behind and couples with 4f electrons through the Coulomb interaction. Therefore the structure of 3d-XPS reflects the electronic states of 4f electrons. By using the impurity Anderson model with a filled valence band,[19,20] the three peak structure of 3d-XPS of $CeO_2$ was analyzed, and the 4f electron number $n_f$ in the ground state was found to be about 0.5, although $CeO_2$ had been considered to be a standard system with tetravalent Ce (i.e., $n_f=0$). In another

form of Ce oxide, $Ce_2O_3$, the 3d-XPS has only two peaks,[16,18] but no detailed analysis has been made.

In rare earth systems, the valence photoemission spectrum (v-XPS), where the 4f electron and valence (or conduction) band electron are photoemitted, is also used to know the 4f state and its hybridization with the valence (or conduction) band. The bremsstrahlung isochromat spectroscopy (BIS), where incident electrons are absorbed and photons are emitted, provides us with the information on the strong correlation of 4f electrons. The resonant photoemission spectrum (R-XPS) has also been observed at the 4d threshold of various rare earth systems.[21] Similarly to the 3d resonance in Ni, the mechanism of the 4d resonance of rare earth systems is considered as follows: A 4d core electron is first excited to the 4f state by absorbing the incident photon, and then the super Coster-Kronig transition occurs, where a 4f electron makes a transition to the 4d level and another 4f electron is emitted. Therefore, only the 4f derived photoemission of v-XPS is enhanced at the 4d threshold, and this phenomenon is used as a technique to separate out the f symmetric state from other symmetric one.[21] Very recently, the v-XPS, BIS and R-XPS have been observed in $CeO_2$ and $Ce_2O_3$,[18] but no satisfactory theoretical analysis has been performed.

Some observations of R-XPS have also been reported for semiconductors, such as black phosphorus,[22] silicon,[23] indium phosphide[24] and germanium diselenide,[25] where the electron correlation of the valence electrons is weak in contrast to the transition metals and rare earth systems. So it is an interesting problem to study how the mechanism of the resonant photoemission

in semiconductors is different from that in transition metals and rare earth systems. In black phosphorus, for example, Taniguchi et al.[22] first observed that when the incident photon energy is swept through the 2p core threshold the CIS of the valence band photoemission at $E_B$=2.7 eV exhibits a weak Fano type resonance and the CIS at $E_B$=10.8 eV shows a strong resonant enhancement. Immediately after this experiment, Kotani and Nakano[26] analyzed the data by using a simplified model and showed that a core exciton state in the intermediate state plays an essentially important role in the second order resonant photoemission process: A 2p electron is excited by the incident photon to form a core exciton, and then it decays through Auger transitions. Since then, however, the effect of the core exciton has been criticized in Si[27,28] and InP.[24] For black phosphorus, high resolution measurements have been made very recently.[29] Some spectral features of the new data in black phosphorus are different from those of the previous measurement. Therefore, it is desirable to reanalyze the R-XPS in black phosphorus with an improved model, and to study more clearly the role of the core exciton.

The purpose of this thesis is to analyze the resonant photoemission in some typical systems with strong and weak electron correlation. We choose Ce and its oxides as the typical system with strong electron correlation and black phosphorus as the typical system with weak electron correlation. In chapter II, 3d-XPS, v-XPS and BIS in Ce oxides are calculated by using the impurity Anderson model with a filled band: In the limit of vanishing hybridization, the ground state of $CeO_2$ consists of the

filled valence band with no 4f electron occupation, whereas that of $Ce_2O_3$ consists of the filled valence band and one extra 4f electron. We improve some previous analyses for $CeO_2$, and give the first analysis for $Ce_2O_3$. In chapter III, the R-XPS in Ce oxides and γ-Ce is calculated. First, we analyze the CIS spectra of $CeO_2$ and $Ce_2O_3$ by using the parameter values determined in chapter II. Then, we analyze the CIS and EDC of γ-Ce. Although γ-Ce is a metal, we can apply our insulator model (of $Ce_2O_3$ type) to this case within the lowest order approximation in the $1/N_f$ expansion,[30] where $N_f$ is the degeneracy of the f state including both the spin and orbital components. In chapter IV, the calculation of the R-XPS in black phosphorus is presented. In this calculation, we neglect the correlation between the valence electrons, but we take into account the effect of a core exciton in the intermediate state. We improve our previous theory[26] by using a more realistic model of the electronic density of states in black phosphorus and by treating explicitly the effect of the core hole potential.[31] We apply this theory to the analysis of the new experimental data for black phosphorus.[29] Finally we summarize our conclusion in chapter V.

## II. XPS and BIS in Cerium Oxides

### § 2.1. Introduction

An insulating compound $CeO_2$ has $CaF_2$ type crystal structure (in Fig. 1 (a)). It was traditionally considered to be standard $Ce^{4+}$ material, but by the recent analysis of photoemission and photoabsorption data it has been found to be in the mixed valence state where $Ce^{4+}$ and $Ce^{3+}$ configurations (i.e. $4f^0$ and $4f^1$ configurations) are strongly mixed. The first analysis of 3d-XPS[14] was made by Fujimori[32] by using a cluster model ($CeO_8$). Then more detailed analyses were performed by Wuilloud et al.[17] and Kotani et al.[19] by using an impurity Anderson model with a filled band. In this model, as shown in Fig. 2, we consider a system consisting of a valence band (O 2p band) and a 4f level $\varepsilon_f$ on a single Ce site. We take account of the hybridization V between the 4f and valence band states, and the Coulomb interaction $U_{ff}$ between 4f electrons. In the limit of vanishing V, the ground state of $CeO_2$ is described by the filled valence band with no 4f electron occupation (Fig. 2 (b)). With a finite value of V the 4f state mixes with the valence band, so that the ground state can be a mixed state between $4f^0$ and $4f^1$ configurations. In the final state of 3d-XPS, the 4f level is pulled down to $\varepsilon_f - U_{fc}$ due to the attractive potential of the 3d core hole $-U_{fc}$.[33] Then, the charge transfer occurs from the valence band to the 4f level, and we have three different configurations $4f^0$, $4f^1$ and $4f^2$, by which the three peak structure of experimental 3d-XPS[14,15,17,18] (Fig. 3 (b)) can be explained. By this analysis, the 4f electron number $n_f$ in the ground state is estimated to be about 0.5.

For $CeO_2$, extensive study of 4f state has also been made by experimental measurements of 2p-photoabsorption (2p-XAS),[15] 3d-photoabsorption (3d-XAS),[34] v-XPS,[17,18,35] and BIS,[17,18,35] and their analysis.[17,20,35] The experimental data of 3d-XPS, 3d-XAS, v-XPS and BIS are shown in Figs. 3 (a)-(c). Main results of these data are analyzed consistently with the analysis of the 3d-XPS by using the impurity Anderson model. But there remain some problems in the analysis of v-XPS and BIS. In the previous calculation of BIS by Wuilloud et al.,[17] a weak structure corresponding to the $4f^2$ final state occurs about 10 eV above the Fermi level $E_F$. This structure could not be observed by their experiment,[35] but, more recently, a weak BIS structure was observed about 15 eV above $E_F$ by Allen[18] as shown in Fig. 3 (a). Also, the energy spacing between the upper edge of v-XPS and the prominent BIS peak calculated by Wuilloud et al.[17] seems to be somewhat smaller than the experimental result[17,18,35] and the position of the 4f state obtained from the band calculation.[36] In all of the v-XPS analysis so far made, only the 4f-derived structure was calculated with disregarding the contribution of the photoexcitation of the valence band (oxygen 2p band). Taking account of these facts, we reanalyze the 3d-XPS, 3d-XAS, v-XPS and BIS of $CeO_2$.

For another insulating compound $Ce_2O_3$ which has $La_2O_3$ type crystal structure (in Fig. 1 (b) and (c)), much less study has been made. Fuggle et al.[16] observed the 3d-XPS, and very recently Allen[18] has measured the v-XPS, BIS and 3d-XPS for a $CeO_2$ film converted progressively to $Ce_2O_3$. According to their data,

the 3d-XPS of $Ce_2O_3$ exhibits two peaks apart from the spin orbit splitting of 3d level (Fig. 3 (b)). The v-XPS has two peaks in $Ce_2O_3$ (Fig. 3 (a)), while only one structure in $CeO_2$, and the BIS has a prominent peak and a weak structure (Fig. 3 (a)). These data have not been analyzed theoretically yet, so we analyze them and discuss the difference in the various spectra between $Ce_2O_3$ and $CeO_2$.

In § 2.2, we present the method of calculations of 3d-XPS, v-XPS and BIS in the impurity Anderson model with the spin and orbital degeneracy $N_f$. We use both a singlet ground state and a spin doublet ground state. In § 2.3, the calculated spectra are compared with the experimental data for $CeO_2$ and $Ce_2O_3$. Section 2.4 is devoted to discussions.

§ 2.2. Formulation

We consider a system consisting of a filled valence band with the energy $\varepsilon_k$, in which k is the index of the energy level (k=1 $\sim$ N), and a 4f level with energy $\varepsilon_f$. The Hamiltonian of this system , H, is written as

$$H = \sum_{\nu}\sum_{k} \varepsilon_k a^{+}_{k\nu}a_{k\nu} + \varepsilon_f \sum_{\nu} a^{+}_{f\nu}a_{f\nu} + U_{ff}\sum_{\nu>\nu'} a^{+}_{f\nu}a_{f\nu}a^{+}_{f\nu'}a_{f\nu'}$$

$$+ \frac{V}{\sqrt{N}} \sum_{k}\sum_{\nu} (a^{+}_{k\nu}a_{f\nu}+a^{+}_{f\nu}a_{k\nu}). \qquad (2.2.1)$$

The operator $a_{i\nu}$ (i=k,f) denotes the annihilation of an electron in the state $(i,\nu)$, where $\nu$ denotes the combined index to specify both 4f orbital symmetry and spin one ( $\nu$= 1 $\sim$ $N_f$). $U_{ff}$ and V represent the intraatomic 4f-4f Coulomb interaction and the hybridization between the valence band state and the 4f state, respectively. In the final state of the 3d-XPS and 3d-XAS, we change $\varepsilon_f$ to $\varepsilon_f - U_{fc}$, where $-U_{fc}$ is the core hole potential.[33]

We denote the ground state with the energy $E_g$ by $|g\rangle$. When a 3d core electron is excited, by absorbing the incident photon, to the high energy photoelectron state, the state $|g\rangle$ changes to the final state of the 3d-XPS, $|f(3d\text{-}XPS)\rangle$ (with the energy $E_f$(3d-XPS)). When a valence electron (an O 2p or a Ce 4f electron) is excited, the state changes to the final state of the v-XPS, $|f(v\text{-}XPS)\rangle$ ($E_f$(v-XPS)). When one 4f electron is added due to the incident electron, the state changes to the final state of the BIS, $|f(BIS)\rangle$ ($E_f$(BIS)). The first one has a core hole and the

same number of valence electrons as those of the ground state, the second one has one less valence electron and the third one has one more valence electron than the ground state.

The 3d-XPS, $I_{3d\text{-}XPS}(E_B)$ is expressed as

$$I_{3d\text{-}XPS}(E_B) = \sum_f |\langle f(3d\text{-}XPS)|g\rangle|^2 L(E_B - E_f(3d\text{-}XPS) + E_g), \qquad (2.2.2)$$

where $E_B = \omega - \varepsilon$ denotes the binding energy with the incident photon energy $\omega$ and the photoelectron kinetic energy $\varepsilon$, and $L(X) = \Gamma/[\pi(X^2+\Gamma^2)]$. $\Gamma$ represents the spectral broadening due to the finite life time of the core hole and the experimental resolution.

The v-XPS, $I_{v\text{-}XPS}(E)$ is expressed as

$$I_{v\text{-}XPS}(E) = \sum_f |\langle f(v\text{-}XPS)|a_{f\nu_0} + \frac{M_s}{\sqrt{N}} \sum_k a_{k\nu_0}|g\rangle|^2 \, L(E + E_f(v\text{-}XPS) - E_g), \qquad (2.2.3)$$

where $M_s$ is the ratio of the matrix elements for the photoexcitations of a valence band electron and a 4f electron. $\nu_0$ denotes a state arbitrarily taken among $N_f$-fold degenerate $\nu$.

The BIS, $I_{BIS}(E)$ is expressed as

$$I_{BIS}(E) = \sum_f |\langle f(BIS)|a^+_{f\nu_0}|g\rangle|^2 \, L(E - E_f(BIS) + E_g). \qquad (2.2.4)$$

If we use the final states having a core hole, eq. (2.2.4) expresses the 3d-XAS.

§ 2.2.1 Basis wave functions for $CeO_2$

In the limit of vanishing V, the ground state of $CeO_2$ is given by $|f^0\rangle$ where the valence band is completely filled and no 4f electron is occupied. (Fig. 2 (b))

$$|f^0\rangle = \prod_{k=1}^{N} \prod_{\nu=1}^{N_f} a^+_{k\nu} |\mathrm{vac}\rangle, \qquad (2.2.5)$$

with $|\mathrm{vac}\rangle$ being the vacuum state. When V is switched on, $|f^0\rangle$ is coupled with the following states:

$$|f^1_{k_1}\rangle = \frac{1}{\sqrt{N_f}} \sum_{\nu} a^+_{f\nu}\, a_{k_1\nu} |f^0\rangle, \qquad (2.2.6)$$

$$|f^2_{k_1k_1}\rangle = \sqrt{\frac{2}{N_f(N_f-1)}} \sum_{\nu_1>\nu_2} a^+_{f\nu_1}\, a_{k_1\nu_1}\, a^+_{f\nu_2}\, a_{k_1\nu_2} |f^0\rangle, \qquad (2.2.7)$$

$$|f^2_{k_1k_2}\rangle = \sqrt{\frac{1}{N_f(N_f-1)}} \sum_{\nu_1\neq\nu_2} a^+_{f\nu_1}\, a_{k_1\nu_1} a^+_{f\nu_2}\, a_{k_2\nu_2} |f^0\rangle \qquad (k_1<k_2), \qquad (2.2.8)$$

$$|f^3_{k_1k_1k_1}\rangle = \sqrt{\frac{6}{N_f(N_f-1)(N_f-2)}} \sum_{\nu_1>\nu_2>\nu_3} \times a^+_{f\nu_1} a_{k_1\nu_1}\, a^+_{f\nu_2}\, a_{k_1\nu_2}\, a^+_{f\nu_3} a_{k_1\nu_3} |f^0\rangle, \qquad (2.2.9)$$

$$|f^3_{k_1k_1k_2}\rangle = \sqrt{\frac{2}{N_f(N_f-1)(N_f-2)}} \sum_{\nu_1>\nu_2,\ \nu_3\neq\nu_1,\nu_2}$$

$$\times a^{+}_{f\nu_1} a_{k_1\nu_1} a^{+}_{f\nu_2} a_{k_1\nu_2} a^{+}_{f\nu_3} a_{k_2\nu_3} |f^0\rangle \quad (k_1 \neq k_2), \qquad (2.2.10)$$

$$|f^3_{k_1k_2k_3}\rangle = \sqrt{\frac{1}{N_f(N_f-1)(N_f-2)}} \sum_{\nu_1\neq\nu_2\neq\nu_3\neq\nu_1}$$

$$\times a^{+}_{f\nu_1} a_{k_1\nu_1} a^{+}_{f\nu_2} a_{k_2\nu_2} a^{+}_{f\nu_3} a_{k_3\nu_3} |f^0\rangle \quad (k_1<k_2<k_3). \qquad (2.2.11)$$

Therefore, we take the states (2.2.5)-(2.2.11) as the basis wave functions for $|g\rangle$ and $|f(3d\text{-XPS})\rangle$, disregarding the states with more than three 4f electrons. The diagonal elements of Hamiltonian H are given by

$$\langle f^0|H|f^0\rangle = N_f \sum_k \varepsilon_k \equiv E_V,$$

$$\langle f^1_{k_1}|H|f^1_{k'_1}\rangle = (E_V - \varepsilon_{k_1} + \varepsilon_f)\delta_{k_1k'_1},$$

$$\langle f^2_{k_1k_1}|H|f^2_{k'_1k'_1}\rangle = (E_V - 2\varepsilon_{k_1} + 2\varepsilon_f + U_{ff})\delta_{k_1k'_1},$$

$$\langle f^2_{k_1k_2}|H|f^2_{k'_1k'_2}\rangle = (E_V-\varepsilon_{k_1} -\varepsilon_{k_2}+2\varepsilon_f+U_{ff})\delta_{k_1k'_1}\delta_{k_2k'_2},$$

$$\langle f^3_{k_1k_1k_1}|H|f^3_{k'_1k'_1k'_1}\rangle = (E_V-3\varepsilon_{k_1}+3\varepsilon_f+3U_{ff})\delta_{k_1k'_1},$$

$$\langle f^3_{k_1k_1k_2}|H|f^3_{k'_1k'_1k'_2}\rangle = (E_V-2\varepsilon_{k_1}-\varepsilon_{k_2}+3\varepsilon_f+3U_{ff})\delta_{k_1k'_1}\delta_{k_2k'_2},$$

$$\langle f^3_{k_1k_2k_3}|H|f^3_{k'_1k'_2k'_3}\rangle = (E_V-\varepsilon_{k_1}-\varepsilon_{k_2}-\varepsilon_{k_3}+3\varepsilon_f+3U_{ff})$$

$$\times \delta_{k_1k'_1}\delta_{k_2k'_2}\delta_{k_3k'_3}.$$

The off-diagonal elements of H are, with use of $v=V/\sqrt{N}$, given by

$$\langle f^0|H|f^1_{k_1}\rangle = \sqrt{N_f}\, v,$$

$$\langle f^1_{k_1}|H|f^2_{k'_1 k'_1}\rangle = \sqrt{2(N_f-1)}\, v\, \delta_{k_1,k'_1}\,,$$

$$\langle f^1_{k_1}|H|f^2_{k'_1 k'_2}\rangle = \sqrt{N_f-1}\, v(\delta_{k_1 k'_1}+\delta_{k_1 k'_2})\,,$$

$$\langle f^2_{k_1 k_1}|H|f^3_{k'_1 k'_1 k'_1}\rangle = \sqrt{3(N_f-2)}\, v\, \delta_{k_1 k'_1}\,,$$

$$\langle f^2_{k_1 k_1}|H|f^3_{k'_1 k'_1 k'_2}\rangle = \sqrt{N_f-2}\, v\, \delta_{k_1 k'_1}\,,$$

$$\langle f^2_{k_1 k_2}|H|f^3_{k'_1 k'_1 k'_2}\rangle = \sqrt{2(N_f-2)}\, v\, \delta_{k_1 k'_1}\delta_{k_2 k'_2}\,,$$

$$\langle f^2_{k_1 k_2}|H|f^3_{k'_1 k'_2 k'_3}\rangle = \sqrt{N_f-2}\, v(\delta_{k_1 k'_1}\delta_{k_2 k'_2} + \delta_{k_1 k'_1}\delta_{k_2 k'_3} + \delta_{k_1 k'_2}\delta_{k_2 k'_3})\,.$$

Since the states $|g\rangle$ and $|f(3d\text{-XPS})\rangle$ thus obtained have the singlet symmetry (not only the spin-singlet but also the orbital-singlet), we denote them by "singlet" state.

In the process of v-XPS, a valence band electron or a 4f electron with $\nu_0$ symmetry is removed, so that we have $N\times N_f-1$ electrons in the final states $|f(\text{v-XPS})\rangle$. The basis states are the following:

$$|f^0_{k_1}\rangle = a_{k_1\nu_0}|f^0\rangle\,, \tag{2.2.12}$$

$$|f^1_{k_1 k_2}\rangle_0 = a_{k_1\nu_0} a^+_{f\nu_0}\, a_{k_2\nu_0}|f^0\rangle \qquad (k_1<k_2)\,, \tag{2.2.13}$$

$$|f^1_{k_1 k_2}\rangle = \frac{1}{\sqrt{N_f-1}}\, a_{k_1\nu_0} \sum_{\nu(\neq\nu_0)} a^+_{f\nu} a_{k_2\nu}|f^0\rangle\,, \tag{2.2.14}$$

$$|f^2_{k_1k_1k_1}> = \sqrt{\frac{2}{(N_f-1)(N_f-2)}}\; a_{k_1\nu_0}\; \nu_1 \overset{\Sigma}{\neq} \nu_2(\neq\nu_0)$$

$$\times\, a^+_{f\nu_1} a_{k_1\nu_1} a^+_{f\nu_2}\, a_{k_1\nu_2}|f^0>, \qquad (2.2.15)$$

$$|f^2_{k_1k_2k_3}>_0 = \frac{1}{\sqrt{N_f-1}}\; a_{k_1\nu_0} a_{f\nu_0} a_{k_2\nu_0}\; \overset{\Sigma}{\nu}(\neq\nu_0)$$

$$\times\, a^+_{f\nu} a_{k_3\nu}|f^0> \quad (k_1<k_2), \qquad (2.2.16)$$

$$|f^2_{k_1k_2k_3}> = \sqrt{\frac{1}{(N_f-1)(N_f-2)}}\; a_{k_1\nu_0}\; \nu_1 \overset{\Sigma}{\neq} \nu_2(\neq\nu_0)$$

$$\times\, a^+_{f\nu_1}\, a_{k_2\nu_1}\, a^+_{f\nu_2} a_{k_3\nu_2}|f^0> \qquad (k_2<k_3). \qquad (2.2.17)$$

Since the states $|f(v\text{-XPS})>$ thus obtained have the spin-doublet symmetry, we denote them by "spin-doublet" state. The diagonal matrix elements of H among these states are given by

$$<f^0_{k_1}|H|f^0_{k'_1}> = (E_V-\varepsilon_{k_1})\delta_{k_1k'_1},$$

$${}_0<f^1_{k_1k_2}|H|f^1_{k'_1k'_2}>_0 = (E_V-\varepsilon_{k_1}-\varepsilon_{k_2}+\varepsilon_f)\delta_{k_1k'_1}\delta_{k_2k'_2},$$

$$<f^1_{k_1k_2}|H|f^1_{k'_1k'_2}> = (E_V-\varepsilon_{k_1}-\varepsilon_{k_2}+\varepsilon_f)\delta_{k_1k'_1}\delta_{k_2k'_2},$$

$$<f^2_{k_1k_1k_1}|H|f^2_{k'_1k'_1k'_1}> = (E_V-3\,\varepsilon_{k_1}+2\,\varepsilon_f+U_{ff})\delta_{k_1k'_1},$$

$$0\langle f^2_{k_1k_2k_3}|H|f^2_{k'_1k'_2k'_3}\rangle 0 = (E_V-\varepsilon_{k_1}-\varepsilon_{k_2}-\varepsilon_{k_3}+2\varepsilon_f+U_{ff})$$

$$\times \delta_{k_1k'_1}\delta_{k_2k'_2}\delta_{k_3k'_3} ,$$

$$\langle f^2_{k_1k_2k_3}|H|f^2_{k_1k_2k_3}\rangle = (E_V-\varepsilon_{k_1}-\varepsilon_{k_2}-\varepsilon_{k_3}+2\varepsilon_f+U_{ff})$$

$$\times \delta_{k_1k'_1}\delta_{k_2k'_2}\delta_{k_3k'_3} .$$

The off-diagonal matrix elements of H among these states are the following:

$$\langle f^0_{k_1}|H|f^1_{k'_1k'_2}\rangle 0 = v\,\delta_{k_1k'_1} - v\,\delta_{k_1k'_2} ,$$

$$\langle f^0_{k_1}|H|f^1_{k'_1k'_2}\rangle = \sqrt{N_f-1}\; v\,\delta_{k_1k'_1} ,$$

$$0\langle f^1_{k_1k_2}|H|f^2_{k'_1k'_2k'_3}\rangle 0 = \sqrt{N_f-1}\; v\,\delta k_1k'_1\,\delta k_2k'_2 ,$$

$$\langle f^1_{k_1k_2}|H|f^2_{k'_1k'_1k'_1}\rangle = \sqrt{2(N_f-2)}\; v\,\delta_{k_1k_2}\delta_{k_1k'_1},$$

$$\langle f^1_{k_1k_2}|H|f^2_{k'_1k'_2k'_3}\rangle 0 = v\,\delta_{k_2k'_3}\,\delta_{k_1k'_1},$$

$$\langle f^1_{k_1k_2}|H|f^2_{k'_1k'_2k'_3} = \sqrt{N_f-2}\; v\,\delta_{k_1k'_1}(\delta_{k_2k'_2}+\delta_{k_2k'_3}).$$

In $|f(BIS)>$, we assume that one 4f electron with $\nu_0$ symmetry is added and we have $NxN_f+1$ electrons. The states are

$$|f^1> = a^+_{f\nu_0}|f^0> , \tag{2.2.18}$$

$$|f^2_{k_1}> = \sqrt{\frac{1}{N_f-1}}\, a^+_{f\nu_0} \sum_{\nu_1(\neq\nu_0)} a^+_{f\nu_1}a_{k_1\nu_1}|f^0>, \tag{2.2.19}$$

$$|f^3_{k_1k_1}> = \sqrt{\frac{2}{(N_f-1)(N_f-2)}}\, a^+_{f\nu_0} \sum_{\nu_1>\nu_2(\neq\nu_0)} \times a^+_{f\nu_1}a_{k_1\nu_1}\, a^+_{f\nu_2}a_{k_1\nu_2}|f^0> , \tag{2.2.20}$$

$$|f^3_{k_1k_2}> = \sqrt{\frac{1}{(N_f-1)(N_f-2)}}\, a^+_{f\nu_0} \sum_{\nu_1\neq\nu_2(\neq\nu_0)} \times a^+_{f\nu_1}a_{k_1\nu_1}\, a^+_{f\nu_2}a_{k_2\nu_2}|f^0> \qquad (k_1<k_2). \tag{2.2.21}$$

Since the states $|f(BIS)>$ thus obtained have the spin-doublet symmetry, we denote them by "spin-doublet" states. The diagonal matrix elements among these states are the following:

$$<f^1|H|f^1> = E_V + \varepsilon_f ,$$

$$<f^2_{k_1}|H|f^2_{k'_1}> = (E_V-\varepsilon_{k_1}+2\varepsilon_f+U_{ff})\delta_{k_1k'_1} ,$$

$$<f^3_{k_1k_1}|H|f^3_{k'_1k'_1}> = (E_V-2\varepsilon_{k_1}+3\varepsilon_f+3U_{ff})\delta_{k_1k'_1},$$

$$\langle f^3_{k_1 k_2} | H | f^3_{k'_1 k'_2} \rangle = (E_V - \varepsilon_{k_1} - \varepsilon_{k_2} + 3\varepsilon_f + 3U_{ff}) \delta_{k_1 k'_1} \delta_{k_2 k'_2} .$$

The off-diagonal matrix elements among these states are

$$\langle f^1 | H | f^2_{k_1} \rangle = \sqrt{N_f - 1}\, v,$$

$$\langle f^2_{k_1} | H | f^3_{k'_1 k'_1} \rangle = \sqrt{2(N_f - 2)}\, v\, \delta_{k_1 k'_1} ,$$

$$\langle f^2_{k_1} | H | f^3_{k'_1, k'_2} \rangle = \sqrt{N_f - 2}\, v\, (\delta_{k_1, k'_1} + \delta_{k_1 k'_2}) .$$

§ 2.2.2 Basis wave functions for $Ce_2O_3$

In the limit of vanishing V, the ground state of $Ce_2O_3$ is given by the $|f^{1'}\rangle$ where the valence band is completely filled and one 4f electron is occupied in the Ce site (Fig. 2 (c)):

$$|f^{1'}\rangle = \sqrt{\frac{1}{N_f}} \sum_{\nu_1} a^+_{f\nu_1} |f^0\rangle . \qquad (2.2.22)$$

In eq.(2.2.22), $|f^0\rangle$ denotes the state where the valence band is filled and the 4f level is empty (See eq. (2.2.5)). When V is switched on, $|f^{1'}\rangle$ is coupled with the following states:

$$|f^{2'}_{k_1}\rangle = \sqrt{\frac{1}{N_f(N_f-1)}} \sum_{\nu_1 \neq \nu_2} a^+_{f\nu_1} a^+_{f\nu_2} a_{k_1 \nu_2} |f^0\rangle , \qquad (2.2.23)$$

$$|f^{3'}_{k_1 k_1}\rangle = \sqrt{\frac{2}{N_f(N_f-1)(N_f-2)}} \sum_{\nu_1 \neq \nu_2 > \nu_3}$$

$$\times a^{+}_{f\nu_1} a^{+}_{f\nu_2} a_{k_1\nu_2} a^{+}_{f\nu_3} a_{k_1\nu_3} |f^0\rangle \ , \qquad (2.2.24)$$

$$|f^{3'}_{k_1k_2}\rangle = \sqrt{\frac{1}{N_f(N_f-1)(N_f-2)}} \sum_{\nu_1\neq\nu_2\neq\nu_3}$$

$$\times a^{+}_{f\nu_1} a^{+}_{f\nu_2} a_{k_1\nu_2} a^{+}_{f\nu_3} a_{k_2\nu_3} |f^0\rangle \quad (k_1<k_2). \qquad (2.2.25)$$

Therefore, we take the states (2.2.22)-(2.2.25) as the basis wave functions for $|g\rangle$ and $|f(3d\text{-XPS})\rangle$, disregarding the states with more than three 4f electrons. The diagonal matrix elements of H are given by

$$\langle f^{1'}|H|f^{1'}\rangle = E_V + \varepsilon_f \ ,$$

$$\langle f^{2'}_{k_1}|H|f^{2'}_{k'_1}\rangle = (E_V-\varepsilon_{k_1}+2\varepsilon_f+U_{ff})\delta_{k_1k'_1} \ ,$$

$$\langle f^{3'}_{k_1k_1}|H|f^{3'}_{k'_1k'_1}\rangle = (E_V-2\varepsilon_{k_1}+3\varepsilon_f+3U_{ff})\delta_{k_1k'_1} \ ,$$

$$\langle f^{3'}_{k_1k_2}|H|f^{3'}_{k'_1k'_2}\rangle = (E_V-\varepsilon_{k_1}-\varepsilon_{k_2}+3\varepsilon_f+3U_{ff})\delta_{k_1k'_1}\delta_{k_2k'_2} \ .$$

The non-zero off-diagonal matrix elements of H are, with use of $v=V/\sqrt{N}$, given by

$$\langle f^{1'}|H|f^{2'}_{k_1}\rangle = \sqrt{N_f-1}\ v,$$

$$\langle f^{2'}_{k_1}|H|f^{3'}_{k'_1,k'_1}\rangle = \sqrt{2(N_f-2)}\,v\delta_{k_1k'_1},$$

$$\langle f^{2'}_{k_1}|H|f^{3'}_{k'_1,k'_2}\rangle = \sqrt{N_f-2}\,v(\delta_{k_1k'_1}+\delta_{k_1k'_2}).$$

Since the states $|g\rangle$ and $|f(3d\text{-XPS})\rangle$ thus obtained have the spin-doublet symmetry, we denote them by "spin-doublet" states.

In the process of v-XPS, a valence band electron or a 4f electron is removed, so that we have $NxN_f$ electrons in the final states $|f(v\text{-XPS})\rangle$. The states $|f(v\text{-XPS})\rangle$ are divided into two classes: One is the "singlet" states (not only the spin-singlet but also the orbital-singlet), which are described by using, as the basis wave functions, the state $|f^0\rangle$ and the states coupled with $|f^0\rangle$ through V. These basis wave functions are the same as those used in describing $|g\rangle$ and $|f(3d\text{-XPS})\rangle$ of $CeO_2$. In the other class, the states $|f(v\text{-XPS})\rangle$ are described by using the following basis wave functions:

$$|f^1_{k_1},0\rangle = \sqrt{\frac{1}{N_f-1}}\,a_{k_1\nu_0}\sum_{\nu(\neq\nu_0)} a^+_{f\nu}|f^0\rangle, \qquad (2.2.26)$$

$$|f^2_{k_1k_2},0\rangle_0 = \sqrt{\frac{1}{N_f-1}}\,a_{k_1\nu_0}\sum_{\nu(\neq\nu_0)} a^+_{f\nu}a^+_{f\nu_0}a_{k_2\nu_0}|f^0\rangle \quad (k_1<k_2), \qquad (2.2.27)$$

$$|f^2_{k_1k_2},0\rangle = \sqrt{\frac{1}{(N_f-1)(N_f-2)}}\,a_{k_1\nu_0}\sum_{\nu\neq\nu'(\neq\nu_0)} a^+_{f\nu}a^+_{f\nu'}a_{k_2\nu'}|f^0\rangle. \qquad (2.2.28)$$

We denote these states by "other symmetry" states, since they have symmetries other than the singlet and spin-doublet symmetries. The diagonal matrix elements of H are given by

$$\langle f^1_{k_1},0|H|f^1_{k'_1},0\rangle = (E_V-\varepsilon_{k_1}+\varepsilon_f)\delta_{k_1k'_1},$$

$$0\langle f^2_{k_1k_2},0|H|f^2_{k'_1k'_2},0\rangle 0 = (E_V-\varepsilon_{k_1}-\varepsilon_{k_2}+2\varepsilon_f+U_{ff})$$

$$\times \delta_{k_1k'_1}\delta_{k_2k'_2},$$

$$\langle f^2_{k_1k_2},0|H|f^2_{k'_1k'_2},0\rangle = (E_V-\varepsilon_{k_1}-\varepsilon_{k_2}+2\varepsilon_f+U_{ff})$$

$$\times \delta_{k_1k'_1}\delta_{k_2k'_2}.$$

The non-zero off-diagonal matrix elements of H among these states are the following:

$$\langle f^1_k,0|H|f^2_{k_1,k_2},0\rangle_0 = v\delta_{k,k_1} - v\delta_{k,k_2},$$

$$\langle f^1_k,0|H|f^2_{k_1,k_2},0\rangle = \sqrt{N_f-2}\; v\delta_{k,k_2}.$$

In $|f(BIS)\rangle$, we assume that one 4f electron with $\nu_0$ symmetry is added and we have $N^xN_f+2$ electrons. The basis wave functions are the following:

$$|f^2\rangle = \sqrt{\frac{1}{N_f}}\; a^+_{f\nu_0} \sum_{\nu_1(\neq\nu_0)} a^+_{f\nu_1}|f^0\rangle, \tag{2.2.29}$$

$$|f^3_{k_1}\rangle = \sqrt{\frac{1}{N_f(N_f-1)}}\; a^+_{f\nu_0} \sum_{\nu_1\neq\nu_2(\neq\nu_0)} a^+_{f\nu_1}a^+_{f\nu_2}a_{k_1\nu_2}|f^0\rangle, \tag{2.2.30}$$

$$|f^4_{k_1k_1}\rangle = \sqrt{\frac{2}{N_f(N_f-1)(N_f-2)}}\; a^+_{f\nu_0} \sum_{\nu_1\neq\nu_2>\nu_3(\neq\nu_0)}$$

$$\times a^+_{f\nu_1}a^+_{f\nu_2}a_{k_1\nu_2}\; a^+_{f\nu_3}a_{k_1\nu_3}|f^0\rangle, \tag{2.2.31}$$

$$|f^4_{k_1k_2}> = \sqrt{\frac{1}{N_f(N_f-1)(N_f-2)}}\, a^+_{f\nu_0} \sum_{\nu_1\neq\nu_2\neq\nu_3(\neq\nu_0)}$$

$$\times\, a^+_{f\nu_1}\, a^+_{f\nu_2} a_{k_1\nu_2} a^+_{f\nu_3} a_{k_2\nu_3} |f^0> \qquad (2.2.32)$$

$$(k_1<k_2).$$

The diagonal elements among these states are following:

$$<f^2|H|f^2> = E_V + 2\varepsilon_f + U_{ff} \ .$$

$$<f^3_{k_1}|H|f^3_{k'_1}> = (E_V - \varepsilon_{k_1} + 3\varepsilon_f + 3U_{ff})\delta_{k_1k'_1},$$

$$<f^4_{k_1k_1}|H|f^4_{k'_1k'_1}> = (E_V - 2\varepsilon_{k_1} + 4\varepsilon_f + 6U_{ff})\delta_{k_1k'_1} \ ,$$

$$<f^4_{k_1k_2}|H|f^4_{k'_1k'_2}> = (E_V - \varepsilon_{k_1} - \varepsilon_{k_2} + 4\varepsilon_f + 6U_{ff})$$

$$\times\, \delta_{k_1k'_1}\delta_{k_2k'_2} \ .$$

The non-zero off-diagonal elements among these states are given by

$$<f^2|H|f^3_{k_1}> = \sqrt{N_f-2}\, v \ ,$$

$$<f^3_{k_1}|H|f^4_{k'_1,k'_1}> = \sqrt{2(N_f-3)}\, v\, \delta_{k_1k'_1},$$

$$<f^3_{k_1}|H|f^4_{k'_1,k'_2}> = \sqrt{N_f-3}\, v\, (\delta_{k_1k'_1} + \delta_{k_1k'_2}).$$

In summary, we take into account the 4f configurations as shown in Table 1 in order to describe the various wave functions.

We neglect the effect of the conduction band. The multiplet structure due to the coupling between 4f electrons, and that between the 4f electron and the core hole, are also disregarded.

## § 2.3. Result of Calculation

We diagonarize numerically the Hamiltonian, eq.(2.2.1), by using the basis wave functions in § 2.2.1 and § 2.2.2, and calculate the spectra, eqs. (2.2.2)-(2.2.4). We adjust the parameter values so as to fit the calculated spectra ($I_{3d\text{-}XPS}(E_B)$, $I_{v\text{-}XPS}(E)$ and $I_{BIS}(E)$) to the experimental data. Numerical calculations are carried out by assuming the valence band spectrum $\varepsilon_k$ as

$$\varepsilon_k = \frac{W}{N}(2k-N-1) \qquad (2.3.1)$$

where W is the valence band width. As an approximation, we take the value N to be finite, but the convergence of the spectrum with N is checked to be sufficiently good.[19] In the present calculations, we use N=6. We also take $N_f$=14 and W=3 eV (for $CeO_2$ and $Ce_2O_3$). As shown in eq. (2.3.1), we take the center of the valence band as the origin of the energy $\varepsilon_k$ (and also $\varepsilon_f$).

### § 2.3.1 $CeO_2$

We first calculate the v-XPS and BIS of $CeO_2$ by using the following set of parameters, which was used by Jo and Kotani[20] in the analysis of 3d-XPS and 3d-XAS of $CeO_2$:

set A: V=0.76 eV, $\varepsilon_f$=1.6 eV, $U_{ff}$=10.5 eV, $U_{fc}$=12.5 eV.

With these values, the ground state is the strongly mixed state between the $4f^0$ and $4f^1$ configurations, and the averaged 4f electron number is $n_f$=0.52. The calculated v-XPS and BIS are shown in Fig. 4 with the solid curve, where we assume $\Gamma = 0.2 + 0.2|E-E_F|$ eV, $M_s$=1.5 and the relative intensity between the v-XPS and BIS is taken arbitrarily. This result is in good agreement

with the following features observed experimentally[18]: The v-XPS has only one broad structure with the width of 3 ∿ 4 eV. The BIS displays a prominent peak and a weak structure about 13 eV above the prominent peak, aside from a broad structure corresponding to the conduction band. From our calculation, it is found that the v-XPS originates mainly from the photoexcitation of the oxygen valence band; the contribution of the valence band excitation is about five times as large as that of the 4f excitation, as is seen from the values of $M_s$=1.5 and $n_f \sim 0.5$. The calculated line shape of v-XPS in $CeO_2$ is almost unchanged (only with the change of the absolute intensity) for any value of $M_s$ satisfying $M_s \geqq 1.5$. It is also found that the prominent BIS peak corresponds to the $4f^1$ final state, while the weak structure 13 ∿ 14 eV above this peak corresponds to the $4f^2$ final state. The occurrence of the latter structure at the right energy position suggests that our parameter values are better than those of Wuilloud et al.[17] However, similarly to the calculation by Wuilloud et al.,[17] our analysis also gives a somewhat smaller energy spacing $E_G$ between the upper edge of v-XPS and the prominent BIS peak (i.e. the energy gap), compared with the experimental value of 3 ∿ 4 eV.

In order to improve the calculated v-XPS and BIS, we try to take another set of parameters:

set B: V=0.9 eV, $\varepsilon_f$=3.5 eV, $U_{ff}$=11.0 eV, $U_{fc}$=13.0 eV

The values of $\Gamma$ and $M_s$ are left unchanged. The result is shown in Fig. 4 with the dashed curve. It is found that the energy spacing $E_G$ becomes larger, in agreement with experimental result.[18] The other spectral features are not very different from those of the

solid curve. With this set B, the ground state is still in the strongly mixed state between $4f^0$ and $4f^1$ configurations. However, the mixing rate is to some extent smaller than that of the set A, and the 4f electron number is $n_f$=0.38.

We next calculate the 3d-XPS and 3d-XAS by using the sets A and B, and compare the results. In Fig. 5 and Fig. 6, respectively, we show the calculated 3d-XPS and 3d-XAS, where we assume $\Gamma$=0.7 eV. The solid and dashed curves are obtained with the use of the sets A and B, respectively. According to the experimental data,[18] the 3d-XPS of $CeO_2$ displays three peaks with energy intervals of about 10 eV and 6 eV. The middle peak has the smallest intensity and the largest width, while the other two peaks are strong and sharp. The experimental 3d-XAS[34] consists of a main peak and a weak satellite, whose energy spacing is about 5eV.

As found from Fig. 5, both of the sets A and B reproduce the experimental features of 3d-XPS[18] rather well. To be more exact, the set A gives a better result; the energy intervals of three peaks are 10.4 eV and 6.8 eV for the set A, whereas 8.3 eV and 8.0 eV for the set B. For the 3d-XAS, as shown in Fig. 6, the result with the set A is to some extent better than the set B both in the relative intensity and the energy spacing between the two peaks (the energy spacing is 5.7 eV for the set A whereas 6.4 eV for the set B).

From our analysis of 3d-XPS, 3d-XAS, v-XPS and BIS, it is difficult to say which of the sets A and B is better. Both of them are fairly good, but they have their own fault. It is also difficult to find a set of parameters with which all of the

experimental data, 3d-XPS, 3d-XAS, v-XPS and BIS, can completely reproduced, probably due to the limitation of our model system. However, it should be possible to compromise the two extremes of sets A and B by taking an intermediate set between them, and improve their faults. For the estimation of the 4f electron number $n_f$, we therefore consider that $n_f(=0.52)$ with the set A gives the upper bound of $n_f$ while $n_f(=0.38)$ with the set B gives its lower bound.

§ 2.3.2 $Ce_2O_3$

We first study how the calculated 3d-XPS depends on the parameters V, $\varepsilon_f$, $U_{ff}$ and $U_{fc}$. In Fig. 7 (a), the 3d-XPS is plotted by changing the value of V. The other parameters are taken to be $\varepsilon_f$=2.0 eV, $U_{ff}$=9.1 eV, $U_{fc}$=12.0 eV and $\Gamma$=1.0 eV, which are appropriate to describe the 3d-XPS of $Ce_2O_3$. The essential role of increasing V is to increase the interval between the two peaks. In Fig. 7 (b) and (c), respectively, we show the spectra calculated for various values of $\varepsilon_f$ and $U_{ff}$. It is found that the change of these parameters causes the change of the intensity ratio between the two peaks. In Fig. 7 (d), we show the change of the spectra by changing $U_{fc}$. The change of $U_{fc}$ gives strong influence on both of the intensity and energy position of the peaks.

We choose our parameter values so as to reproduce the experimental 3d-XPS of $Ce_2O_3$,[18] which exhibits a remarkable two-peak structure with the energy spacing of about 5eV. (The lower binding energy peak is weaker than the higher binding energy one.) Then, we obtain V=0.6 eV, $\varepsilon_f$=2.0 eV, $U_{ff}$=9.1 eV, $U_{fc}$=12.0

eV and $\Gamma$=1.0 eV. With these parameters, the ground state is found to be mainly composed of the $4f^1$ configuration and $n_f$=1.04. The calculated 3d-XPS is displayed in Fig. 8. The two peaks correspond to the final states where the $4f^1$ and $4f^2$ configurations are mixed strongly, and the 4f electron numbers of the higher and lower binding energy peaks are 1.42 and 1.84, respectively.

In Fig. 9, we show the calculated v-XPS and BIS. We use $\Gamma$= 0.2 + 0.2$|E-E_F|$ eV and $M_s$=1.1. On the experimental data,[18] the v-XPS has peaks: The lower energy peak is much broader than the higher energy one, and the energy spacing between them is 3 $\sim$ 4 eV. The experimental BIS[18] has a prominent peak about 8 eV above the higher energy peak of the v-XPS. A weak structure of BIS is also observed about 14 eV above the prominent BIS peak. From our calculation, the lower energy peak of the v-XPS is found to come mainly from the photoexcitation of the valence band (with the final states of "other symmetry") and the valence band contribution is about four times as large as the 4f electron contribution. On the other hand, the higher energy peak of the v-XPS comes mainly from the 4f electron excitation (with the "singlet" final states), and the 4f electron contribution is about ten times as large as the valence band contribution. The valence band-derived XPS with "singlet" final states is much weaker than that with "other symmetry" final states, and the contribution from "other symmetry" final states to the 4f-derived XPS is negligibly small. The prominent BIS peak is found to correspond mainly to the $4f^2$ final state. However, our theory cannot explain the experimental BIS structure about 14 eV above the prominent

peak (designated as B in Fig. 3 (a)). The calculated BIS structure corresponding to the $4f^3$ final state is too weak to reproduce this experimental structure, because the ground state of $Ce_2O_3$ is in the almost pure $4f^1$ configuration. The energy position of the calculated $4f^3$ structure is also different by about 5 eV from that of the experimental structure. Except for this structure, the calculated spectra are in good agreement with the experimental data.[18)]

Before closing this subsection, we remark on our choice of $M_s$. The relative intensity between the two peaks of v-XPS changes remarkably according as we change $M_s$ as shown in Fig. 10. By comparing the calculated v-XPS with the experimental one, we estimate $M_s \sim 1.1$. It can also be shown that with this value of $M_s$ the R-XPS observed by Allen[18)] is well explained, as shown in the next chapter.

§ 2.4. Discussions

We have analyzed the experimental 3d-XPS, v-XPS, and BIS in $Ce_2O_3$ and $CeO_2$ by using the filled band Anderson model. The main conclusions which we have obtained from the analysis are as follows:

(1) In the ground state, $Ce_2O_3$ is in the almost trivalent state, whereas $CeO_2$ is in the mixed valence state with $n_f = 0.4 \sim 0.5$.

(2) In 3d-XPS, $Ce_2O_3$ has two peaks, which are the mixed states between $4f^1$ and $4f^2$ configurations. $CeO_2$ has three peaks; One is mainly composed of $4f^0$ configuration and the other two peaks are the mixed states between $4f^1$ and $4f^2$ configurations.

(3) In v-XPS, $Ce_2O_3$ has two peaks mainly corresponding to the valence band photoemission and 4f electron photoemission. $CeO_2$ has a broad structure, which is mainly composed of the photoemission of the valence band.

(4) In BIS, $Ce_2O_3$ has one peak, which is composed of the $4f^2$ final state. $CeO_2$ has two peaks; One is composed of the $4f^1$ final state, while the other is composed of the $4f^2$ final state.

For the point (1), the essential difference of the ground state between $Ce_2O_3$ and $CeO_2$ is understood as follows: When the oxygen 2p band is filled in the limit of vanishing V, we have one 4f electron occupation ($n_f$=1) for $Ce_2O_3$, while no 4f electron occupation ($n_f$=0) for $CeO_2$. When we switch on the mixing V, as shown in the previous analysis,[19,20] the $4f^0$ and $4f^1$ configurations mix strongly in $CeO_2$ because their energy difference $E(f^1)-E(f^0)=\varepsilon_f-\varepsilon_v$ ($\varepsilon_v$ being the characteristic energy of the valence

band) is comparable with V. In $Ce_2O_3$, on the other hand, the energy difference $E(f^2)-E(f^1)=\varepsilon_f-\varepsilon_v+U_{ff}$ is much larger than V, so that the ground state remains in the almost pure $4f^1$ configuration.

For the point (2), the appearance of the $4f^0$ final state in the 3d-XPS of $CeO_2$ is due to the existence of the $4f^0$ component in the ground state. In $Ce_2O_3$, there is no $4f^0$ component in the ground state, so that the $4f^0$ final state does not occur in the 3d-XPS. From Fig. 5 and Fig. 8, we can see that the lowest binding energy peak of the 3d-XPS in $CeO_2$ is located in between the two peaks of the 3d-XPS in $Ce_2O_3$, in agreement with the experiment.[18)]

For the point (3), $Ce_2O_3$ has one 4f electron in the ground state, so that there is a remarkable 4f electron emission peak. The number of 4f electron in the ground state of $CeO_2$ is small, so the emission of 4f electron is much weaker than the emission of the valence electron. We shall confirm the value of $M_s$, i.e. the ratio between the 4f electron emission and the valence band electron emission by the analysis of the resonant photoemission spectrum.

For the point (4), the ground state of $Ce_2O_3$ has little $4f^2$ component, and thus the $4f^3$ component in the BIS final states is very small and there is no peak. The weak structure about 14 eV above the prominent peak in the experimental BIS may be a structure of the conduction band. The ground state of $CeO_2$ is composed of the $4f^0$ and $4f^1$ configurations, so that the BIS has the $4f^1$ and $4f^2$ peaks.

Finally, it is to be remarked that in order to make more detailed analysis of 3d-XPS, 3d-XAS, v-XPS and BIS in $Ce_2O_3$ and $CeO_2$, the effect of the multiplet structure due to the interaction between 4f electron and the core hole, should be taken into account.

## III. Resonant Photoemission in Cerium Oxides and γ-Cerium

### § 3.1. Introduction

For Ce and its compounds, the behavior of the 4f electron is often strange, such as the mixed valence and heavy electron behavior. To study the 4f electron state in these materials, experimental measurements of various electron spectra mentioned in chapter II[34,35,37-42] and also the R-XPS[21,43-48] have been made. The R-XPS is mainly observed at 4d electron excitation threshold. The 4d core electron is first excited to the 4f state by absorbing the incident photon, and then by the super Coster-Kronig transition a 4f electron makes a transition to the 4d level and another 4f electron is excited as a photoelectron. Therefore, only the 4f-derived v-XPS is enhanced by this mechanism, and we can get from R-XPS the information on the mixing between the 4f state and the valence (or conduction) band.

Most of the R-XPS measurements have so far been made for Ce metal and metallic Ce compounds,[21,48] but very recently R-XPS has also been measured for $CeO_2$ and $Ce_2O_3$.[18] The CIS of R-XPS of $CeO_2$ and $Ce_2O_3$ are shown in Fig. 11. The intensity of the higher energy peak of $Ce_2O_3$ (denoted by $Ce_2O_3$ Ce 4f in Fig. 11) is resonantly enhanced at the 4d threshold (about 120 eV), but the intensity of the lower energy peak of $Ce_2O_3$ (denoted by $Ce_2O_3$ O 2p in Fig. 11 ) is not much enhanced. For $CeO_2$, the resonant enhancement is also observed. The purpose of this chapter is to make the first theoretical analysis for the R-XPS of $CeO_2$ and $Ce_2O_3$, by using the model and parameter values estimated in Chapter II. Another purpose of this chapter is to analyze R-XPS

of γ-Ce, one of the f.c.c. phases of Ce metal. The R-XPS data of γ-Ce[44] (EDC at ω=50, 110, 120, 130 and 170 eV) are shown in Fig. 12, where the EDC has two peaks; one peak is very close to the Fermi level $E_F$, and the other is about 2 eV below $E_F$. The intensities of the two peaks have their maximum values (maximum of the Fano interference[11]) at different values of ω (near 120 eV). The minimum of the CIS (minimum of the Fano interference[11]) occurs about 10 eV below the threshold.

For the quantitative argument, the spectrum at the Fano minimum is usually substracted from the spectrum at the Fano maximum to estimate the relative intensity of the 4f derived emission. After such a procedure for γ-Ce,[45] it is found that the intensity of the 4f emission at $E_F$ is roughly a half of the 4f emission at about 2 eV below $E_F$. For other trivalent Ce compounds, such as $CeAl_2$,[49] this procedure gives almost the same result. For R-XPS of γ-Ce, a theoretical analysis was made by Sakuma et al.,[50] who used the impurity Anderson model by taking account of only the $4f^0$ and $4f^1$ configurations. Their result shows that the resonant enhancement occurs at different photon energies for the two peaks of the EDC; the resonance for the peak near $E_F$ occurs at a smaller photon energy than that of the lower energy peak. This is qualitatively in agreement with experimental data, but is not quantitatively.

In § 3.2, we give a formulation of the R-XPS in the impurity Anderson model with the spin and orbital degeneracy $N_f$. In § 3.3, we calculate the R-XPS for $CeO_2$ and $Ce_2O_3$ by using the same parameter values as we used in chapter II to analyze the 3d-XPS,

v-XPS and BIS. We also calculate the R-XPS for γ-Ce. Section 3.4 is devoted to some discussion.

## § 3.2. Formulation

We consider the material system (4f state and valence band) which is described in the initial, intermediate and final states of the R-XPS by the following Hamiltonian:

$$H_M = \begin{cases} H & \text{(initial and final states)}, \\ H - U_{fc} \sum_{\nu} a^{+}_{f\nu} a_{f\nu} & \text{(intermediate state)}, \end{cases} \tag{3.2.1}$$

where H is given by eq. (2.2.1). By absorbing the incident photon, a core electron can be excited to the 4f state, while the valence electron (4f electron or valence band electron) can be excited to the photoelectron states. These processes are described by the following Hamiltonian:

$$H_R = H_v + H_c, \tag{3.2.2}$$

where

$$H_v = \frac{M_v}{\sqrt{N}} \sum_{k,\nu} a_{k\nu} + M_f \sum_{\nu} a_{f\nu} \ , \tag{3.2.3}$$

$$H_c = M_c \sum_{\nu} a^{+}_{f\nu}. \tag{3.2.4}$$

Here $H_v$ represents the excitation from 4f state or valence band to photoelectron state and $H_c$ represents that from core state to 4f state. We assume that $M_v$, $M_f$ and $M_c$ are real constants. The intermediate state having a core hole is changed to final states by the Auger transition expressed by the following Hamiltonian:

$$H_A = v_A \sum_{\nu \neq \nu'} (a_{f\nu} a_{f\nu'} + \text{h.c.}), \tag{3.2.5}$$

where we assume that $v_A$ is a real constant. We do not write explicitly the creation and annihilation operators of photoelectron and core electron in these Hamiltonians.

We calculate the photoemission spectrum, $I_{R\text{-}XPS}(\omega,\varepsilon)$, for the incident photon energy $\omega$ and the photoelectron kinetic energy $\varepsilon$, in the form

$$I_{R\text{-}XPS}(\omega,\varepsilon)= \sum_f |\langle f|T|g\rangle|^2 \delta(\omega-\varepsilon+E_g-E_f)\,, \tag{3.2.6}$$

$$T= H_R + H_A \frac{1}{Z-H_M-H_A} H_R\,, \tag{3.2.7}$$

$$Z= \omega+ E_g + i\eta \quad (\eta \to 0+), \tag{3.2.8}$$

where $|f\rangle$ represents the final state of v-XPS and $|g\rangle$ represents the initial state. In the T-matrix of eq. (3.2.7), we take into account the terms of the lowest order of $H_R$ and all orders of $H_A$. By using the notation $|m\rangle$ for intermediate states, $\langle f|T|g\rangle$ can be rewritten as

$$\langle f|T|g\rangle= \langle f|H_v|g\rangle + \sum_{m,m'} \langle f|H_A|m\rangle\langle m|\frac{1}{Z-H_M-H_A}|m'\rangle \times \{\langle m'|H_c|g\rangle + \sum_{\varepsilon',f'} \frac{\langle m'|H_A|f'\rangle\langle f'|H_v|g\rangle}{Z-\varepsilon'-E_{f'}}\}. \tag{3.2.9}$$

By using the approximation

$$\langle m|\frac{1}{Z-H_M-H_A}|m'\rangle \sim \frac{\delta_{mm'}}{\omega+E_g-E_m+\varepsilon_c-\Delta_m+i\gamma_m}\,, \tag{3.2.10}$$

where $\varepsilon_c$ represents a core electron energy and

$$\Delta_m - i\gamma_m = \sum_{\varepsilon',f'} \frac{\langle m|H_A|f'\rangle\langle f'|H_A|m\rangle}{Z - \varepsilon' - E_{f'}} \quad , \qquad (3.2.11)$$

we obtain

$$\langle f|T|g\rangle = \langle f|H_v|g\rangle + \sum_m \frac{\langle f|H_A|m\rangle\langle m|H_c|g\rangle}{\omega+E_g-E_m+\varepsilon_c-\Delta_m+i\gamma_m}$$

$$\times \{1 + \sum_{\varepsilon',f'} \frac{\langle m|H_A|f'\rangle\langle f'|H_v|g\rangle}{\langle m|H_c|g\rangle(Z-\varepsilon'-E_{f'})} \} \, . \qquad (3.2.12)$$

Then, the spectrum is expressed as

$$I_{R-XPS}(\omega,\varepsilon) = \sum_f N_f M_f^2 \left| \langle f| a_{f\nu_0} + \frac{M_s}{\sqrt{N}} \sum_k a_{k\nu_0} |g\rangle + \right.$$

$$\sum_{\nu,m} \frac{\langle f|a_{f\nu_0} a_{f\nu}|m\rangle\langle m|a^+_{f\nu}|g\rangle}{\omega+E_g-E_m+\varepsilon_c-\Delta_m+i\gamma_m} \times \{ \frac{M_c v_A}{M_f} +$$

$$\left. \sum_{\varepsilon',f'} \frac{\langle m|H_A|f'\rangle\langle f'|H_A|m\rangle}{Z - \varepsilon' - E_{f'}} \left[ \frac{M_c v_A \langle f'|H_v|g\rangle}{M_f \langle f'|H_A|m\rangle\langle m|H_c|g\rangle} \right] \right|^2$$

$$\times \delta(\omega-\varepsilon+E_g-E_f) \, , \qquad (3.2.13)$$

where

$$M_s = \frac{M_v}{M_f} \, . \qquad (3.2.14)$$

We use the approximation of

$$\frac{M_c v_A \langle f'|H_v|g\rangle}{M_f \langle f'|H_A|m\rangle\langle m|H_c|g\rangle} \sim A_{v\,f',m}\left[\frac{M_c v_A \langle f'|H_v|g\rangle}{M_f \langle f'|H_A|m\rangle\langle m|H_c|g\rangle}\right] \equiv c \ ,$$

(3.2.15)

where $A_v$ represents the average with respect to f and m and c is a real constant, and we assume that $\Delta_m$ and $\gamma_m$ are independent of m. Then, eq. (3.2.13) is rewritten as

$$I_{R\text{-}XPS}(\omega,\varepsilon) = N_f M_f^2 \sum_f \left|\langle f|a_{f\nu_0} + \frac{M_s}{\sqrt{N}} \sum_k a_{k\nu_0}|g\rangle \right.$$
$$\left. + \sum_m \frac{\langle f|a_{f\nu_0}\, a_{f\nu_1}|m\rangle\langle m|a^+_{f\nu_1}|g\rangle}{\omega+E_g-E_m+\tilde{\varepsilon}_c+i\gamma} c\gamma(q-i)\right|^2 \delta(\omega-\varepsilon+E_g-E_f),$$

(3.2.16)

where

$$q = \frac{v_A M_c}{c M_f \gamma} + \frac{\Delta}{\gamma} \qquad (3.2.17)$$

and

$$\tilde{\varepsilon}_c = \varepsilon_c - \Delta \ . \qquad (3.2.18)$$

The basis wave functions for each state ( $|g\rangle$, $|f\rangle$ and $|m\rangle$) are given in § 2.2.1 (for $CeO_2$ type) and § 2.2.2 (for $Ce_2O_3$). For the intermediate states, $|m\rangle$, we use the same basis wave functions as the final states of BIS ( $|f(BIS)\rangle$) (but we use $\varepsilon_f - U_{fc}$ instead of $\varepsilon_f$). In our calculation, we neglect contributions of the conduction band, and the multiplet structure of the intermediate and final states due to the coupling between 4f electrons and that between the 4f electron and the core hole.

## § 3.3. Result of Calculation

We calculate each state of $|g\rangle$, $|m(\text{R-XPS})\rangle$ and $|f(\text{v-XPS})\rangle$ in the same manner as we used in chapter II, and calculate eq. (2.2.1). First, We calculate the CIS of R-XPS of $CeO_2$ and $Ce_2O_3$ by using the same parameter values as we used to analyze the 3d-XPS, 3d-XAS, v-XPS and BIS in chapter II. In this section, $\tilde{\varepsilon}_c$ is not treated explicitly and photon energy, $\omega$, is measured by $E_m - E_g$.

### § 3.3.1 $CeO_2$ and $Ce_2O_3$

For $CeO_2$ and $Ce_2O_3$, there is only one experimental observation of the CIS spectrum by Allen[18] (Fig. 11). For $CeO_2$, we use two sets of parameter values (set A and set B in § 2.3.1), but as shown in Fig. 13 (a) and (b), the CIS for the set A is similar to that for the set B. In these figures, we use $\gamma$= 2 eV, c=1 and q=1 (the solid line) or q=-1 (the dashed line). When we disregard the photoemission of the valence band by taking $M_s$=0.0, the CIS spectrum becomes much different from the experimental one (Fig. 13 (c)). On the other hand, the result with $M_s$ = 1.5 seems to be consistent with the experimental data. It is difficult to make a more detailed data analysis (e.g., the estimation of the value q), partly because the data for $CeO_2$ is not very accurate (as mentioned by Allen[18]) and partly because the experimental back ground is steep. In any case, the tendency of the calculated CIS spectra is similar to the experimental one, and this implies that the 4f state is mixed in the valence band.

Next, we calculate the CIS spectrum for $Ce_2O_3$. From the

experimental data (Fig. 11),[18] the higher energy peak of v-XPS, which is named "$Ce_2O_3$ Ce 4f" in Fig. 11, is very strongly enhanced at the 4d-threshold but the lower energy peak of v-XPS, which is named "$Ce_2O_3$ O 2p", is not very much enhanced. The calculated CIS spectra are shown in Fig. 14 with q=2, c=1 and $\Upsilon$=2 eV. The higher energy peak of v-XPS comes mainly from the 4f electron excitation (See § 2.3.2) so that the resonant enhancement is very large. On the other hand, the lower energy peak of v-XPS comes mainly from the valence band excitation and the resonant enhancement is small. From this result, we confirm that our choice of parameter values, especially $M_s$, in § 2.3.2 is reasonable and that the ground state of $Ce_2O_3$ is in the almost $Ce^{3+}$ state.

§ 3.3.2 $\gamma$-Ce

We analyze experimental data of R-XPS in $\gamma$-Ce. We assume that $\gamma$-Ce is an almost trivalent system (has almost one 4f electron) and we can apply the $Ce_2O_3$ type basis wave functions in the insulating model to $\gamma$-Ce. The effects of the conduction band are neglected by taking into account only leading term of the $1/N_f$ expansion (Fig. 15). For large $N_f$, the states in the first row of Fig. 15 couple with a strength which is independent of $N_f$, while the coupling between the states in the first and second rows or the second and third rows becomes of the order of $1/\sqrt{N_f}$. So, we can disregard the electron hole pair in the conduction band for the limit of $N_f=\infty$ (or even for $N_f$=14).[30] The EDC for $\gamma$-Ce (in Fig. 12)[44] has two peaks, one is near $E_F$ and another is about 2 eV below $E_F$, when the incident photon energy is sufficiently low or high. When the incident photon energy is about 10

eV below the 4d threshold, the EDC has only one broad structure. When the incident photon energy is just at the 4d-threshold, the intensity of the peak with low energy is enhanced resonantly. The intensity of the peak at $E_F$ is enhanced resonantly at slightly smaller incident photon energy.

We determine the parameter values V, $\varepsilon_f$, $U_{ff}$, $U_{fc}$, $\Gamma$, W and $M_s$ by comparing the calculated EDC of R-XPS at the 4d-threshold with the experimental one.[44] The values are V=0.2 eV, $\varepsilon_f$=-0.6 eV, $U_{ff}$=5.5 eV, $U_{fc}$=9.5 eV, $\Gamma$=0.25+0.1|E-$E_F$| eV, W=1.5 eV and $M_s$=0.75. We also estimate the back ground $I_{B.G.}(\omega,E)$, by the following expression.

$$I_{B.G.}(\omega,E) = C \int_E^{\infty} I_{R\text{-}XPS}(\omega,E')dE' \quad , \qquad (3.3.1)$$

where C is a constant and we take C=0.2 to reproduce the experimental data.[44] In Figs. 16 and 17, we show the calculated EDC and CIS (E =-0.4 eV and -2.1 eV, which correspond to the peaks of EDC), respectively, with q=2, c=1 and $\Upsilon$=3 eV. Here, we assume that $\omega$= -12 eV in our previous definition $\omega=E_m-E_g$ corresponds to 120 eV in photon energy of the experimental data, and shown the number, $\omega$+132, in the parenthesis. These spectra are in good agreement with the experimental data. If we use $M_s$=0.0, the spectral shape before the resonance is different from that with finite $M_s$. When $M_s$=0.0, furthermore the EDC disappears, at about 10 eV below the resonance, because the contribution from the 4f electron emission disappears by the interference (i.e., the Fano minimum). Therefore, the finite value of $M_s$ is important to reproduce the experimental data.[44] We also calculate the 3d-

XPS, 3d-XAS, v-XPS and BIS by using the same parameter values as those of R-XPS and show in Fig. 18 (for the 3d-XPS and 3d-XAS with $\Gamma$=0.7 eV) and Fig. 19 (for the v-XPS and BIS with $\Gamma$=0.2+0.2$|E-E_F|$ eV). They are in agreement with the experimental data of $\gamma$-Ce (the experimental data in both $\gamma$-Ce and $\alpha$-Ce are shown in Fig. 20), [37,46] so that our parameter values are confirmed to be reasonable for $\gamma$-Ce. We use the $Ce_2O_3$ type basis wave functions in this analysis, so the initial state has one 4f electron and the final states of BIS have two 4f electrons.

If we use the $CeO_2$ type basis wave functions in the analysis, the resonant behavior and other spectra are different from the above results. We calculate the R-XPS by using the same parameter values as the above calculation but with the $CeO_2$ type model, and the results are shown in Fig. 21 (a: EDC, b: CIS) with $\Gamma$=0.2+0.2$|E-E_F|$ eV. We also calculate the 3d-XPS, 3d-XAS, v-XPS and BIS. They are shown in Fig 22 (for the 3d-XPS and 3d-XAS with $\Gamma$=0.7 eV) and Fig. 23 (for the v-XPS and BIS with $\Gamma$=0.2+0.2$|E-E_F|$ eV). The initial state has about 0.9 electrons in the 4f state. These spectra rather correspond to the mixed valence materials, such as $\alpha$-Ce and $CeRh_3$, and the whole tendency is in agreement with the experimental data.[21,34,38]

§ 3.4. Discussions

We have calculated the R-XPS for $CeO_2$, $Ce_2O_3$ and γ-Ce by using the filled band Anderson model. The main conclusions which we obtained from the analysis are as follows:

(1) We can reproduce the experimental data with use of the same parameter values as we used to analyze the 3d-XPS, v-XPS and BIS.

(2) For $Ce_2O_3$, the intermediate state mainly consists of the $4f^2$ configuration. The low energy structure is not very enhanced at the threshold.

(3) For γ-Ce, we use the $Ce_2O_3$ type basis wave function. The two peaks in the EDC have the different dependence on the incident photon energy. The EDC at about 10 eV below the threshold mainly consists of the conduction electron emission.

(4) With using the $CeO_2$ type basis wave function, we get the spectrum for the mixed valence Ce compounds.

For the point (1), this calculation of the R-XPS is consistent with the calculation of other spectra, and the parameter values are found to be chosen as the best set. The model which we use in this thesis is useful to analyze the various electron spectra consistently for Ce and its compounds.

For the point (2), there is a core hole in the intermediate state, so the 4f level is pulled down by the core hole potential. But, there is at least two 4f electrons, so that the Coulomb repulsion works. Then, the energy difference between the $4f^2$ and $4f^3$ configurations, $E(f^3)-E(f^2) = (\varepsilon_f-U_{fc}) + 2U_{ff} - \varepsilon_v$ ($\varepsilon_v$ being the characteristic energy of the valence band), is comparable with $U_{ff}$ and much larger than V, so the intermediate state re-

mains in the almost pure $4f^2$ configuration. The lower energy structure mainly consists of the valence band electron emission, but the 4f configuration is mixed a little. From the ratio of intensities just at the resonance and well away from the resonance, we can check whether or not the value of $M_s$ is reasonable. We can reproduce the experimental data fairly well, so $M_s$ is found to be chosen as a reasonable value.

For the point (3), the initial state of γ-Ce has one 4f electron, which is consistent with the fact that γ-Ce has the magnetic moment and Kondo temperature is very low. The model is the same as that we used for $Ce_2O_3$, but the behavior of the spectrum is different from that of $Ce_2O_3$. γ-Ce has smaller value of $U_{ff}$ than $Ce_2O_3$ as found from $4f^2$ peak of BIS, so the difference between the $4f^2$ and $4f^3$ configurations, which is about $2U_{ff}-U_{fc}$, is smaller, and these configurations mix each other more strongly than the case of $Ce_2O_3$ in the intermediate state. This is the main reason that two peaks in the EDC of γ-Ce have their Fano maxima at different incident photon energies, in contrast with the case of $Ce_2O_3$. Furthermore, the v-XPS of γ-Ce has a stronger intensity for the lower energy peak, while that of $Ce_2O_3$ has a stronger intensity for the higher energy peak, because $\varepsilon_f$ of γ-Ce is much lower than that of $Ce_2O_3$.

For the point (4), the initial state in the $CeO_2$ type system has a finite weight of the $4f^0$ configuration, and we get a little different spectrum from that in the $Ce_2O_3$ type system. The two peaks in the EDC depend on the incident photon energy in a different way, as found from Figs. 17 and 21 (b). This difference

comes from the difference in the intermediate states, where the $4f^1$ configuration exists in $CeO_2$ type system, as well as from the difference in the final states.

The 4d R-XPS is generally under the influence of the multiplet effects of the intermediate state. The 3d R-XPS has an advantage over the 4d R-XPS in that the 3d R-XPS provides us with the direct information on the different 4f emission without being smeared by the multiplet effect. The 3d R-XPS has very large contrast between the resonant component and the non-resonant component,[47] so we need to take into account only the resonant component. However, there is no experimental 3d R-XPS data of Ce compounds available for comparison with our theory, because the observation has been made only with poor resolution due to some technical difficulty in the relevant photon energy range.[47]

We have used several approximations in the formulation of R-XPS, and it is a remaining problem to examine these approximations in detail. It is also to be remarked that in order to make more detailed analysis of 4d R-XPS in Ce compounds, we should take care of a possible difference between the 3d core hole potential and the 4d core hole potential, and should take into account the multiplet effect, as well as the core electron excitation to the conduction band.

## IV. Resonant Photoemission in Black Phosphorus

### § 4.1. Introduction

Recently, some observations of R-XPS have been reported for semiconductors, such as black phosphorus,[22] silicon[23] and germanium diselenide,[25] where the electron correlation in the valence band is weak. In this chapter we discuss the R-XPS of black phosphorus, which is the most stable form in allotropes of phosphorus at normal condition. Black phosphorus has a layered crystal structure (the crystal structure is shown in Fig. 24)[51] and is a narrow gap semiconductor with energy gap of about 0.3 eV.[52,53] In the last decade, many experiments[22,29,54-63] have been carried out to study characteristic properties of black phosphorus. Some band calculations[64,65] have also been made, and it is shown that the density of states of conduction and valence bands, respectively, increases suddenly a few electron volts above and below the energy gap. It is also found that the density of states of valence band has three main peaks. The band structure and the density of states are shown in Fig. 25.

The first experimental observation of R-XPS in black phosphorus was made by Taniguchi et al.,[22] and the data was analyzed theoretically by Kotani and Nakano[26] with a simplified model system. It was shown that a core exciton plays an important role in the intermediate state. The core exciton is excited by the incident photon at the core excitation edge, and decays by the two different Auger transitions : (i) a direct recombination of the core exciton with the simultaneous excitation of a valence electron and (ii) a recombination of a core hole with a valence

electron with simultaneous excitation of another valence electron. The process (i) interferes with the photoemission of valence electrons, and gives rise to the Fano-type resonance of the valence band photoemission intensity. Furthermore, the core-exciton-induced Auger transition (ii) causes a sharp onset of the Auger electron spectrum, which is much sharper than that of the normal Auger transition following the photoexcitation of a free electron-core hole pair. In the model of Kotani and Nakano, the density of states of the valence and conduction bands is assumed to be constant, and the effect of the core hole potential is not explicitly treated but assumed only to produce a core exciton as an extra state.

For some other semiconductors, however, the effect of the core exciton has been criticized by more recent experimental investigations. For silicon the existence of the core-exciton-induced-resonance seems to be still controversial,[27,28] and for indium phosphide the absence of the core exciton effect has been reported.[24] For black phosphorus, high resolution measurements have been made very recently by Takahashi et al.,[29] and some spectral features different from those of the previous experiment[22] have been reported. Considering these facts, we reanalyze the R-XPS of black phosphorus by using an improved model system.[31]

In §4.2, we present our model Hamiltonian and give a formulation of the resonant photoemission spectra. In § 4.3, the results of numerical calculations of R-XPS are shown. The dependence of spectral features on parameter values included in the

theory is first studied from a somewhat general viewpoint, and then the analysis of experimental data[29] is made. In § 4.4, some discussion is given on the effect of the core exciton.

## § 4.2. Formulation

We consider a system consisting of a conduction band with the energy $\varepsilon_{ck}$, a valence band with $\varepsilon_{vk}$, high energy photoelectron states with $\varepsilon_e$ and a nondegenerate core state with $\varepsilon_p$. For the core state, we consider only one state on the atomic site 0, which is assumed to be excited by the incident photon. The Hamiltonian of this system, H, is written as

$$H = H_0 + U, \tag{4.2.1}$$

$$H_0 = \sum_k \varepsilon_{ck} a^+_{ck} a_{ck} + \sum_k \varepsilon_{vk} a^+_{vk} a_{vk} + \sum_e \varepsilon_e a^+_e a_e + \varepsilon_p a^+_p a_p \,, \tag{4.2.2}$$

$$U = u a^+_0 a_0 a_p a^+_p, \tag{4.2.3}$$

where $a_i$ (i=ck,vk,e,p) denotes the annihilation operator for the electron in each state, U represents a core hole potential, which is assumed, for simplicity, to be of short range and $a_0$ denotes the annihilation operator for a conduction electron on the 0 site (core hole site); $a_0$ and $a_{ck}$ are related by

$$a_0 = \frac{1}{\sqrt{N}} \sum_k a_{ck} \,, \tag{4.2.4}$$

where N is the number of atoms. We assume that the electrons are spinless, and disregard the electron-electron interaction in the valence band and that between a valence electron and a conduction electron.

The ground state of H is written as

$$|g> = \prod_k a^+_{vk} a^+_p |vac>, \qquad (4.2.5)$$

where $|vac>$ denotes the vacuum state. The ground state energy, $E_g$, is described by

$$E_g = \varepsilon_p + \sum_k \varepsilon_{vk}. \qquad (4.2.6)$$

By absorbing the incident photon, the core electron can be excited to the conduction electron states, while the valence electron can be excited to the photoelectron states. These processes are described by the following Hamiltonian:

$$H_R = (M_c a^+_0 a_p + M_k \sum_{e,k} a^+_e a_{vk}) + h.c., \qquad (4.2.7)$$

where the annihilation operator of the incident photon is omitted and "h.c." expresses the Hermitian conjugate that represents the inverse processes. We assume that $M_c$ and $M_k$ are real constants. The existence of the core hole potential U is important in the intermediate state having a core hole, because U modifies the absorption spectrum of the core electron and it has a large influence on the photoemission spectrum. The creation of the core hole is followed by two types of Auger recombinations expressed by the following Hamiltonian:

$$H_A = V_1 + V_2, \qquad (4.2.8)$$

$$V_1 = v_1 \sum_{e,k} (a_e^+ a_p^+ a_{vk} a_0 + \text{h.c.}), \tag{4.2.9}$$

$$V_2 = v_2 \sum_{e,k,k'} (a_e^+ a_p^+ a_{vk} a_{vk'}^+ + \text{h.c.}), \tag{4.2.10}$$

where $V_1$ describes the recombination between a conduction electron and the core hole, and $V_2$ describes that between a valence electron and the core hole. We assumed that $v_1$ and $v_2$ are real constants. After the Auger recombinations, there are two kinds of final states. One is a state having one valence hole and one photoelectron. The other is a state having two valence holes, one conduction electron and one photoelectron. We call the former "one-hole final state" and the latter "two-hole final state".

We calculate the photoemission spectrum, $I(\omega,\varepsilon)$, for the incident photon energy $\omega$ and photoelectron kinetic energy $\varepsilon$, in the form

$$I(\omega,\varepsilon) = 2\pi \sum_f |\langle f|T|g\rangle|^2 \delta(\omega + E_g - E_f)\delta(\varepsilon - \varepsilon_e) , \tag{4.2.11}$$

where T is the t-matrix given by

$$T = V + V \frac{1}{Z-H-V} V, \tag{4.2.12}$$

$$V = H_R + H_A, \tag{4.2.13}$$

$$Z = \omega + E_g + i\eta \quad (\eta = +0), \tag{4.2.14}$$

Here $|f\rangle$ and $E_f$ represent each final state and its energy ($\varepsilon_e$ is included in $E_f$), respectively. By taking account of the lowest

order effects of $H_R$ and all order effects of $H_A$, the spectrum $I(\omega,\varepsilon)$ is written as

$$I(\omega,\varepsilon) = 2\pi \sum_f |\langle f|H_R + H_A \frac{1}{Z - H - H_A} H_R|g\rangle|^2 \delta(\omega + E_g - E_f)\delta(\varepsilon - \varepsilon_e). \quad (4.2.15)$$

We divide $I(\omega,\varepsilon)$ into two terms:

$$I(\omega,\varepsilon) = I_1(\omega,\varepsilon)+I_2(\omega,\varepsilon), \quad (4.2.16)$$

where $I_1(\omega,\varepsilon)$ and $I_2(\omega,\varepsilon)$ correspond to one-hole and two-hole final states, respectively. In the following, we calculated $I_1$ and $I_2$ separately.

§ 4.2.1 One hole final state

We consider the final states $|e,\bar{v}k\rangle$, where we have a photoelectron with energy $\varepsilon_e$ and a free valence hole with $-\varepsilon_{vk}$, and describe the intermediate states in terms of $|ck,\bar{p}\rangle$, where we have one free conduction electron with $\varepsilon_{ck}$ and one core hole with $-\varepsilon_p$. The states $|e,\bar{v}k\rangle$ and $|ck,\bar{p}\rangle$ are eigenstates of H and $H_0$, respectively, and the eigenvalue equations are expressed as

$$H|e,\bar{v}k\rangle = E_{e,\bar{v}k}|e,\bar{v}k\rangle,$$

$$E_{e,\bar{v}k} = E_g - \varepsilon_{vk} + \varepsilon_e, \quad (4.2.17)$$

$$H_0|ck,\bar{p}\rangle = E_{ck,\bar{p}}|ck,\bar{p}\rangle,$$

(4.2.18)

$$E_{ck,\bar{p}} = E_g - \varepsilon_p + \varepsilon_{ck}.$$

Then, the spectrum $I_1(\omega,\varepsilon)$ is written, by using eqs. (4.2.7), (4.2.8), (4.2.9) and (4.2.15) as

$$I_1(\omega,\varepsilon) = 2\pi \sum_{e,k} |\langle e, \bar{vk}| H_R + H_A \frac{1}{Z-H-H_A} H_R |g\rangle|^2 \delta(\omega + E_g - E_{e,\bar{vk}}) \delta(\varepsilon - \varepsilon_e)$$

$$= 2\pi \rho\rho_v(-E_B) |M_k + v_1 \langle 0,\bar{p}| \frac{1}{Z-H-H_A} (M_c |0,\bar{p}\rangle + M_k \sum_{e',k'} |e',\bar{vk}'\rangle)|^2$$

$$= 2\pi\rho\rho_v(-E_B) |M_k + v_1 (M_c + \sum_{e',k'} \frac{M_k \bar{v_1}}{Z - E_{e',\bar{vk}'}}) \langle 0,\bar{p}| \frac{1}{Z-H-H_A} |0,\bar{p}\rangle|^2, \quad (4.2.19)$$

where $\rho_v(-E_B)$ is the density of states of the valence band, $\rho$ is that of the photoelectron states, $E_B = \omega - \varepsilon$ denotes the binding energy, and $|0,\bar{p}\rangle$ denotes the state having a conduction electron on the same site as the core hole. The state $|0,\bar{p}\rangle$ is represented by

$$|0,\bar{p}\rangle = \frac{1}{\sqrt{N}} \sum_k |ck, \bar{p}\rangle . \quad (4.2.20)$$

We calculate $\langle 0,\bar{p}| 1/(Z-H-H_A) |0,\bar{p}\rangle$ by expanding it with respect to $V_1$ and by using the self-energy part

$$\Delta_1 - i\Gamma_1 = \langle 0,\bar{p}| V_1 G_1 V_1 |0,\bar{p}\rangle, \quad (4.2.21)$$

$$G_1 = \frac{1}{Z-H-V_2}, \tag{4.2.22}$$

and then eq. (4.2.19) is rewritten as

$$I_1(\omega,\varepsilon) = 2\pi\rho M_k^2\, \rho_v(-E_B) \left| \frac{1-(\Delta_1-q\Gamma_1)\langle 0,\bar{p}|G_1|0,\bar{p}\rangle}{1-(\Delta_1-i\Gamma_1)\langle 0,\bar{p}|G_1|0,\bar{p}\rangle} \right|^2, \tag{4.2.23}$$

where

$$q = \frac{M_c v_1}{M_k \Gamma_1} + \frac{\Delta_1}{\Gamma_1}. \tag{4.2.24}$$

We assume $\Delta_1$, $\Gamma_1$ and q to be constant. After a little manipulation, $\langle 0,\bar{p}|G_1|0,\bar{p}\rangle$ can be expressed as

$$\langle 0,\bar{p}|G_1|0,\bar{p}\rangle = \frac{\frac{1}{N}\sum_k \frac{1}{\omega+\varepsilon_p-\varepsilon_{ck}-\Delta_2+i\Gamma_2}}{1-\frac{u}{N}\sum_k \frac{1}{\omega+\varepsilon_p-\varepsilon_{ck}-\Delta_2+i\Gamma_2}}, \tag{4.2.25}$$

where $\Delta_2$ and $\Gamma_2$ are real and imaginary parts of the self-energy

$$\Delta_2 - i\Gamma_2 = \langle ck,\bar{p}|V_2 \frac{1}{Z-H} V_2|ck,\bar{p}\rangle, \tag{4.2.26}$$

which occurs when we expand $\langle ck,\bar{p}|G_1|ck,\bar{p}\rangle$ with respect to $V_2$. From eqs. (4.2.23) and (4.2.25), $I_1$ is finally expressed in the following form:

$$I_1(\omega,\varepsilon) = 2\pi\rho M_k^2\ \rho_v(-E_B)\left|\frac{1-\dfrac{u+\Delta_1-q\Gamma_1}{N}\sum_k\dfrac{1}{\omega+\varepsilon_p-\varepsilon_{ck}-\Delta_2+i\Gamma_2}}{1-\dfrac{u+\Delta_1-i\Gamma_1}{N}\sum_k\dfrac{1}{\omega+\varepsilon_p-\varepsilon_{ck}-\Delta_2+i\Gamma_2}}\right|^2 . \qquad (4.2.27)$$

§ 4.2.2 Two-hole final state

We describe the final states as $|e,ck,\bar{v}k',\bar{v}k''\rangle$, where we have a photoelectron with energy $\varepsilon_e$, a free conduction electron with $\varepsilon_{ck}$ and two free valence holes with $-\varepsilon_{vk'}$ and $-\varepsilon_{vk''}$. The eigenvalue equation is written as

$$H|e,ck,\bar{v}k',\bar{v}k''\rangle = E_{e,ck,\bar{v}k',\bar{v}k''}|e,ck,\bar{v}k',\bar{v}k''\rangle , \qquad (4.2.28)$$

$$E_{e,ck,\bar{v}k',\bar{v}k''} = E_g-\varepsilon_{vk'}-\varepsilon_{vk''}+\varepsilon_e+\varepsilon_{ck}.$$

Then the spectrum $I_2$ is expressed, by using eqs. (4.2.7), (4.2.8), (4.2.9), (4.2.10) and (4.2.15), as

$$I_2(\omega,\varepsilon) = 2\pi \sum_{e,k,k',k''}|\langle e,ck,\bar{v}k',\bar{v}k''|H_A\frac{1}{Z-H-H_A}H_R|g\rangle|^2\times$$

$$\delta(\omega+E_g-E_{e,ck,\bar{v}k',\bar{v}k''})\delta(\varepsilon-\varepsilon_e)$$

$$= 2\pi\rho\sum_k|v_2\langle ck,\bar{p}|\frac{1}{Z-H-H_A}(M_c|0,\bar{p}\rangle$$

$$+ M_k\sum_{e',k'''}|e',\bar{v}k'''\rangle)|^2\sum_{k',k''}\delta(E_B+\varepsilon_{vk'}+\varepsilon_{vk''}-\varepsilon_{ck})$$

$$= 2\pi\rho\, M_k^2 \left(\frac{v_2}{v_1}\right)^2 \sum_k \left|\left(\frac{M_c v_1}{M_k} + \Delta_1 - i\Gamma_1\right) \right.$$
$$\left. \langle ck,\bar{p}\left|\frac{1}{Z-H-H_A}\right|0,\bar{p}\rangle\right|^2 S(E_B-\varepsilon_{ck}), \qquad (4.2.29)$$

where $S(X)$ is expressed, by taking the top of the valence band as the origin of energy, as

$$S(X) = \int_{-X}^{0} \rho_v(\varepsilon_v)\rho_v(-X-\varepsilon_v)d\varepsilon_v, \quad (X>0). \qquad (4.2.30)$$

By expanding $\langle ck,\bar{p}\,|1/(Z-H-H_A)\,|0,\bar{p}\rangle$ with respect to $V_1$ and by using the relation $(v_2/v_1)^2 = \kappa/D$ (see Appendix), eq. (4.2.29) is rewritten as

$$I_2(\omega,\varepsilon) = 2\pi\rho M_k^2 \frac{\kappa(q^2+1)}{D}\left(\frac{\Gamma}{1+\kappa}\right)^2 \frac{\sum_k |\langle ck,\bar{p}|G_1|0,\bar{p}\rangle|^2 S(E_B-\varepsilon_{ck})}{|1-(\Delta_1-i\Gamma_1)\langle 0,\bar{p}|G_1|0,\bar{p}\rangle|^2}, \qquad (4.2.31)$$

where

$$D = \int \rho_v(\varepsilon_v)d\varepsilon_v, \qquad (4.2.32)$$

$$\kappa = \frac{\Gamma_2}{\Gamma_1}, \qquad (4.2.33)$$

and

$$\Gamma = \Gamma_1 + \Gamma_2. \qquad (4.2.34)$$

We assume $\Delta_2$, $\Gamma_2$ and $\kappa$ to be constant. After a little manipula-

tion, $\langle ck,\bar{p}|G_1|0,\bar{p}\rangle$ is expressed as

$$\langle ck,\bar{p}|G_1|0,\bar{p}\rangle = \frac{1}{\sqrt{N}} \frac{\dfrac{1}{\omega+\varepsilon_p-\varepsilon_{ck}-\Delta_2-i\Gamma_2}}{1-\dfrac{u}{N}\sum_{k'}\dfrac{1}{\omega+\varepsilon_p-\varepsilon_{ck'}-\Delta_2-i\Gamma_2}} \cdot \qquad (4.2.35)$$

From eqs. (4.2.31) and (4.2.35), $I_2$ is expressed in the following form:

$$I_2(\omega,\varepsilon) = 2\pi\rho M_k^2 \frac{\kappa(q^2+1)}{D}\left(\frac{\Gamma}{1+\kappa}\right)^2 \frac{\dfrac{1}{N}\sum_k \dfrac{S(E_B-\varepsilon_{ck})}{(\omega+\varepsilon_p-\varepsilon_{ck}-\Delta_2)^2+\Gamma_2^2}}{\left|1-\dfrac{u+\Delta_1-i\Gamma_1}{N}\sum_{k'}\dfrac{1}{\omega+\varepsilon_p-\varepsilon_{ck'}-\Delta_2+i\Gamma_2}\right|^2} . \qquad (4.2.36)$$

## § 4.3. Result of Calculation

In this section, we calculate the spectra $I_1(\omega,\varepsilon)$, $I_2(\omega,\varepsilon)$ and $I(\omega,\varepsilon)$ by using a model density of states of black phosphorus as shown in Fig. 26. This density of states is constructed by taking account of the experimental photoemission spectra[22,29,58] (for the valence band) and the energy band calculation[65] (for the conduction band). The quantities q, $\kappa$, u and $\Gamma$ are treated as parameters, whereas $\Delta_1$ and $\Delta_2$ are not treated explicitly but regarded as already included in u and $\varepsilon_p$, respectively [see eqs. (4.2.27) and (4.2.36)]. In order to take account of the effect of the spin-orbit splitting of the 2p core states, we superpose the spectra with two different $\varepsilon_p$, which correspond to the core exciton excitation energies 130.6 eV and 131.4 eV,[29,62] with the weights 2/3 and 1/3, respectively. With our model, the core exciton is not a true bound state but a resonance state, except for too large value of $|u|$. As an example, the density of states of the conduction band for u=-1.25 eV is shown in Fig. 27 with the solid line, compared with that for u=0 (dotted line). A sharp peak is found slightly above the bottom of the conduction band and this represents the core exciton.

In § 4.3.1, we investigate how the calculated spectra depend on the parameter values of q, $\kappa$, u and $\Gamma$. There, we confine our calculations to constant initial state spectra (CIS spectra) of $I_1$ at $E_B$=2.5 eV and $I_2$ at $E_B$=10.4 eV, where the binding energy $E_B$ is measured from the top of the valence band. These calculations are very important in comparing the results with experimental data, since the main experimental results have been reported for

these CIS spectra.[29] In § 4.3.2, we adjust the parameter values so as to fit the calculated spectra to the experimental data.

§ 4.3.1 Parameter dependence of CIS spectra

We show in Fig. 28 the CIS spectra calculated for $E_B$=2.5 eV, which corresponds to the binding energy of the first peak of the valence band photoemission spectrum (see Fig. 32). The structure of these CIS spectra in the vicinity of $\omega\sim$130 eV originates from the interference effect (so-called Fano-type resonance)[11] between the direct photoemission process due to $M_k$ and the second order process (mainly through the core exciton intermediate state) due to $M_c$ and $V_1$. In Fig. 28 (a) and (b), we show the change of the spectra by changing q and $\kappa$. The essential roles of q and $\kappa$ are understood by noting that the present calculation is a finite u version of the simple Fano formula, which we have used in previous theory.[26] In the limit of $|u|\to\infty$, eq. (4.2.27) reduces to the form

$$I_1 = 2\pi\rho M_k^2 \rho_v(-E_B) \frac{(\tilde{\omega}+\frac{q}{1+\kappa})^2+(\frac{\kappa}{1+\kappa})^2}{\tilde{\omega}^2+1}, \qquad (4.3.1)$$

where $\tilde{\omega}$ is defined by $(\omega-\varepsilon_{ex})/\Gamma$ with the core exciton excitation energy $\varepsilon_{ex}$. Therefore, q determines the pattern of the structure due to the interference effect, while $\kappa$ determines the relative intensity between the spectrum with the interference (due to the recombination $V_1$) and that without the interference (due to $V_2$). Even when u is finite, these effects of q and $\kappa$ are essentially unchanged, as found from Fig. 28 (a) and (b). For q=0, we have

two antiresonance dips at the photon energies corresponding to the spin-orbit split core excitons, and with increasing q the asymmetric peaks also occur. When the sign of q is inverted, the peaks (dips) are found to change to dips (peaks), except for the case $q \sim 0$. On the other hand, it is also found that when $\kappa$ is increased [from Fig. 28 (a) to (b)] the amplitude of the interference structure decreases, corresponding to the decrease of the relative weight of the recombination $V_1$.

The effects of the change of u and $\Gamma$ are shown in Fig. 28 (c) and (d), respectively. When u is decreased, the interference structure is broadened and its intensity becomes small, because the oscillator strength of the core exciton decreases. The broadening of the structure also occurs with the increase of the life time width $\Gamma$ of the intermediate states, as found from Fig. 28 (d). These effects of u and $\Gamma$ are essentially the same when q and $\kappa$ are changed.

In Fig. 29, we show the CIS spectra of $I_2$ at $E_B$=10.4 eV, which corresponds to the binding energy of the $L_{2,3}VV$ Auger peak just at the 2p excitation threshold. Also, this binding energy coincides almost with the fourth peak of the valence band photoemission spectrum (see Fig. 32). We show in Fig. 29 (a) the spectra for various values of q and $\kappa$. It is found that the intensity of $I_2$ changes remarkably (note the different scale of the ordinate for each figure) with the change of q and $\kappa$, but the spectral shape (i.e., the $\omega$ dependence of $I_2$) is not very dependent on q and $\kappa$. This is understood from eq. (4.2.36), where $I_2$ depends on q and $\kappa$ mainly through the $\omega$ independent factor

$\kappa(q^2+1)/(1+\kappa)^2$.

The two-peak structure in Fig. 29 (a) comes from the core-exciton-induced $L_{2,3}VV$ Auger transition. This is clearly seen from Fig. 29 (b), where we show the change of the spectra by changing u with other parameters fixed appropriately. When u is strong, the core exciton is excited with a large oscillator strength and induces the strong $L_{2,3}VV$ Auger transition, resulting in the conspicuous two-peak structure as shown in the case of u=-2.0 eV in Fig. 29 (b). These Auger peaks have high energy tails, which come from the Auger transition following the photoexcitation of the unbound pair of a conduction electron and a core hole. When $|u|$ is decreased, the intensity of the tail increases, since the oscillator strength of the unbound pair excitation increases, whereas the intensity of the core exciton decreases. Then, the relative intensity between the two peaks in Fig. 29 (b) is inverted with decreasing $|u|$, because the higher energy peak is superposed on the tail of the lower energy peak. When u is very weak or u vanishes, the two-peak structure cannot be found, but we have only a broad peak which originates from the normal $L_{2,3}VV$ Auger transition following the photoexcitation of a free conduction electron-core hole pair.

The effect of the change of $\Gamma$ is shown in Fig. 29 (c). With increasing $\Gamma$, the two-peak structure is broadened. Furthermore, the intensity of $I_2$ increases with $\Gamma$, as also seen from eq. (4.2.36).

§ 4.3.2. Comparison with the experimental spectra

Keeping in mind the effects of q, $\kappa$, u and $\Gamma$ studied in §

4.3.1, we choose these parameter values so as to fit the calculated CIS spectra to the experimental ones observed by Takahashi et al.[29] In order to take account of the experimental resolution, we convolute the calculated spectrum $I(\omega,E_B)$ [here, the argument $\varepsilon$ is changed to $E_B$] with the Gaussian function of appropriate width ($\Delta\omega=\Delta E_B=0.15$ eV) with respect to $\omega$ (or $E_B$). Furthermore, we take account of the secondary electron intensity, which is estimated by

$$I_S(\omega,E_B) = C\int_0^{E_B} I(\omega,E_B')\,dE_B' \qquad (4.3.2)$$

with a constant C. We choose C=0.045 so as to reproduce the experimental energy distribution curve for $\omega$ smaller than the core exciton edge. In Fig. 30, we show the CIS spectra calculated for $E_B$=2.5 eV and 10.4 eV by using the parameter values of q=-150, $\kappa$=900, u=-1.25 eV and $\Gamma$=0.2 eV. This result is in good agreement with the experimental data,[29] which is plotted in the inset of Fig. 30.

Of our parameter values, $\Gamma$ is estimated from the experimental data of reflection spectrum.[62] The value of u=-1.25 eV is chosen so as to reproduce the relative intensity of two peaks in the CIS spectrum at $E_B$=10.4 eV [see Fig. 29 (b)]. From the experimental intensity ratio between the CIS spectra at $E_B$=2.5 eV and 10.4 eV for $\omega\sim$131 eV, we find that the factor $\kappa(q^2+1)/(\kappa+1)^2$ is to be taken as about 25. Under this condition, each value of q and $\kappa$ is determined in order to give the CIS spectrum at 2.5 eV consistent with the experiment. It is to be noted that the value of $\kappa$ should be very large because the experimental amplitude of

the interference structure is very small. Furthermore, the sign of q should be negative, because the experimental CIS spectrum at $E_B$=2.5 eV exhibits a peak when ω approaches the core exciton threshold from lower energy side (otherwise, we have a dip).

In Fig. 32 we show the energy distribution curves calculated for various values of the incident photon energy. For ω=120.2 eV, which is considerably smaller than the core exciton threshold, the spectrum simply reflects the density of states of the valence band. However, for ω =130∿131, the intensity of the peak at $E_B$=10.4 eV increases resonantly, representing the core-exciton-induced $L_{2,3}VV$ Auger transition. When ω becomes larger than the core exciton threshold, the peak shifts to the higher binding energy side, representing the occurrence of the normal $L_{2,3}VV$ Auger transition. These features are in good agreement with the experimental result (shown in Fig. 31).[29)]

§ 4.4. Discussions

We have improved our previous theory[26] of the resonant photoemission in black phosphorus, and applied it to the analysis of the recent experimental data. The main conclusions which we have obtained from the analysis are as follows :

(1) The weak structure in the CIS spectrum for $E_B$=2.5 eV is due to the interference between the direct valence band photoemission and the second order process with the core exciton state as an intermediate state.

(2) The rapid increase of the CIS spectrum for $E_B$=10.4 eV at the 2p threshold, as well as its two-peak structure, are due to the core-exciton-induced $L_{2,3}VV$ Auger transition.

In connection with the former point (1), Takahashi et al. suggested another origin of the CIS structure that it comes from the low binding energy tail of the spectrum $I_2$. Near the 2p threshold, the intensity of $I_2$ is strongly enhanced, and then that of the low binding energy tail is also modified. Therefore, if the tail of $I_2$ has the sufficient intensity at $E_B$=2.5 eV, this mechanism may explain the observed CIS structure. In order to examine this possibility, we calculate, with our model system the intensity of $I_2$ at $E_B$=2.5 eV as shown in Fig. 33. The intensity thus obtained is plotted in the inset of Fig. 33 as a function of $\omega$. From this calculation, it is found that this contribution is too weak (an order of magnitude weaker) to explain the experimental CIS structure. Furthermore, by this mechanism the energies of the two peaks of the CIS spectrum for $E_B$=2.5 eV coincide with those of the CIS spectrum for $E_B$=10.4 eV. However,

the experimental peak energies for $E_B$=2.5 eV are slightly (but definitely) shifted to the low energy side compared with those for $E_B$=10.4 eV. By the mechanism (1) of the interference effect, the peak energy is a little bit smaller than the core exciton excitation energy, when q is negative, as in the case of the usual Fano resonance (see also Fig. 28).

For the latter point (2), it is to be stressed that in order to reproduce the experimental two-peak structure we have to take account of the $L_{2,3}VV$ Auger transitions which are induced not only by the core exciton state but also by the unbound conduction electron-core hole pair. The experimental result can neither be reproduced with too large $|u|$ (where we have the contribution only from the core exciton) nor with too small $|u|$ (the contribution only from the unbound pair), as shown in Fig. 29 (b).

More recently, high resolution measurements have been made by Taniguchi et al.[66] Their data are mainly in agreement with the present analysis, but some features are different. It seems that the CIS spectrum for $E_B$=10.4 eV in the new data has two components at each spin orbit split component. This fact is clearly found in the total yield,[62] which is shown in Fig. 34 (a), and it seems that two kinds of core exciton give rise to this structure. Therefore, we take into account one more component whose excitation energy is about 0.2 eV less than the already considered component, and the calculated photoabsorption spectrum (total yield) is shown in Fig. 34 (b). This result is very similar to the experimental data and it can be shown that the calculated CIS is also similar to the experimental one.[66] So

we can analyze the experimental data fairly well by using our model.

For more detailed theoretical analysis, the present model should also be improved by taking account of the effects of the core hole potential with a finite potential range, more detailed energy band structures and the energy (or momentum) dependence of $M_k$, $M_c$, $v_1$ and $v_2$. However, the essential features of (1) and (2) will not be changed even with the improved model, since they are not very sensitive to the quantitative details of the model system.

It is to be mentioned that the present theory can also be applied to the analysis of the previous experimental data by Taniguchi et al.[22] We obtain the result in agreement with the experiment by using the parameter values $q \sim 70$, $\kappa \sim 200$ and $u \sim -2.5$ eV which are different from those used in the analysis in § 4.3.2 (and also different from those of our previous analysis because of the difference in the model system). It is beyond the scope of the present thesis to discuss which set of the parameter values is more reasonable for black phosphorus from a theoretical viewpoint, and also to discuss the reason of the discrepancy of the two experimental data. Finally, we mention that it is an important unsolved problem to estimate q and $\kappa$ from the first principle calculation.

## IV. Conclusions

In this thesis, we have shown that our theory can reproduce well various experimental spectra for Ce oxides, γ-Ce and black phosphorus. The main conclusions which we have obtained from the analyses are as follows:

(1) 3d-XPS, v-XPS and BIS of Ce oxides

In the ground state, $Ce_2O_3$ is in the almost trivalent state, whereas $CeO_2$ is in the mixed valence state, because the energy difference between $4f^1$ and $4f^2$ configurations in $Ce_2O_3$ is much larger than V, whereas the energy difference between $4f^0$ and $4f^1$ configurations in $CeO_2$ is comparable with V. In the final state of 3d-XPS, the energy difference between $4f^1$ and $4f^2$ configurations in both materials is comparable with V. So the 3d-XPS has three peaks in $CeO_2$, while two peaks in $Ce_2O_3$. In the v-XPS, $Ce_2O_3$ has two peaks mainly corresponding to the valence band photoemission and 4f electron photoemission. $CeO_2$ has one broad structure mainly corresponding to the valence band photoemission. In BIS, $Ce_2O_3$ has one peak, which is composed of mainly the $4f^2$ final state. $CeO_2$ has two peaks; One is composed of the $4f^1$ final state, and the other is composed of the $4f^2$ final state.

(2) R-XPS of Ce oxides and γ-Ce

We can fit the calculated R-XPS to the experimental one with use of the same parameter values as those we determined from the analysis of the 3d-XPS, 3d-XAS, v-XPS and BIS. Both of γ-Ce and $Ce_2O_3$ are in the almost trivalent state, but they show the different CIS behavior of R-XPS. This can be explained mainly from that the intermediate states of γ-Ce are different from those of $Ce_2O_3$, because of the different parameter values.

(3) R-XPS of black phosphorus

The weak structure in the CIS spectrum for $E_B$=2.5 eV is due to the interference between the direct valence band photoemission and the second order process with the core exciton state as an intermediate state, and the rapid increase of the CIS spectrum for $E_B$=10.4 eV at 2p threshold is due to the core-exciton-induced $L_{2,3}VV$ Auger transition. So, the core exciton state plays the important role as the intermediate state in the R-XPS. Our model can also be applied to the analysis of R-XPS in the other semiconductors which have the wide valence band and weak electron correlation.

Finally we remark some remaining problems. In our model of Ce oxides, we neglect effects of the multiplet structure and the conduction band. In more detailed analysis of BIS and R-XPS, it will be necessary to take account of these effects. When we apply this model to the analysis of the metallic materials, it is desirable to show quantitatively the convergence of the $1/N_f$ expansion. Furthermore, there should be a limitation in the impurity Anderson model, and it is also a remaining problem to show clearly the limitation. For the black phosphorus model, we neglect the correlation between the valence band electrons and that between the valence band electron and the conduction band electron. We also assume a short range potential as the core hole potential. When we apply this model to the analysis of copper halides, above mentioned electron correlations are important.[67] The effect of finite range of the core hole potential will also be important in more detailed analysis.

Acknowledgements

The author would like to express his sincere thanks to Professor Akio Kotani for valuable discussions and continuous encouragement from suggestion of the problem to preparation of the manuscript. He also would like to express his thanks to Professor Junjiro Kanamori, Professor J. C. Parlebas, Dr. Takeo Jo, Dr. Jun-ichi Igarashi and Mr. Masato Okada for their valuable discussions and continuous encouragement, and to Professor S.-J. Oh, Professor A. Bianconi, Dr. Masaki Taniguchi and Dr. Takashi Takahashi for providing him with important information on the experimental data. He would like to express his special gratitude to Dr. Kozo Okada for his critical discussion and encouragement. Finally he also would like to acknowledge the help of Ms. Akimi Egusa in preparing the manuscript.

## Appendix

From their definitions, $\Gamma_1$ and $\Gamma_2$ are expressed as

$$\Gamma_1 = -\mathrm{Im} \langle 0,\bar{p}|V_1 \frac{1}{Z - H - V_2} V_1|0,\bar{p}\rangle$$

$$= \pi v_1^2 \sum_{e,k} \delta(\omega-\varepsilon_e+\varepsilon_{vk}), \qquad (A.1)$$

$$\Gamma_2 = -\mathrm{Im} \langle ck,\bar{p}|V_2 \frac{1}{Z - H} V_2|ck,\bar{p}\rangle$$

$$= \pi v_2^2 \sum_{e,k',k''} \delta(\omega-\varepsilon_e+\varepsilon_{vk'}+\varepsilon_{vk''}-\varepsilon_{ck}). \qquad (A.2)$$

Then, we obtain

$$\kappa = \frac{\Gamma_2}{\Gamma_1} = \left(\frac{v_2}{v_1}\right)^2 \frac{\sum_{e,k',k''} \delta(\omega-\varepsilon_e+\varepsilon_{vk'}+\varepsilon_{vk''}-\varepsilon_{ck})}{\sum_{e,k} \delta(\omega-\varepsilon_e+\varepsilon_{vk})}$$

$$= \left(\frac{v_2}{v_1}\right)^2 \frac{\int d\varepsilon_v \rho_v(\varepsilon_v) \int_{\varepsilon_{ck}-\omega-\varepsilon_v}^{0} d\varepsilon_v' \rho_c(\varepsilon_v')}{\int_{-\omega}^{0} d\varepsilon_v \, \rho_v(\varepsilon_v)} . \qquad (A.3)$$

Since $\omega$ is much larger than the effective range of $\varepsilon_{ck}$ and $\varepsilon_{vk}$ ($\omega \sim 10^2$ eV and the range of $\varepsilon_{ck}$ and $\varepsilon_{vk} \sim 10$ eV), eq. (A.3) can be approximately rewritten as

$$\kappa \sim \left(\frac{v_2}{v_1}\right)^2 \frac{D^2}{D} = \left(\frac{v_2}{v_1}\right)^2 D, \qquad (A.4)$$

where

$$D = \int \rho_v(\varepsilon_v) d\varepsilon_v. \qquad (A.5)$$

References


1) Photoemission in Solids I and II, Topic Applied Physics Vols. 26 and 27 (Springer-Verlag 1978, 1979) ed. M. Cardona and L. Ley.

2) H. Hertz: Ann. Physik 31 (1887) 983.

3) J. J. Thomson: Phil. Mag. 44 (1897) 293.

4) A. Einstein: Ann. Physik 17 (1905) 132.

5) F. J. Himpsel, J. A. Knapp and D. E. Eastman: Phys. Rev. B19 (1979) 2919.

6) V. L. Moruzzi, J. F. Janak and A. R. Williams: Calculated Electronic Property of Metals (Pergamon 1978).

7) U. Bänninger, G. Busch, M. Campagna and H. C. Siegmann: Phys. Rev. Lett. 25 (1970) 383.

8) Y. Baer, P. F. Hedin, J. Hedman, M. Klasson, C. Nordling K. Siegbahn: Phys. Scr. 1 (1970) 55.

9) C. Guillot, Y. Ballu, J. Paigné, J. Lecante, K. P. Jain P. Thiry, R. Pinchaux, Y. Pétroff and L.M. Falicov: Phys. Rev. Lett. 39 (1977) 1632.

10) T. Jo, A. Kotani, J. C. Parlebas and J. Kanamori: J. Phys. Soc. Jpn. 52 (1983) 2581.

11) U. Fano: Phys. Rev. 124 (1961) 1866.

12) R. Clauberg, W. Gudat, E. Kisker, E. Kuhlmann and G. M. Rothberg: Phys. Rev. Lett. 47 (1981) 1314.

13) See, for instance, D. Chandesris, J. Lecante and Y. Pétroff: Phys. Rev. B27 (1983) 2630.

14) P. Burroughs, A. Hamnett, A. F. Orchard and G. Thornton:

J. Chem. Soc., Dalton Trans. 17 (1976) 1686.

15) E. Beaurepaire: Thesis Institut, Polytechnique, Nancy (1983).

16) J. C. Fuggle, M. Campagna, Z. Zolnierek, R. Lässer and and A. Platau: Phys. Rev. Lett. 45 (1980) 1597.

17) E. Wuiloud, B. Delly, W. -D. Schneider and Y. Baer: Phys. Rev. Lett 53 (1984) 202.

18) J. W. Allen: J. Magn. and Magn. Mater. 47&48 (1985) 168.

19) A. Kotani, H. Mizuta, T. Jo and J. C. Parlebas: Solid State Commun. 53 (1985) 805.

20) T. Jo and A. Kotani: J. Phys. Soc. Jpn. 55 (1986) 2457.

21) See, for instance, D.J. Peterman, J.H. Weaver, M. Croft and D.T. Peterson: Phys. Rev. B27 (1983) 808.

22) M. Taniguchi, S. Suga, M. Seki, H. Sakamoto, H. Kanzaki, Y. Akahama, S. Endo, S. Terada and S. Narita: Solid State Commun. 49 (1984) 867.

23) K.L.I. Kobayashi, H. Daimon and Y. Murata: Phys. Rev. Lett. 51 (1983) 1701.

24) T. Kendelewicz, R.S. List, M.D. Williams, I. Lindau and W. E. Spicer: Phys. Rev. B30 (1984) 2263.

25) K. Inoue, M. Kobayashi, K. Murase, M. Taniguchi and S. Suga: Solid State Commun. 54 (1985) 193.

26) A. Kotani and T. Nakano: Solid State Commun. 51 (1984) 97.

27) R.A. Riedel, M. Turowski, G. Margaritondo and P. Perfetti: Phys. Rev. Lett. 52 (1984) 1568.

28) R.A. Riedel, M. Turowski, G. Margaritondo and P. Perfetti: Phys. Rev. B30 (1984) 6815.

29) T. Takahashi, H. Ohsawa, N. Gunasekara, T. Kinoshita,

H. Ishii, T. Sagawa, T. Miyahara and H. Kato:
Phys. Rev. B33 (1986) 1485.

30) O. Gunnarson and K. Schönhammer: Phys. Rev. B28 (1983) 4315, Phys. Rev. Lett. 50 (1983) 604, Phys. Rev. B31 (1985) 4815.

31) T. Nakano and A. Kotani: J. Phys. Soc. Jpn. 55 (1986) 2867.

32) A. Fujimori: Phys. Rev. B28 (1983) 2281, 4489.

33) A. Kotani and Y. Toyozawa: J. Phys. Soc. Jpn. 35 (1973) 1073.

34) G. Kaindl, G. Kalkowski, W. D. Brewer, E. V. Sampathkumaran, F. Holtzberg and A. Schach v. Wittenau:
J. Magn. and Magn. Mater. 47 & 48 (1985) 181.

35) W. -D. Schneider, B. Delley, E. Wuilloud, J. -M. Imer and Y. Baer: Phys. Rev. B32 (1985) 6819.

36) D. D. Koelling, A. M. Boring and J. H. Wood:
Solid State Commun. 47 (1983) 227.

37) E. Wuilloud, H. R. Moser, W. -D. Schneider and Y. Baer:
Phys. Rev. B28 (1983) 7354.

38) G. Krill, J. P. Kappler, A. Meyer, L. Abadi and M. F. Ravet: J. Phys. F11 (1981) 1713.

39) J. C. Fuggle, F. U. Hillebrecht, Z. Zołnierek, R. Lässer, Ch. Freiburg, O. Gunnarsson and K. Schönhammer:
Phys. Rev. B27 (1983) 7330.

40) F. U. Hillebrecht, J. C. Fuggle, G. A. Sawatzky, M. Campagna, O. Gunnarson and K. Schönhammer:
Phys. Rev. B30 (1984) 1777.

41) F. Patthey, B. Delly, W. -D. Schneider and Y. Baer:
Phys. Rev. Lett. 55 (1985) 1518.

42) Y. Baer, H. R. Ott, J. C. Fuggle and L. E. De Long:

Phys. Rev. B24 (1981) 5384.

43) J. W. Allen, S. -J. Oh, I. Lindau, J. M. Lawrence, L. I. Johannson and S. B. Hagström: Phys. Rev. Lett. 46 (1981) 1100.

44) L. I. Johansson, J. W. Allen, T. Gustafsson, I. Lindau and S. B. M. Hagström: Solid State Commun. 28 (1978) 53.

45) D. Wieliczka, J. H. Weaver, D. W. Lynch and C. G. Olson: Phys. Rev. B26 (1982) 7056.

46) D. M. Wieliczka, C. G. Olson and D. W. Lynch: Phys. Rev. B29 (1984) 3028.

47) J. W. Allen, S. -J. Oh, I. Lindau and L. I. Johansson: Phys. Rev. B29 (1984) 5927.

48) As a review of the electron spectroscopies for Ce compounds J. W. Allen, S. -J. Oh, O. Gunnarsson, K. Schönhammer, M. B. Maple, M. S. Torikachvili and I. Lindau: Adv. in Phys. 35 (1986) 275.

49) R. D. Parks, S. Raaen, M. L. den Boer, Y. -S. Chaug and G. P. Williams: J. Magn. and Magn. Mater. 47&48 (1985) 163.

50) A. Sakuma, Y. Kuramoto, T. Watanabe and C. Horie: J. Mag. and Mag. Mater. 52 (1985) 393.

51) A. Brown and S. Rundquist: Acta Cryst. 19 (1965) 684.

52) R. W. Keyes: Phys. Rev. 92 (1953) 580.

53) D. Warschauer: J. Appl. Phys. 34 (1963) 1853.

54) S. Sugai, T. Ueda and K. Murase: J. Phys. Soc. Jpn. 50 (1981) 3356.

55) Y. Fujii, Y. Akahama, S. Endo, S. Narita, Y. Yamada and G. Shirane: Solid State Commun. 44 (1982) 579.

56) T. Kikegawa and H. Iwasaki: Acta Cryst. B39 (1983) 158.

57) M. Ikezawa, Y. Kondo and I. Shirotani: J. Phys. Soc. Jpn. 52 (1983) 1518.

58) Y. Harada, K. Murano, I. Shirotani, T. Takahashi and Y. Maruyama: Solid State Commun. 44 (1982) 877.

59) M. Taniguchi, S. Suga, M. Seki, H. Sakamoto, H. Kanzaki, Y. Akahama, S. Terada, S. Endo and S. Narita: Solid State Commun. 45 (1983) 59.

60) T. Takahashi, K. Shirotani, S. Suzuki and T. Sagawa: Solid State Commun. 45 (1983) 945.

61) Y. Hayashi, T. Takahashi, H. Asahina, T. Sagawa, A. Morita and I. Shirotani: Phys. Rev. B30 (1984) 1891.

62) M. Taniguchi, S. Suga, M. Seki, A. Mikuni, S. Asaoka, H. Kanzaki, Y. Akahama, S. Endo and S. Narita: Phys. Rev. B28 (1983) 1165, Phys. Rev. B30 (1984) 4555.

63) H. Kawamura, I. Shirotani and K. Tachikawa: Solid State Commun. 49 (1984) 879.

64) Y. Takao, H. Asahina and A. Morita: J. Phys. Soc. Jpn. 50 (1981) 3362.

65) H. Asahina, K. Shindo and A. Morita: J. Phys. Soc. Jpn. 51 (1982) 1193.

66) M. Taniguchi: private communication.

67) J. Igarashi and T. Nakano: J. Phys. Soc. Jpn. 55 (1986) 1384.

Figure captions

Fig. 1 The crystal structure of Ce oxides.

(a) $CeO_2$ ($CaF_2$ type). Big and small circles represent O and Ce atoms, respectively.

(b) $Ce_2O_3$ ($La_2O_3$ type). Big and small circles represent O and Ce atoms, respectively. Shed circles are on the dot and dashed diagonal line of (c).

(c) A projection on its base of atoms in the hexagonal unit of $Ce_2O_3$. The smaller circles are Ce atoms.

Fig. 2 The impurity Anderson model using in this thesis.

(a) Meanings of parameters.

(b) Model for $CeO_2$.

(c) Model for $Ce_2O_3$.

Fig. 3 The experimental spectra of $CeO_2$ and $Ce_2O_3$ after ref. 18 and 34.

(a) The v-XPS and BIS. The upper line denotes $CeO_2$. A and B designate the position of a small peak.

(b) The 3d-XPS. The upper line denotes $CeO_2$.

(c) The 3d-XAS for $CeO_2$.

Fig. 4 The calculated v-XPS and BIS for $CeO_2$. The solid curve denotes parameter set A and the dashed curve denotes parameter set B (see text). The values of $\Gamma$ and $M_s$ are taken to be $0.2+0.2|E-E_F|$ eV and 1.5, respectively.

Fig. 5 The calculated 3d-XPS for $CeO_2$. The solid curve denotes parameter set A and the dashed curve denotes parameter set B (see text). The value of $\Gamma$ is taken to be 0.7 eV.

Fig. 6 The calculated 3d-XAS for $CeO_2$. The solid curve denotes

parameter set A and the dashed curve denotes parameter set B (see text). The value of $\Gamma$ is taken to be 0.7 eV.

Fig. 7 The dependence of the calculated 3d-XPS for $NxN_f+1$ electron system on the parameters V, $\varepsilon_f$, $U_{ff}$ and $U_{fc}$. The value of $\Gamma$ is taken to be 1.0 eV.

(a) V is changed with $U_{ff}$=9.1 eV, $U_{fc}$=12.0 eV and $\varepsilon_f$=2.0 eV.

(b) $\varepsilon_f$ is changed with V=0.6 eV, $U_{ff}$=9.1 eV and $U_{fc}$=12.0 eV.

(c) $U_{ff}$ is changed with V=0.6 eV, $U_{fc}$=12.0 eV and $\varepsilon_f$=2.0 eV.

(d) $U_{fc}$ is changed with V=0.6 eV, $U_{ff}$=9.1 eV and $\varepsilon_f$=2.0 eV.

Fig. 8 The calculated 3d-XPS for $Ce_2O_3$ with V=0.6 eV, $U_{ff}$=9.1 eV, $U_{fc}$=12.0 eV, $\varepsilon_f$=2.0 eV and $\Gamma$=1.0 eV.

Fig. 9 The calculated v-XPS and BIS for $Ce_2O_3$ with V=0.6 eV, $U_{ff}$=9.1 eV, $U_{fc}$=12.0 eV, $\varepsilon_f$=2.0, $\Gamma=0.2+0.2|E-E_F|$ eV and $M_s$=1.1.

Fig. 10 The dependence of the calculated v-XPS for $NxN_f+1$ electron system on $M_s$. The other parameter values are same as Fig. 9.

Fig. 11 The resonant photoemission CIS spectra for $CeO_2$ and $Ce_2O_3$ after ref. 18.

Fig. 12 The resonant photoemission EDC spectra for $\gamma$-Ce after ref. 44.

Fig. 13 The calculated CIS spectra for $CeO_2$at the valence band center with $\Gamma=0.2+0.2|E-E_F|$ eV, $\gamma$=2 eV and $M_s$=1.5.

(a) The spectra with the parameter set A (see text). Solid line is with q=1 and dashed line is with q=-1.

(b) The spectra with the parameter set B (see text). Solid line is with q=1 and dashed line is with q=-1.

(c) The spectra with $M_s$=0.0 and the parameter set A. Solid line is with q=1 and dashed line is with q=-1.

Fig. 14 The calculated CIS spectra for $Ce_2O_3$ at the lower energy peak (the valence band center) and the higher energy peak with $\gamma$=2 eV and q=2.

Fig. 15 Schematic representation of the basis states used. Solid circles show electrons and open circles show holes. The lines indicate which states couple to each other.

Fig. 16 The calculated EDC for $\gamma$-Ce with V=0.2 eV, $\varepsilon_f$=-0.6 eV, $U_{ff}$=5.5 eV, $U_{fc}$=9.5 eV, W=1.5 eV, $\Gamma$=0.25+0.1$|$ E-$E_F$ $|$ eV, $\gamma$=3 eV, q=2, $M_s$=0.7 and C=0.2 which is for the back ground (see text).

Fig. 17 The calculated CIS spectra for $\gamma$-Ce at the peaks in EDC with the same parameter values as Fig. 16.

Fig. 18 The calculated 3d-XPS and 3d-XAS for $\gamma$-Ce with the same parameter values as Fig. 16.

(a) The 3d-XPS.

(b) The 3d-XAS.

Fig. 19 The calculated v-XPS and BIS for $\gamma$-Ce with the same parameter values as Fig. 16.

Fig. 20 The experimental data for v-XPS, BIS and 3d-XPS in $\alpha$-Ce and $\gamma$-Ce after ref. 37 and 46.

(a) The v-XPS and BIS.

(b) The 3d-XPS.

Fig. 21 The calculated resonant photoemission spectra by use of $CeO_2$ type basis wave functions with the same parameter values as Fig. 16.

(a) The EDC.

(b) The CIS spectra at each peak in the EDC.

Fig. 22 The calculated 3d-XPS and 3d-XAS by use of $CeO_2$ type basis wave functions with the same parameter values as Fig. 16.

Fig. 23 The calculated v-XPS and BIS by use of $CeO_2$ type basis wave functions with the same parameter values as Fig. 16.

Fig. 24 The crystal structure of black phosphorus.

Fig. 25 The band structure and the density of states of black phosphorus after ref. 65.

Fig. 26 Model of energy bands for black phosphorus.

Fig. 27 Density of states of the conduction band (solid line) modified by the core hole potential u (u=-1.25 eV), in comparison with that for u=0 eV (broken line).

Fig. 28 Photoemission CIS spectra of $I_1(\omega,\varepsilon)$ at $E_B$=2.5 eV for various parameter values.

(a) q is changed with $\kappa$=0.5, u=-2.5 eV and $\Gamma$=0.2 eV.

(b) q is changed with $\kappa$=50, u=-2.5 eV and $\Gamma$=0.2 eV.

(c) u is changed with $\kappa$=900, q=-150 and $\Gamma$=0.2 eV.

(d) $\Gamma$ is changed with $\kappa$=900, q=-150 and u=-1.25 eV.

Fig. 29 Photoemission CIS spectra of $I_2(\omega,\varepsilon)$ at $E_B$=10.4 eV for various parameter values.

(a) $\kappa$ and q are changed with u=-1.25 eV and $\Gamma$=0.2 eV.

(b) u is changed with $\Gamma$=0.2 eV.

(c) $\Gamma$ is changed with u=-1.25 eV.

In (b) and (c), $\kappa$ and q are fixed at 900 and -150, respectively.

Fig. 30 Photoemission CIS spectra of $I(\omega,\varepsilon)$ at $E_B$=2.5 eV and 10.4 eV, with $\kappa$=900, q=-150, u=-1.25 eV and $\Gamma$=0.2 eV. The experimental CIS spectra are shown in the inset after Fig. 3 in ref. 29.

Fig. 31 The experimental data of EDC in black phosphorus after Fig. 2 in ref. 29.

Fig. 32 Photoemission energy distribution curves of $I(\omega,\varepsilon)$ for various photon energies. The parameter values are the same as Fig. 28.

Fig. 33 Photoemission energy distribution curve of $I_2(\omega,\varepsilon)$ at $\omega$=130.6 eV. The CIS spectrum of $I_2(\omega,\varepsilon)$ at $E_B$=2.5 eV is shown in the inset.

Fig. 34 The experimental and calculated spectra of yield in black phosphorus.

(a) The experimental spectrum of yield after Fig. 8 in ref. 62.

(b) The calculated photoabsorption spectrum with taking into account two component of the core exciton at each threshold.

Table 1. The 4f configurations in order to describe the various basis wave functions, and their symmetry.

| | spectrum | ground state | final state |
|---|---|---|---|
| $CeO_2$ | 3d-XPS | $f^0, f^1, f^2$ (singlet) | $f^0, f^1, f^2, f^3$ (singlet) |
| | v-XPS | | $f^0, f^1, f^2$ (spin doublet) |
| | BIS | | $f^1, f^2, f^3$ (spin doublet) |
| $Ce_2O_3$ | 3d-XPS | $f^1, f^2, f^3$ (spin doublet) | $f^1, f^2, f^3$ (spin doublet) |
| | v-XPS | | $f^0, f^1, f^2$ (singlet) $f^1, f^2$ (other symmetry) |
| | BIS | | $f^2, f^3, f^4$ (other symmetry) |

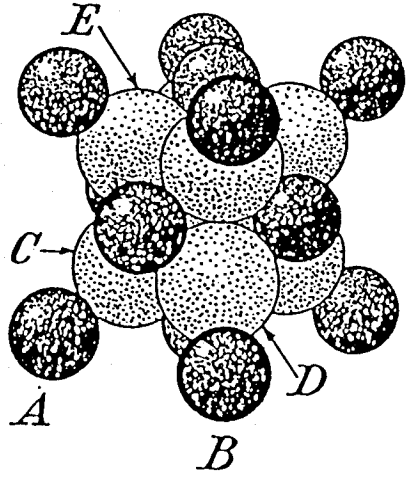


(a)

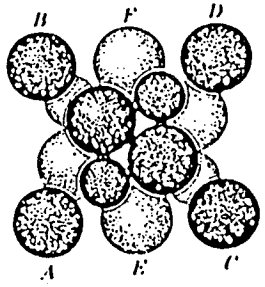


(b)

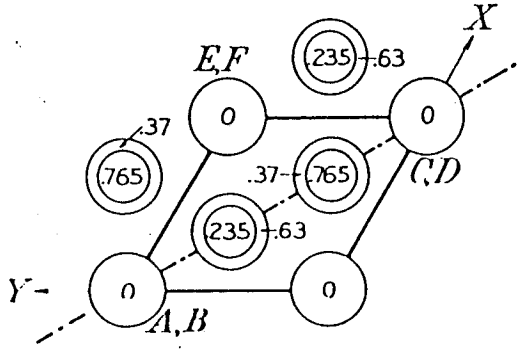


(c)

Fig.1

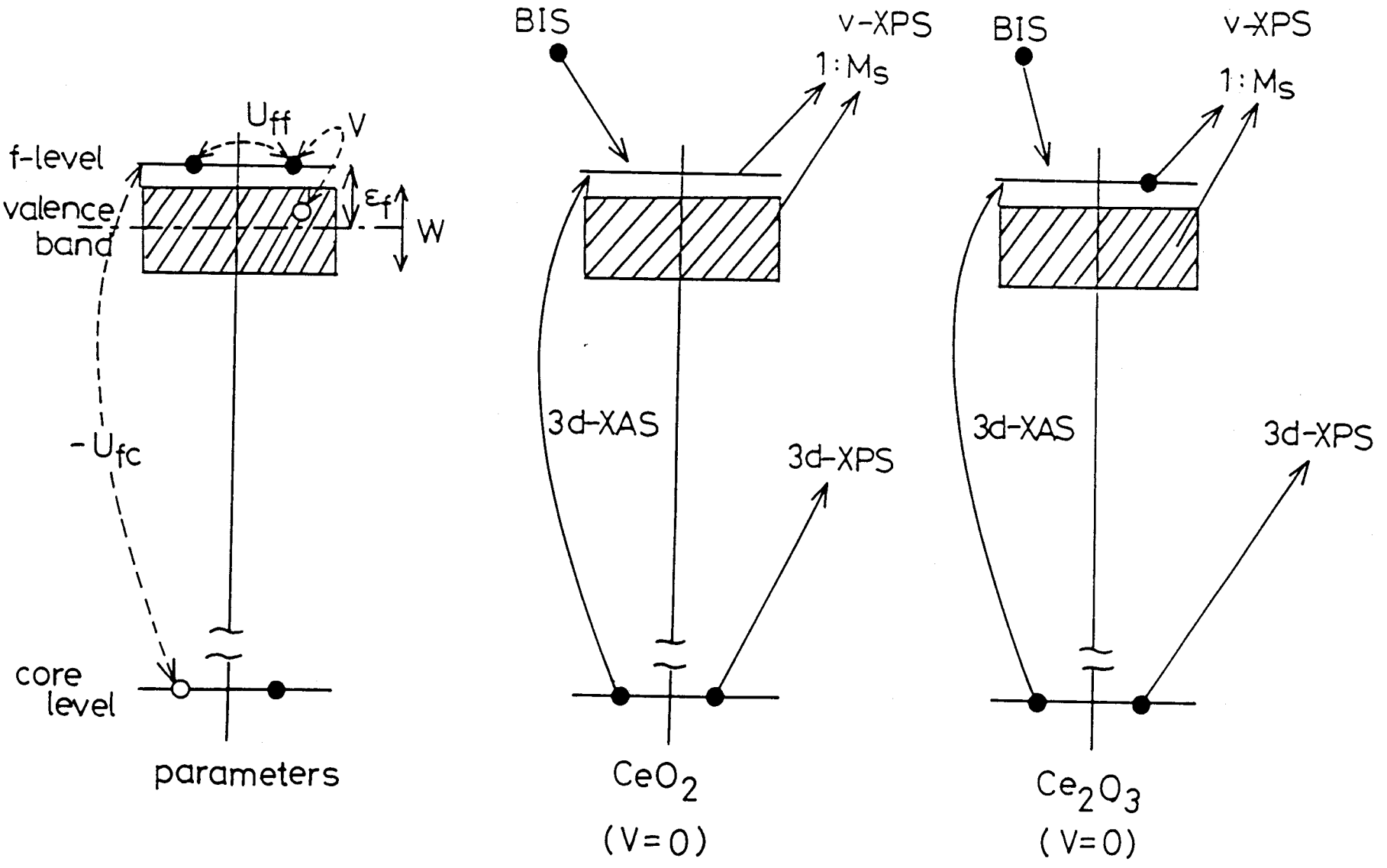
f-level
valence band
$U_{ff}$
V
$\varepsilon_f$
W
$-U_{fc}$
core level
parameters
BIS
v-XPS
1 : $M_s$
3d-XAS
3d-XPS
$CeO_2$
(V=0)
BIS
v-XPS
1 : $M_s$
3d-XAS
3d-XPS
$Ce_2O_3$
(V=0)

Fig.2

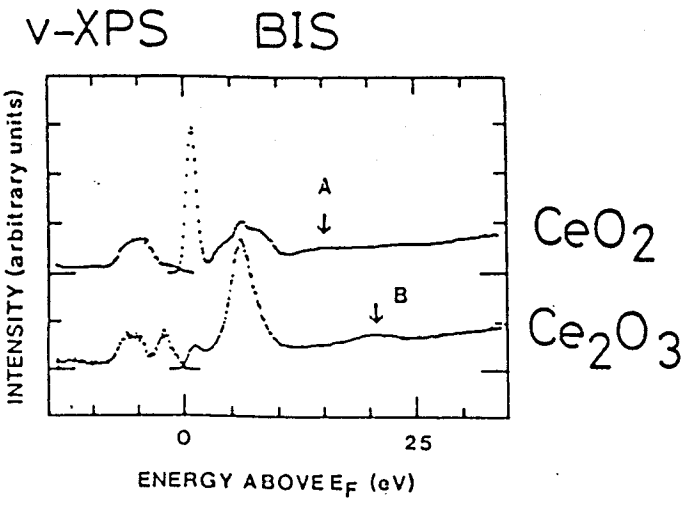
v-XPS
BIS
INTENSITY (arbitrary units)
A
B
CeO2
Ce2O3
0
25
ENERGY ABOVE EF (eV)

(a)

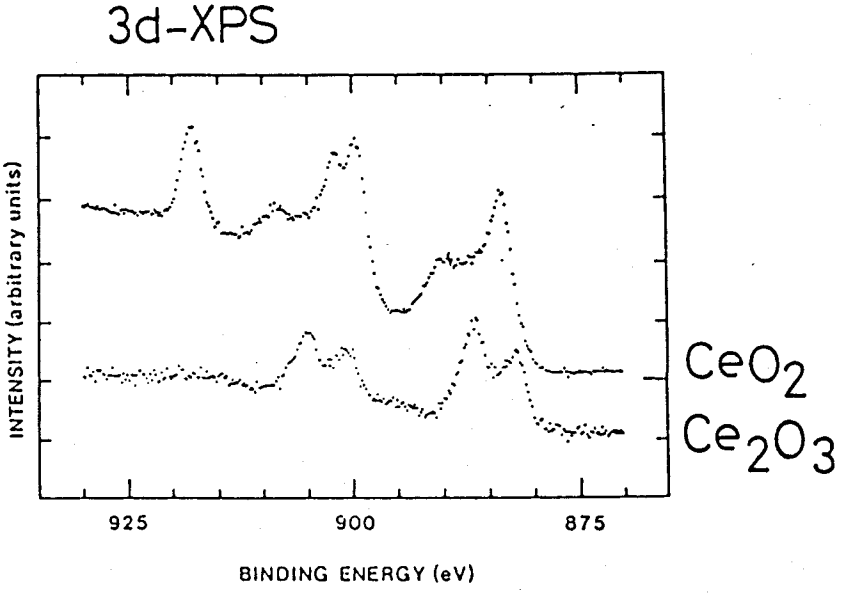
3d-XPS
INTENSITY (arbitrary units)
CeO2
Ce2O3
925
900
875
BINDING ENERGY (eV)

(b)

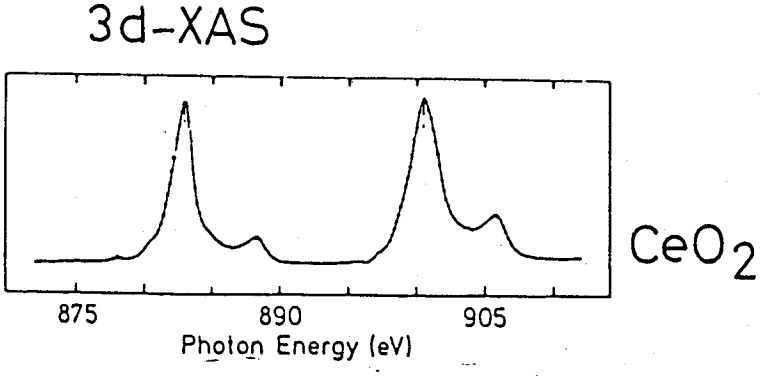
3d-XAS
CeO2
875
890
905
Photon Energy (eV)

(c)

Fig. 3

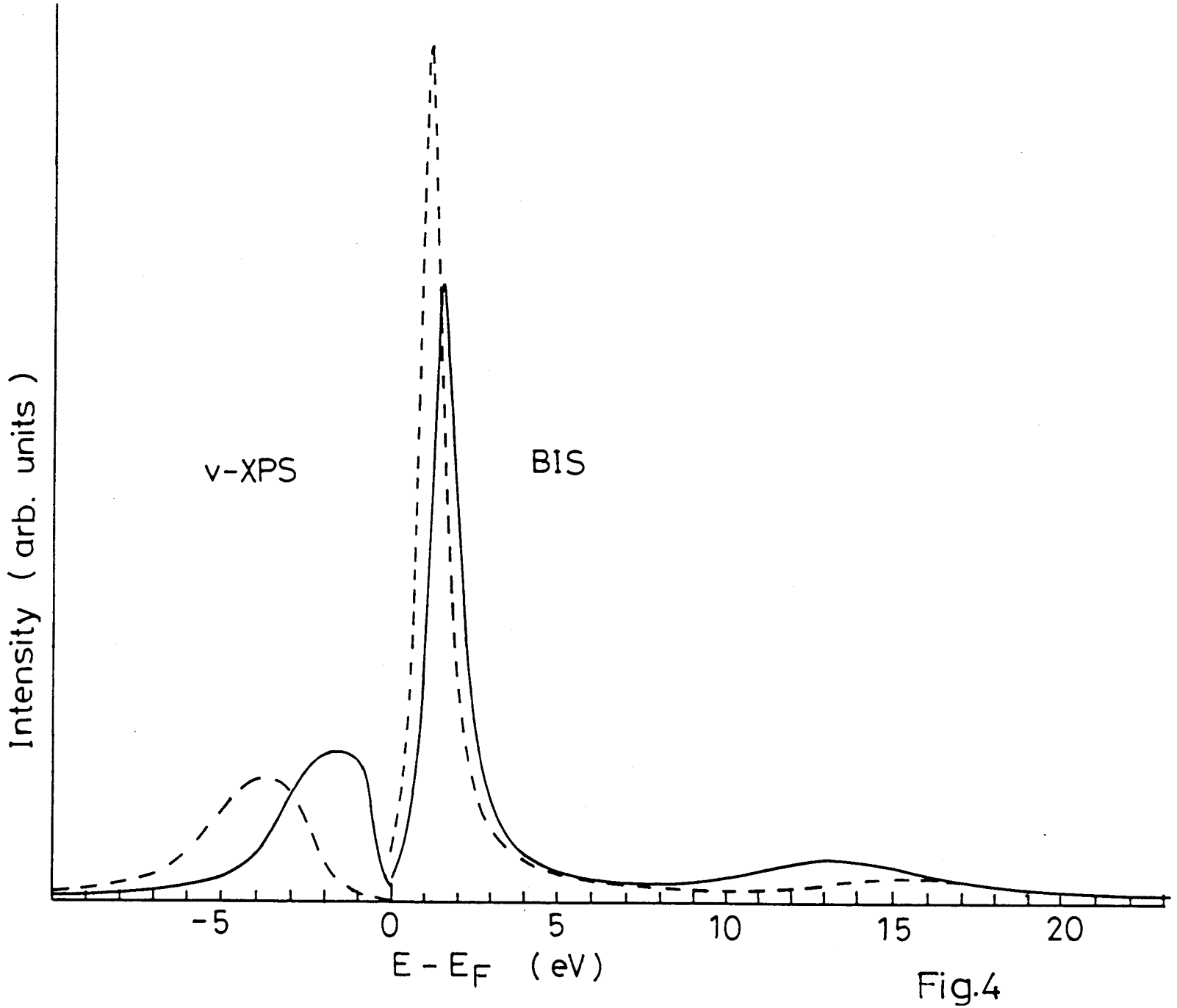


Fig.4

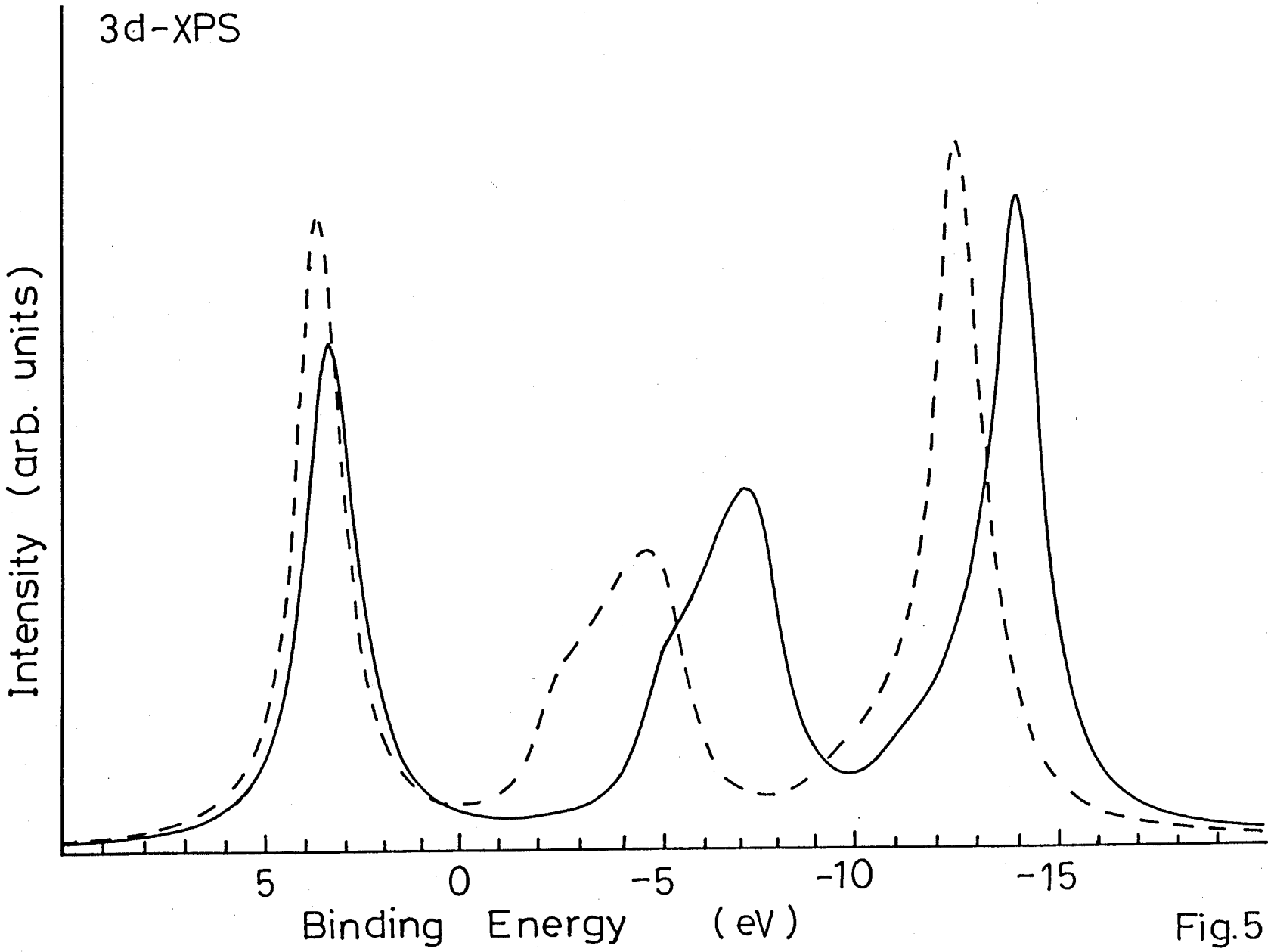


Fig.5

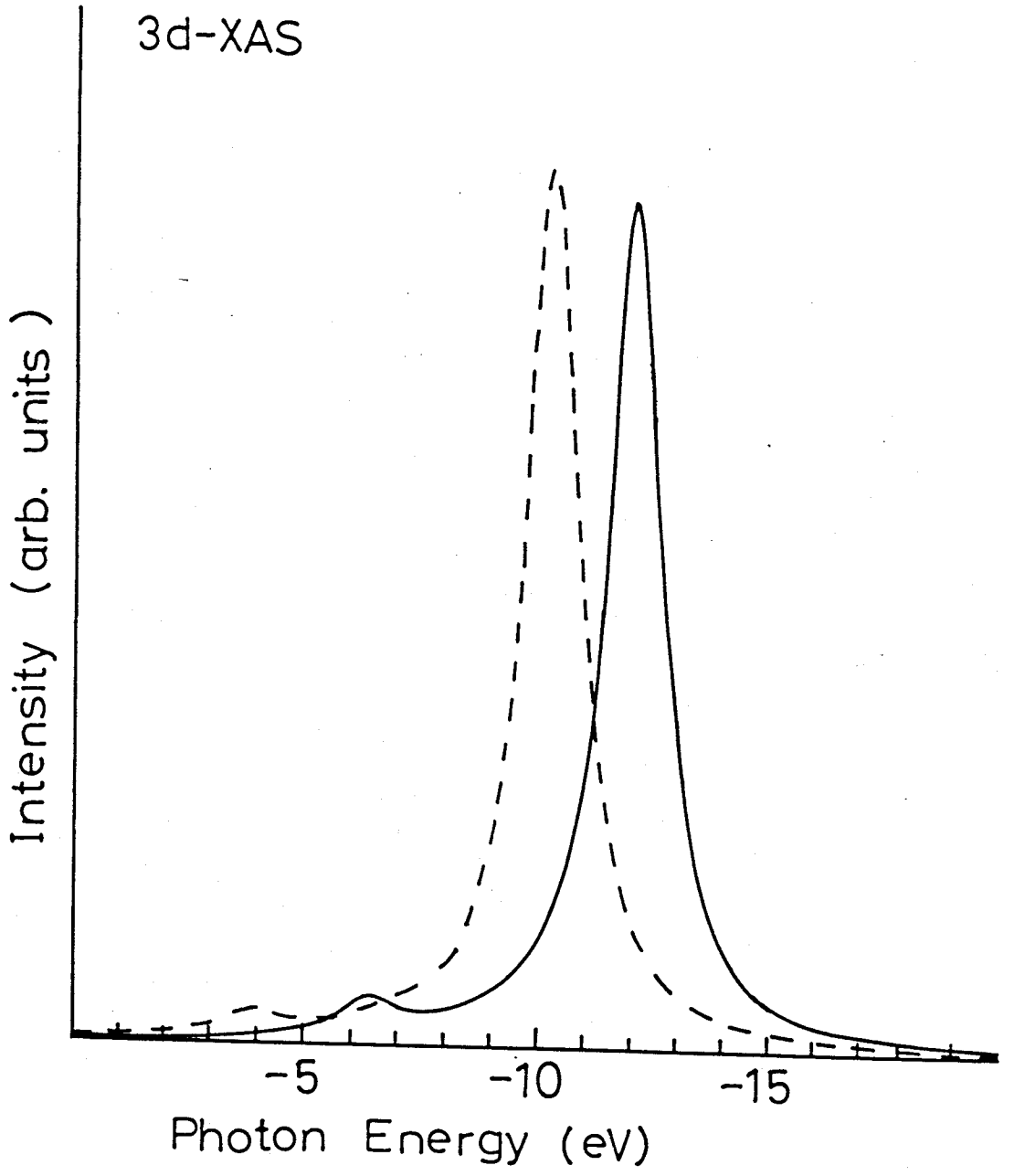


Fig.6

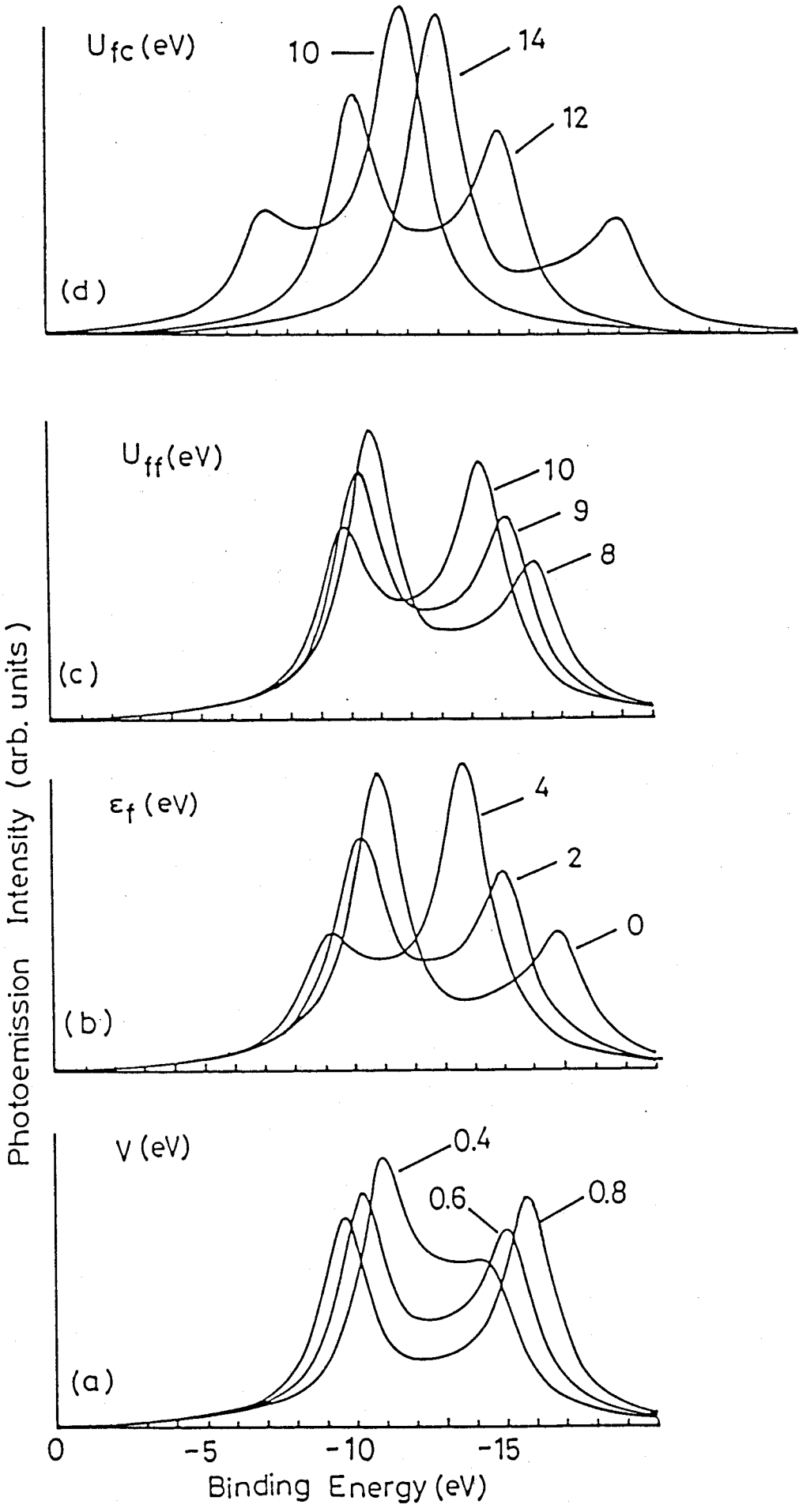
$U_{fc}$ (eV)
10
14
12
(d)
$U_{ff}$ (eV)
10
9
8
(c)
$\varepsilon_f$ (eV)
4
2
0
(b)
V (eV)
0.4
0.6
0.8
(a)
Photoemission Intensity (arb. units)
0
-5
-10
-15
Binding Energy (eV)

Fig.7

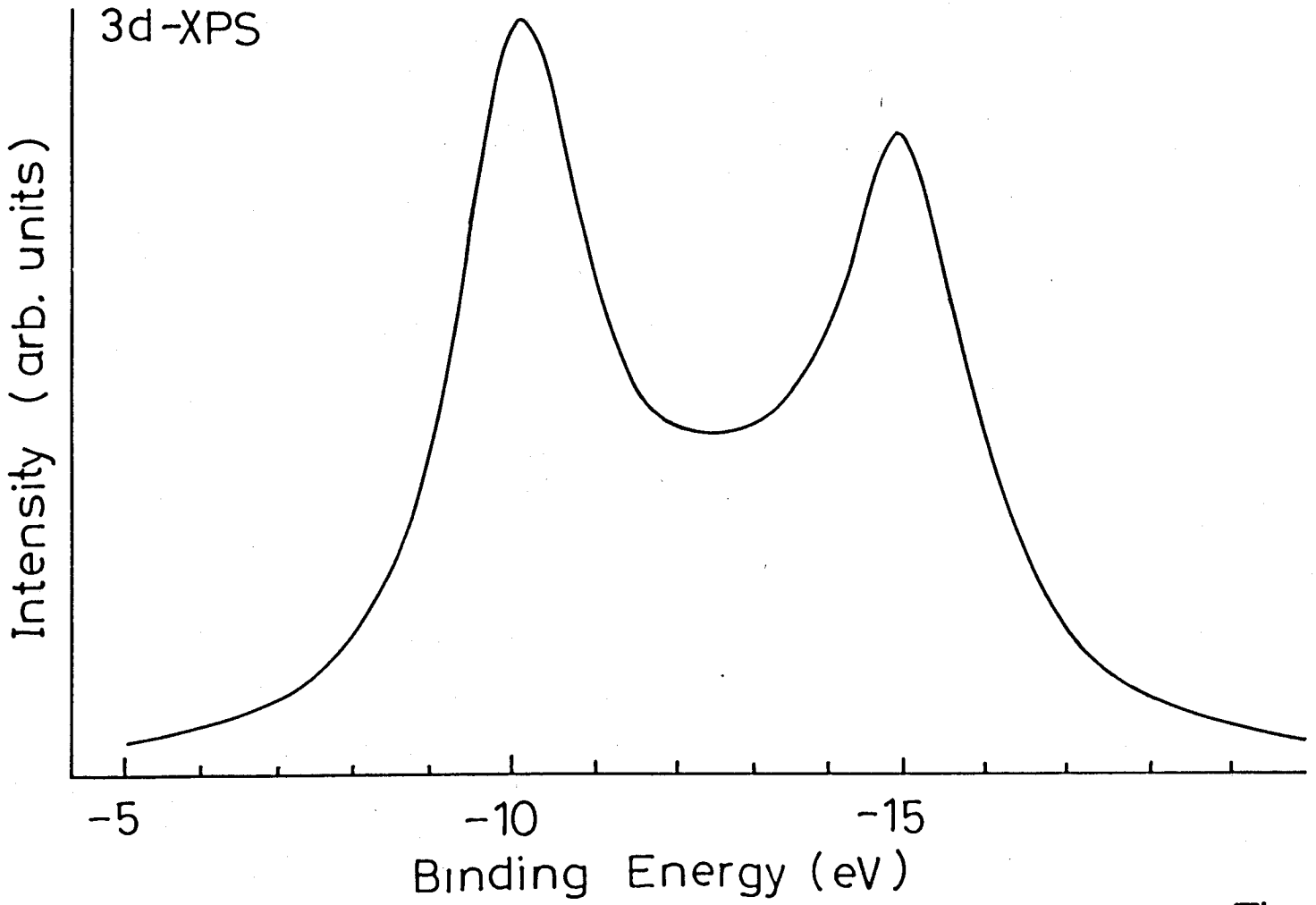


Fig.8

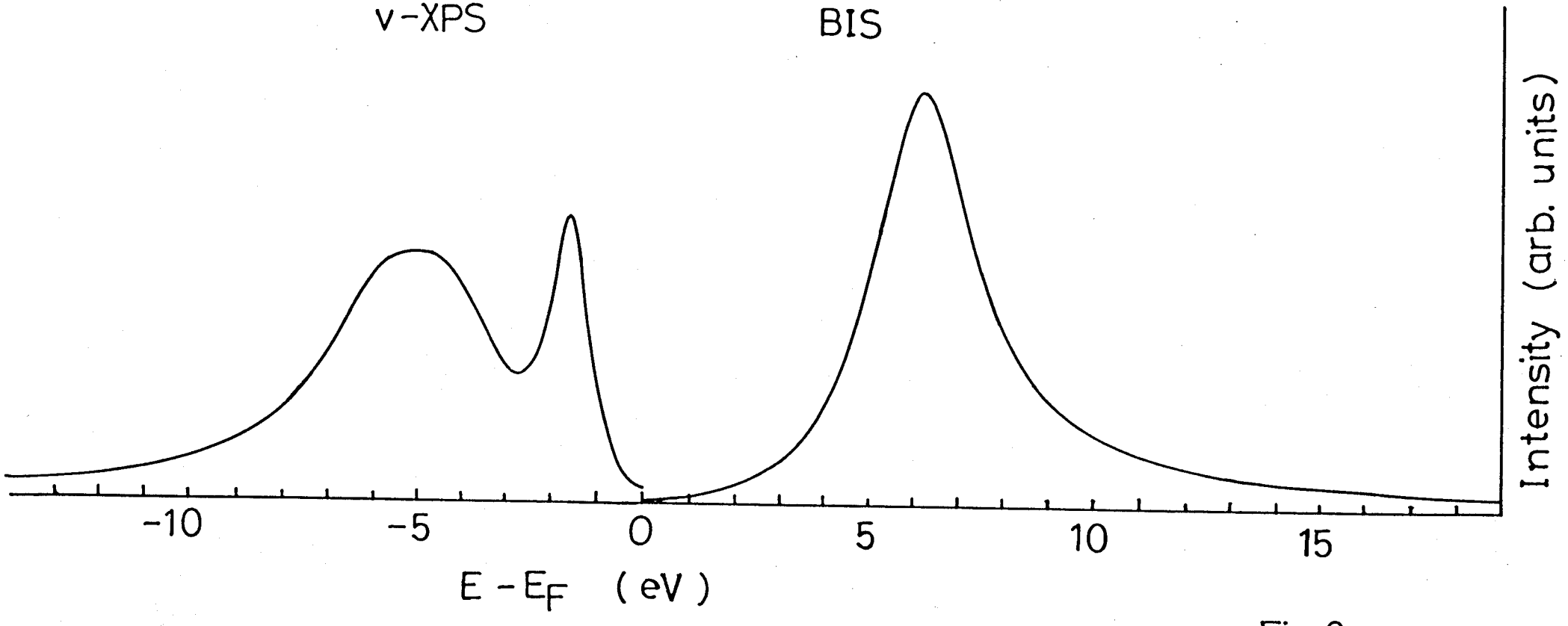


Fig.9

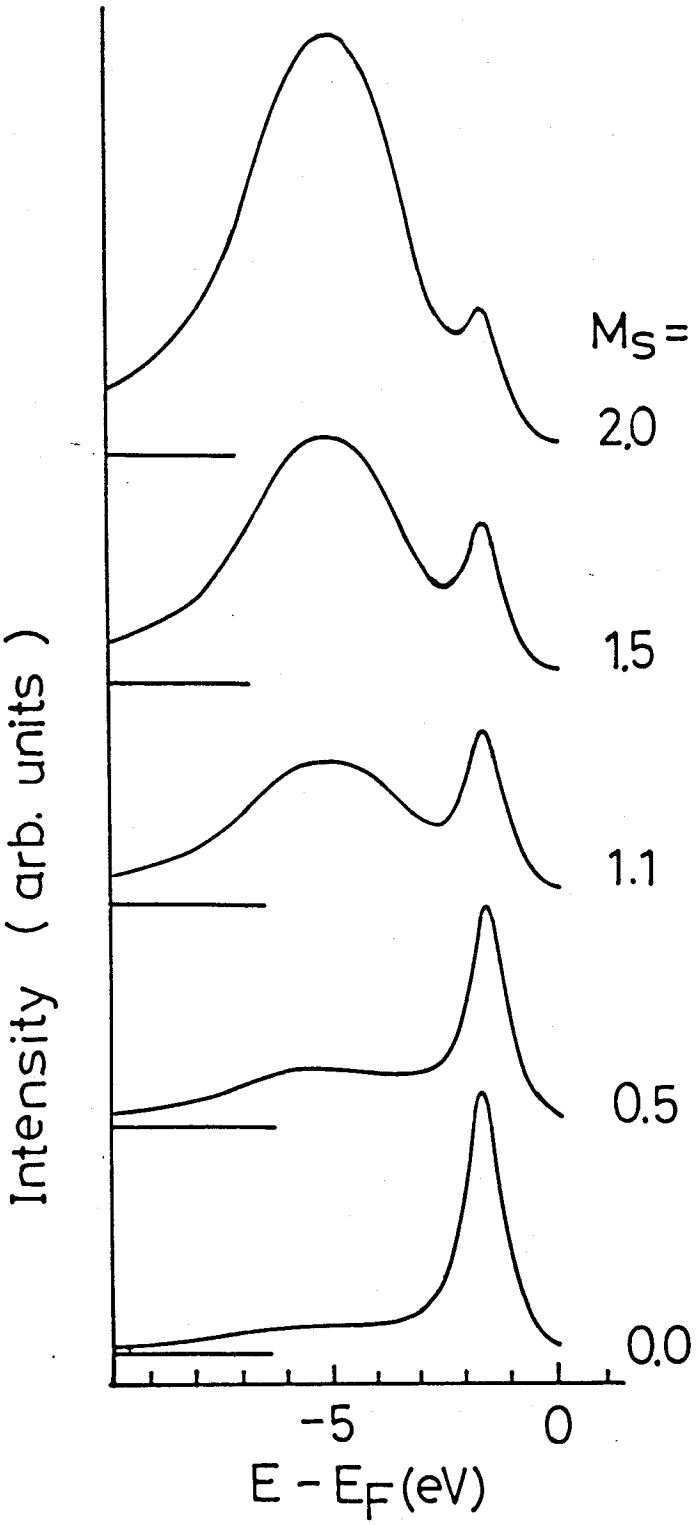


Fig.10

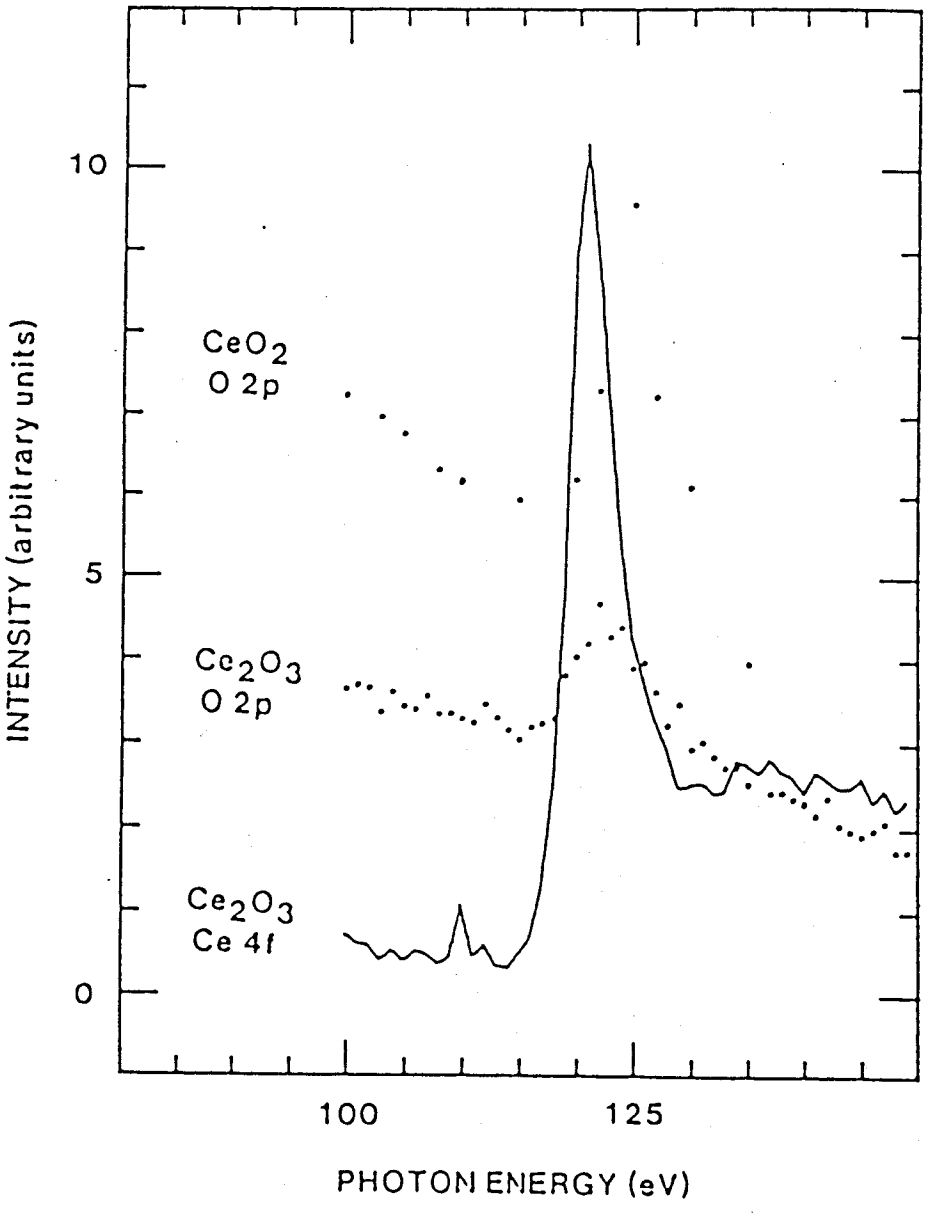
10
5
0
INTENSITY (arbitrary units)
CeO2
O 2p
Ce2O3
O 2p
Ce2O3
Ce 4f
100
125
PHOTON ENERGY (eV)

Fig. 11

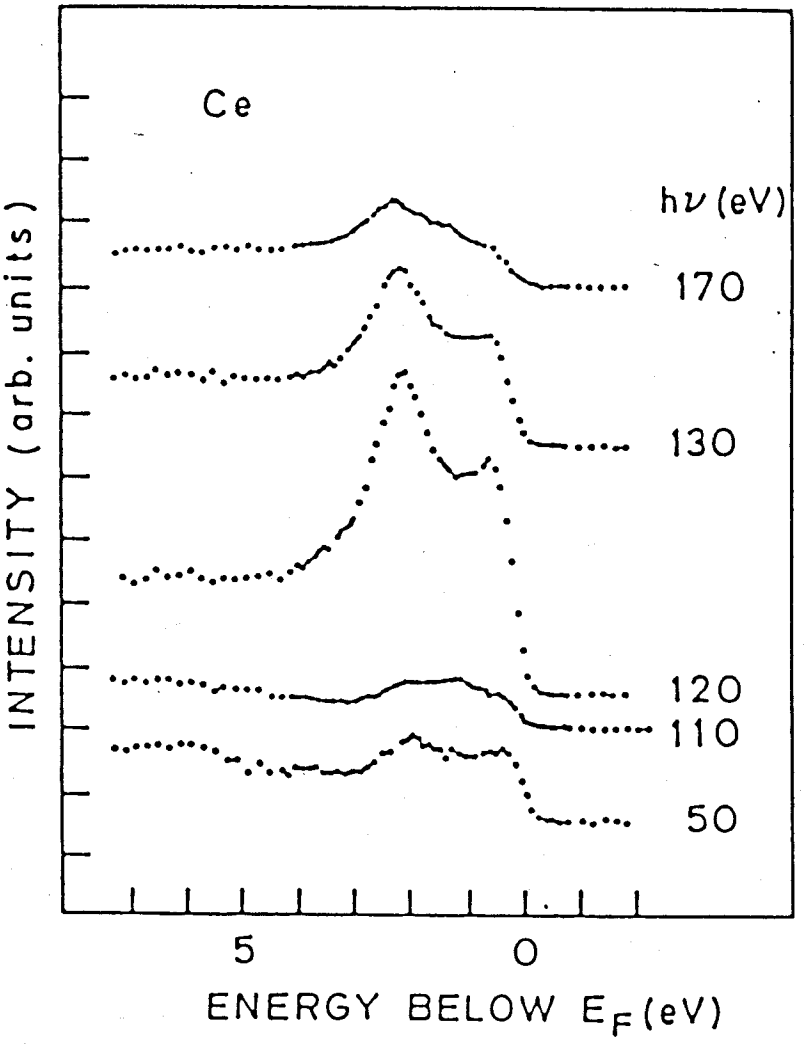
Ce
hν (eV)
170
130
120
110
50
INTENSITY (arb. units)
5
0
ENERGY BELOW $E_F$ (eV)

Fig.12

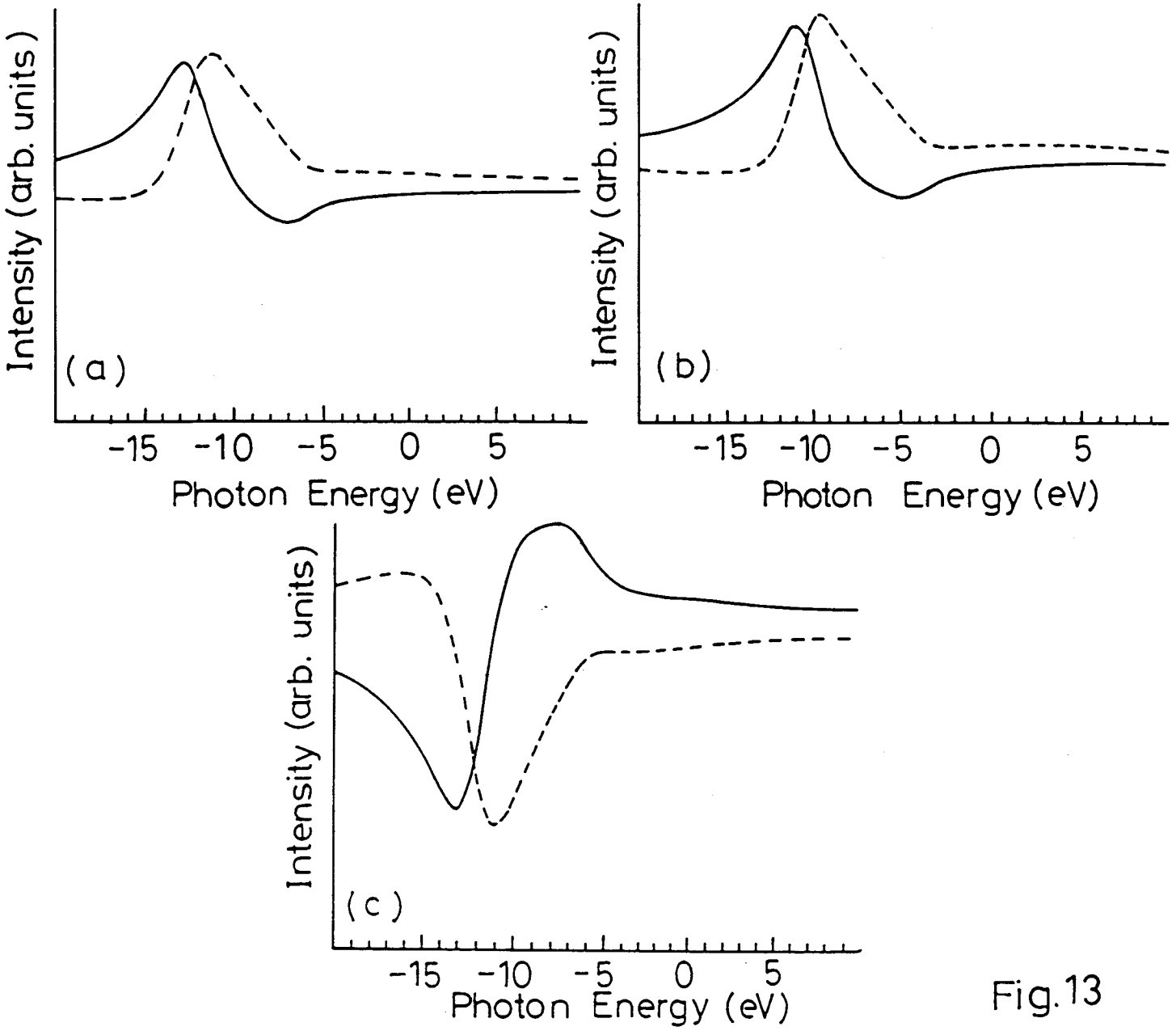
Intensity (arb. units)
(a)
-15 -10 -5 0 5
Photon Energy (eV)
Intensity (arb. units)
(b)
-15 -10 -5 0 5
Photon Energy (eV)
Intensity (arb. units)
(c)
-15 -10 -5 0 5
Photon Energy (eV)

Fig.13

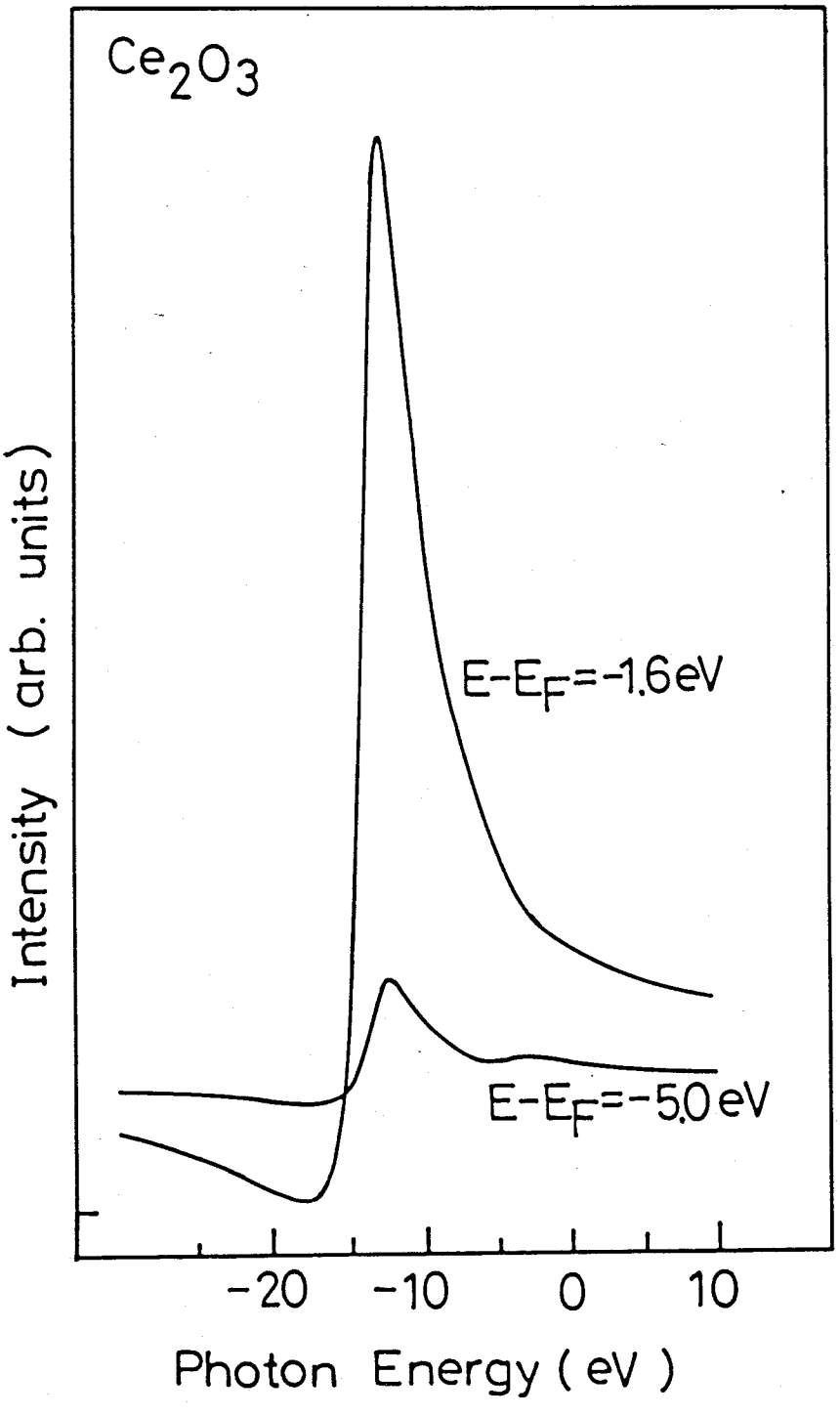
Ce2O3
E-EF=-1.6eV
E-EF=-5.0eV
Intensity ( arb. units)
-20
-10
0
10
Photon Energy ( eV )

Fig. 14

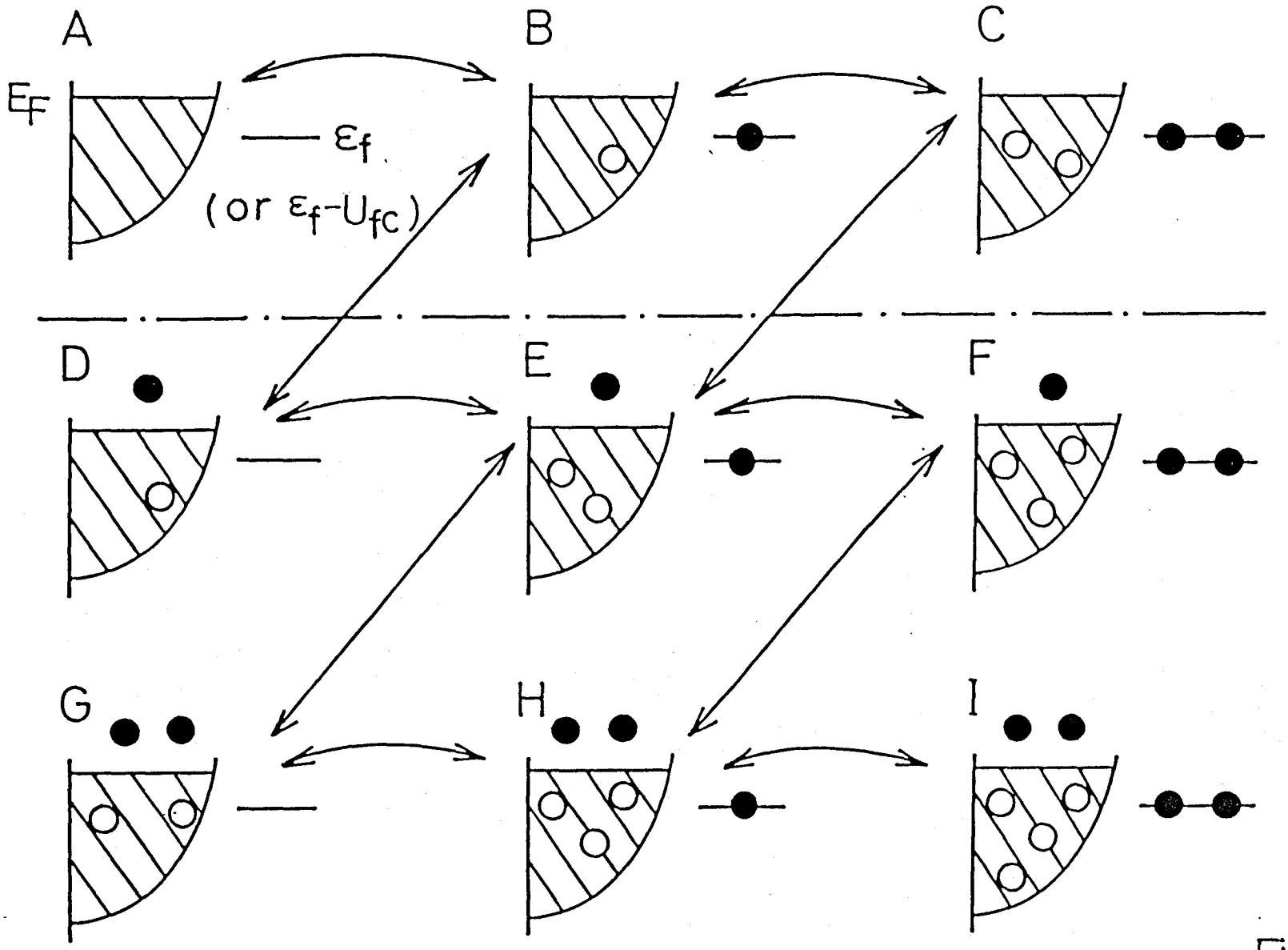


Fig.15

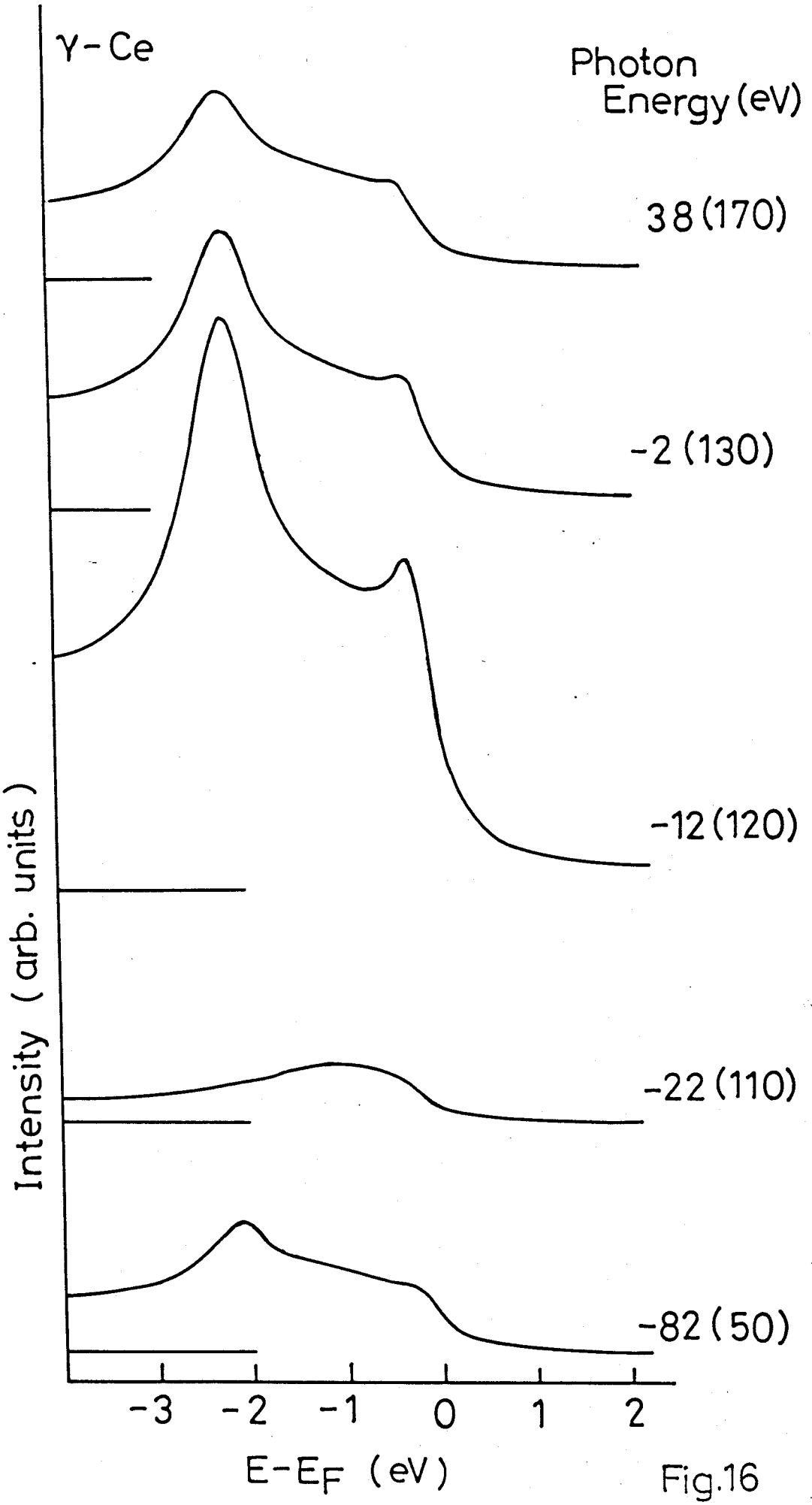
γ-Ce
Photon Energy (eV)
38 (170)
-2 (130)
-12 (120)
-22 (110)
-82 (50)
Intensity (arb. units)
-3
-2
-1
0
1
2
E-E_F (eV)

Fig.16

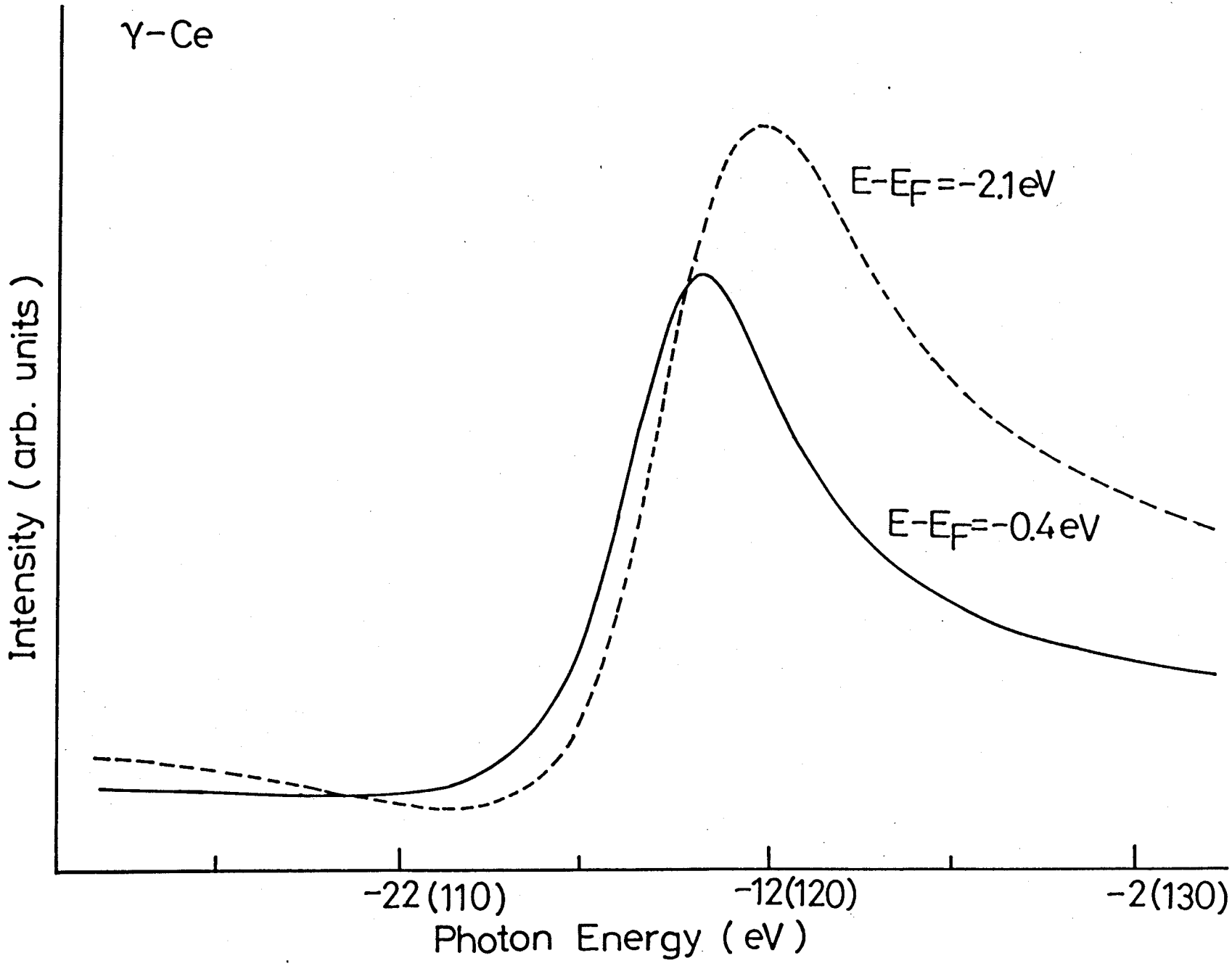
γ-Ce
E-E_F=-2.1eV
E-E_F=-0.4eV
Intensity ( arb. units )
-22 (110)
-12(120)
-2(130)
Photon Energy ( eV )

Fig.17

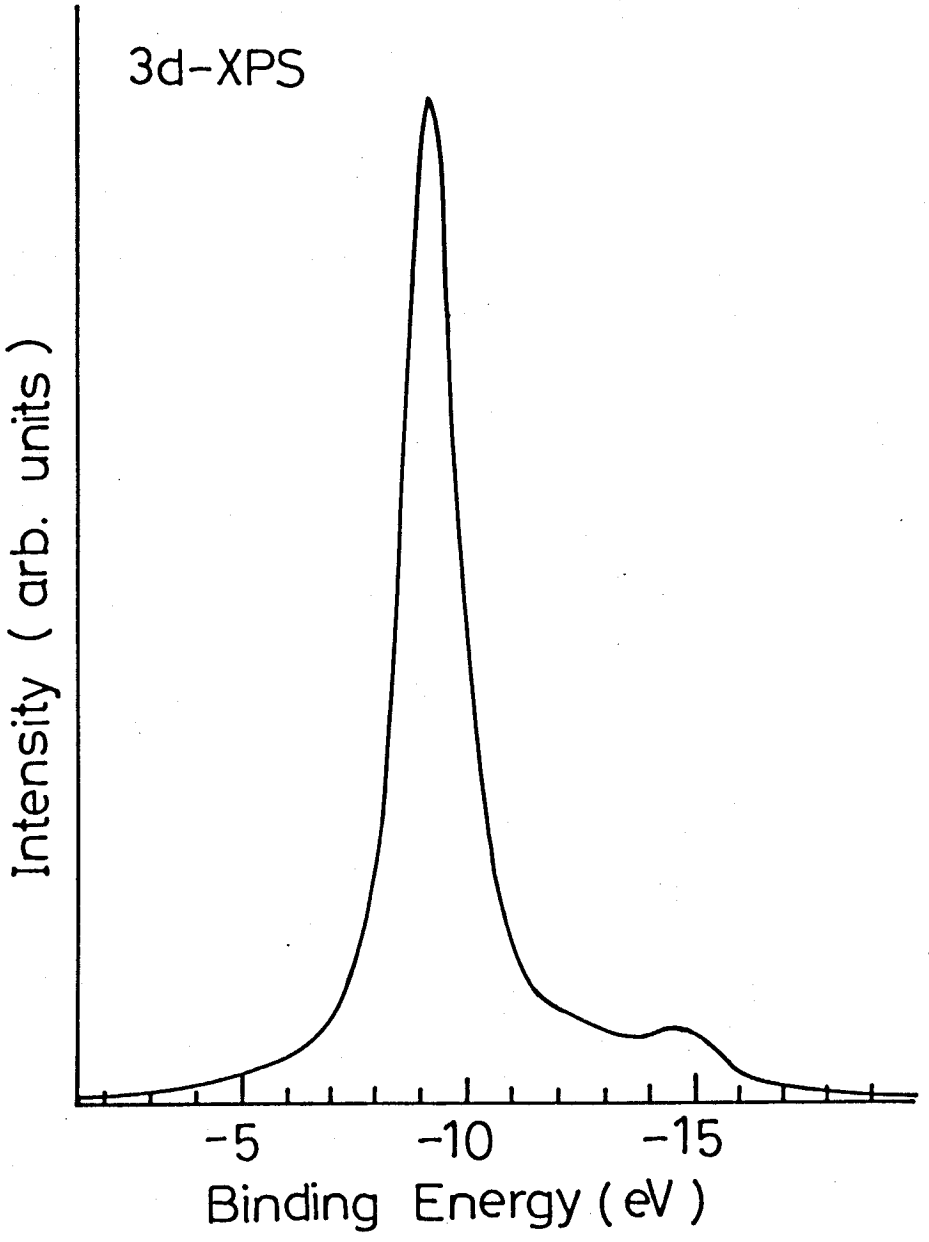
3d-XPS
Intensity ( arb. units )
-5
-10
-15
Binding Energy ( eV )

( a )

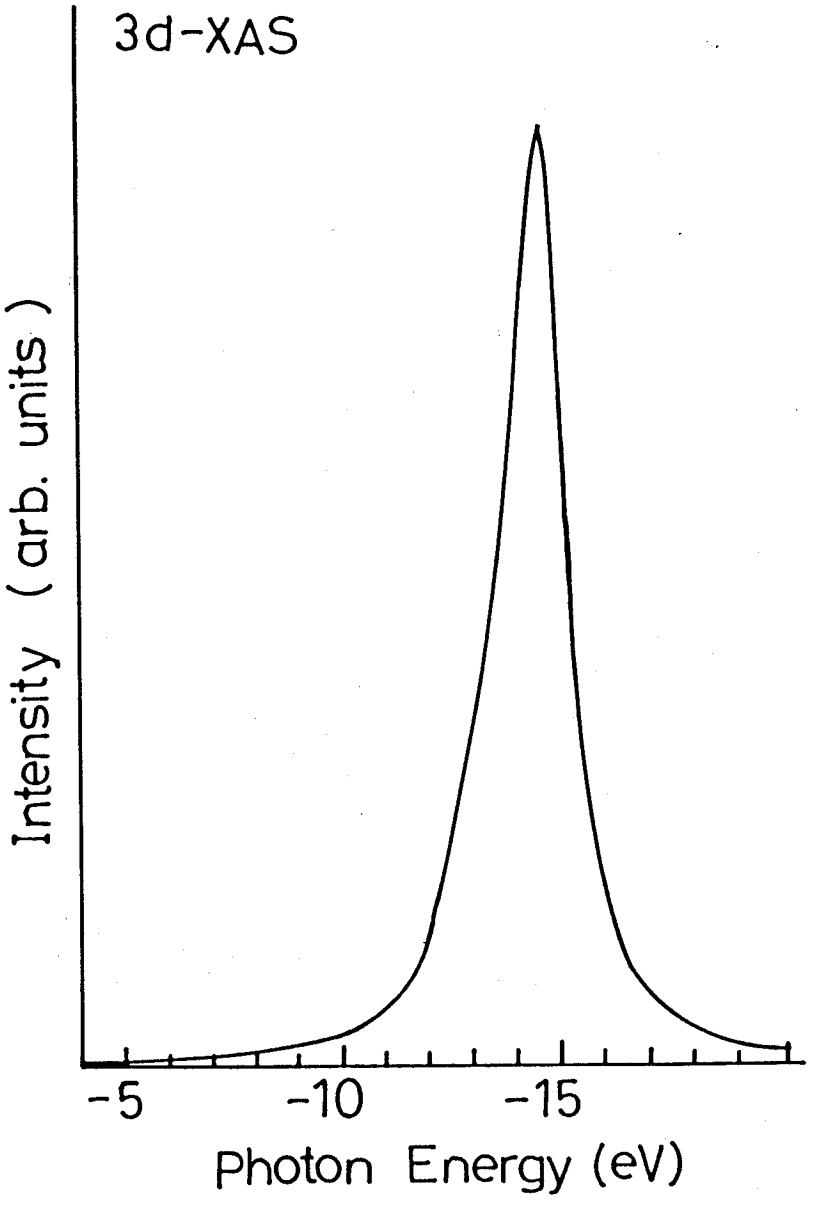
3d-XAS
Intensity ( arb. units )
-5
-10
-15
Photon Energy (eV)

( b )

Fig.18

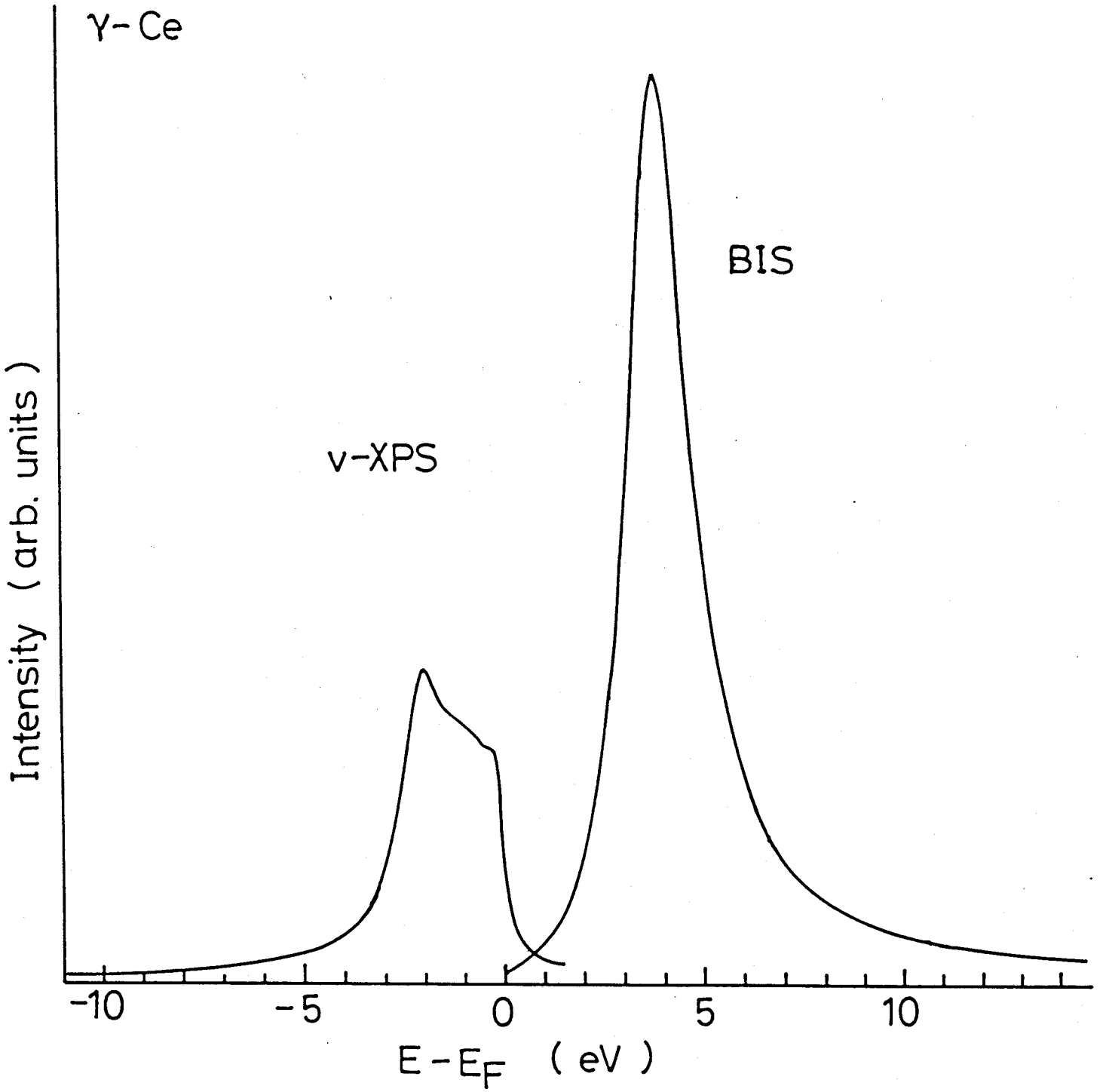


Fig. 19

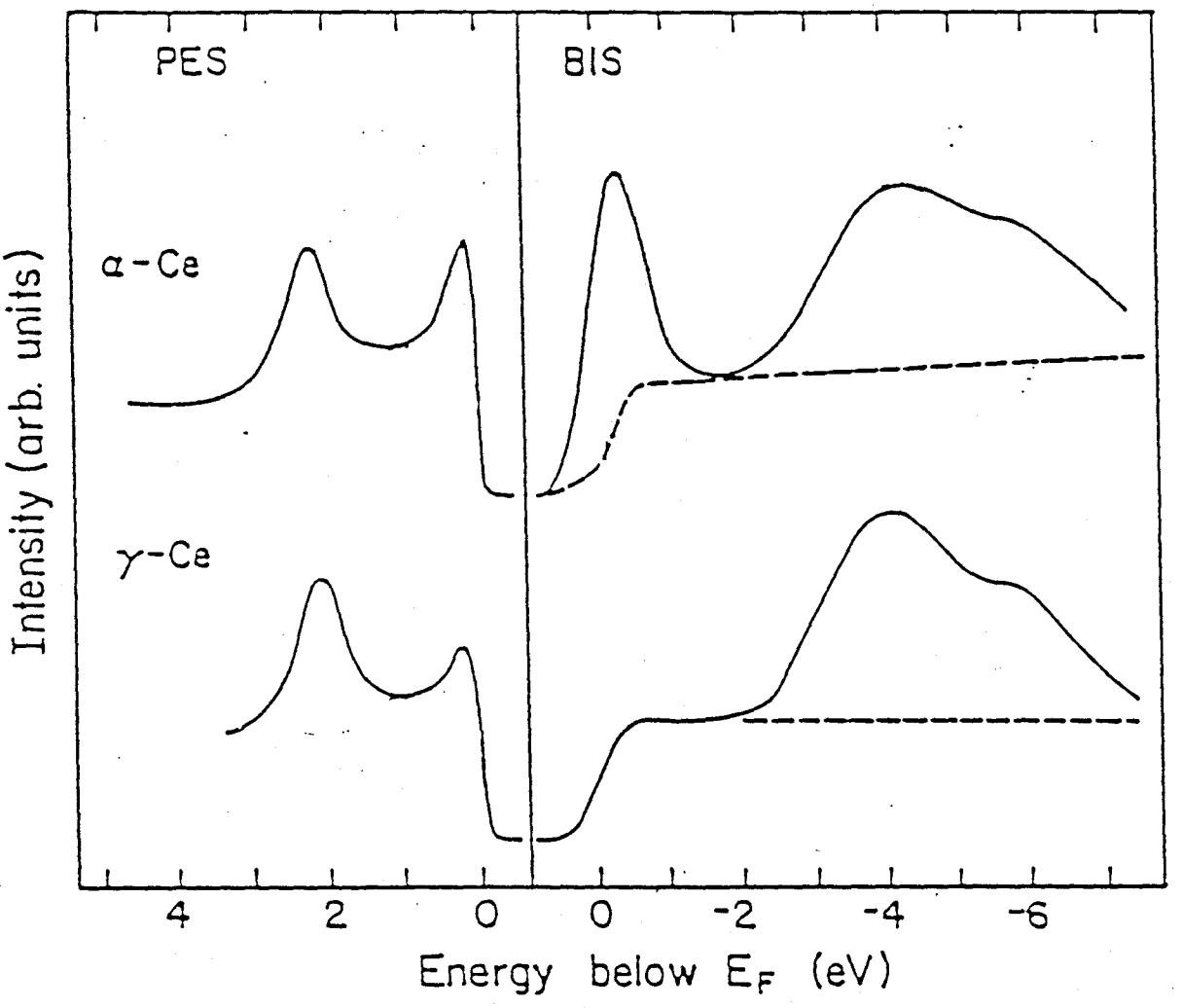
PES
BIS
α-Ce
γ-Ce
Intensity (arb. units)
4
2
0
0
-2
-4
-6
Energy below $E_F$ (eV)

(a)

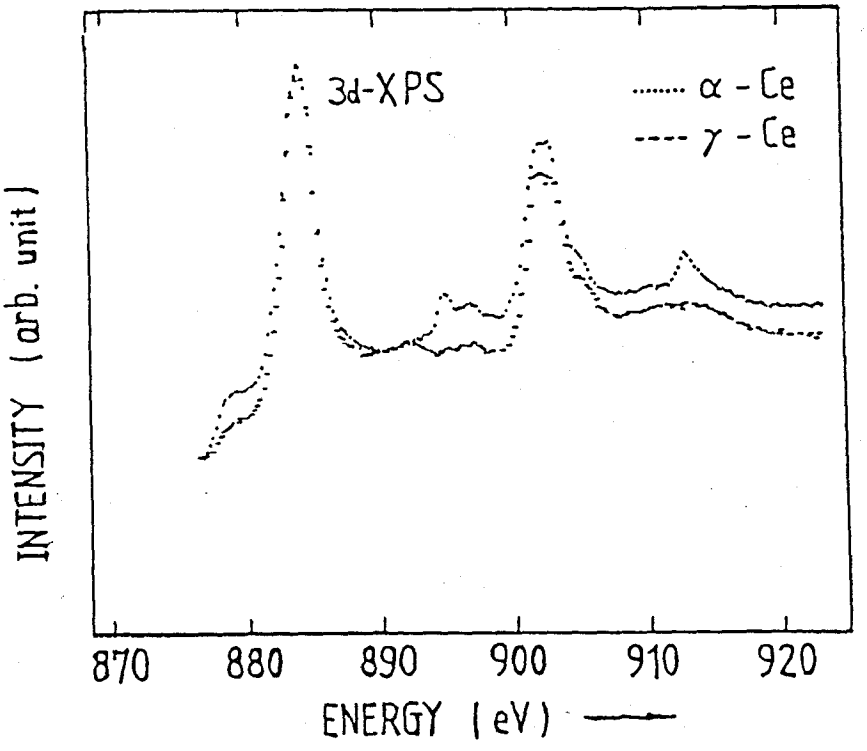
3d-XPS
α - Ce
γ - Ce
INTENSITY (arb. unit)
870
880
890
900
910
920
ENERGY (eV)

(b)

Fig. 20

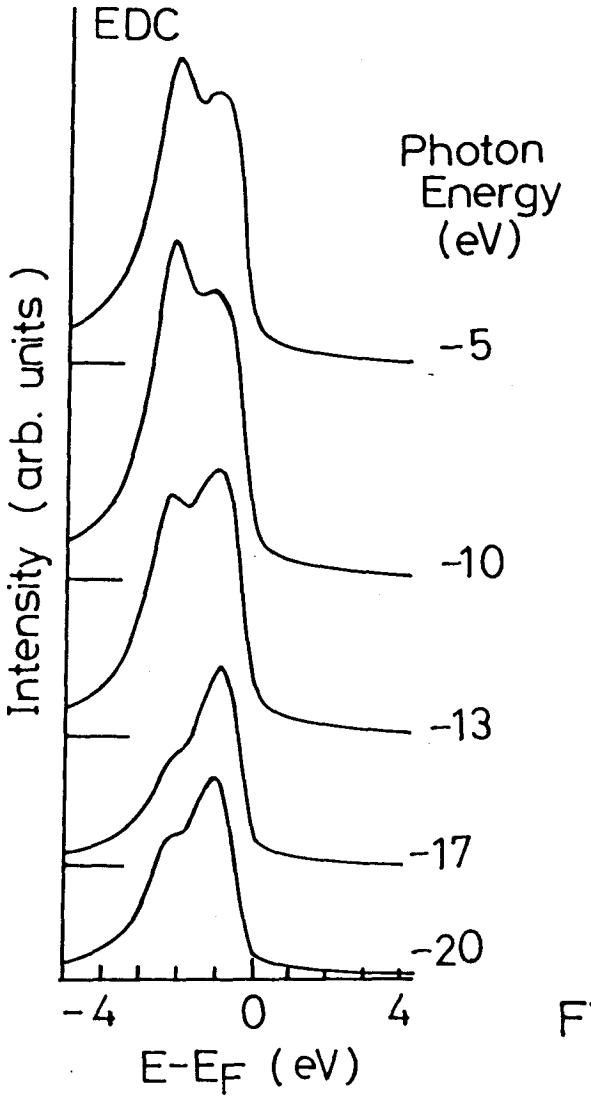
EDC
Photon
Energy
(eV)
-5
-10
-13
-17
-20
Intensity (arb. units)
-4
0
4
E-E_F (eV)

Fig.21

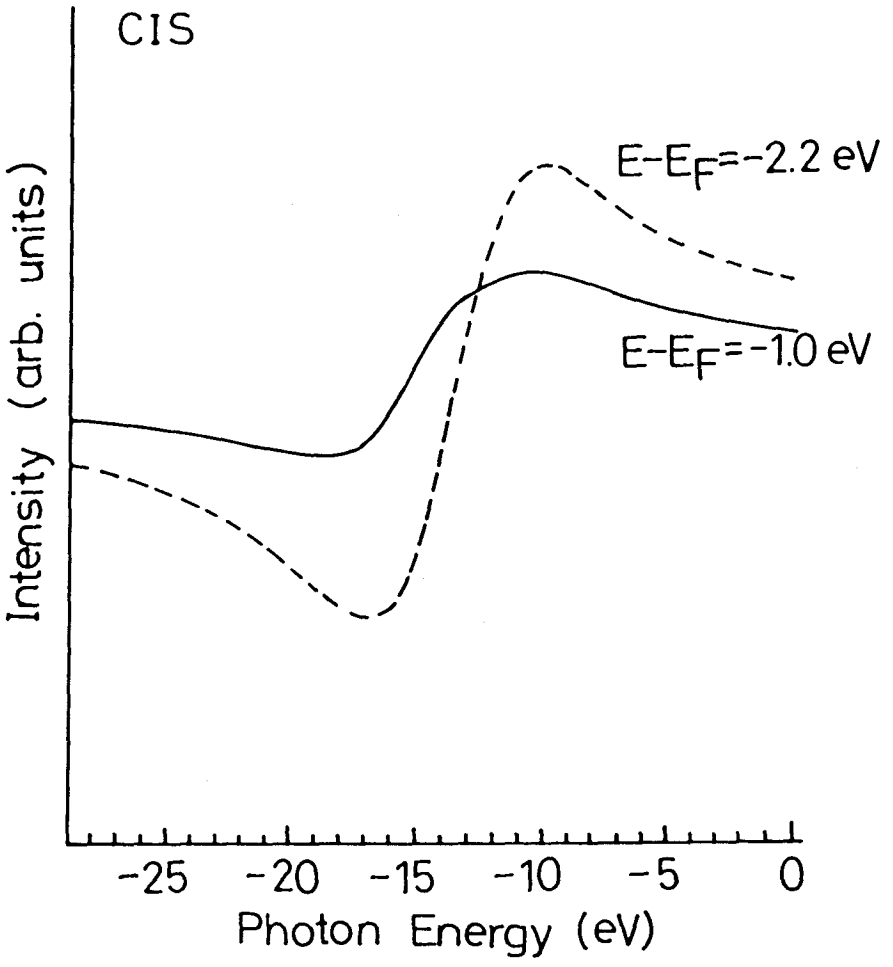
CIS
E-E_F=-2.2 eV
E-E_F=-1.0 eV
Intensity (arb. units)
-25
-20
-15
-10
-5
0
Photon Energy (eV)

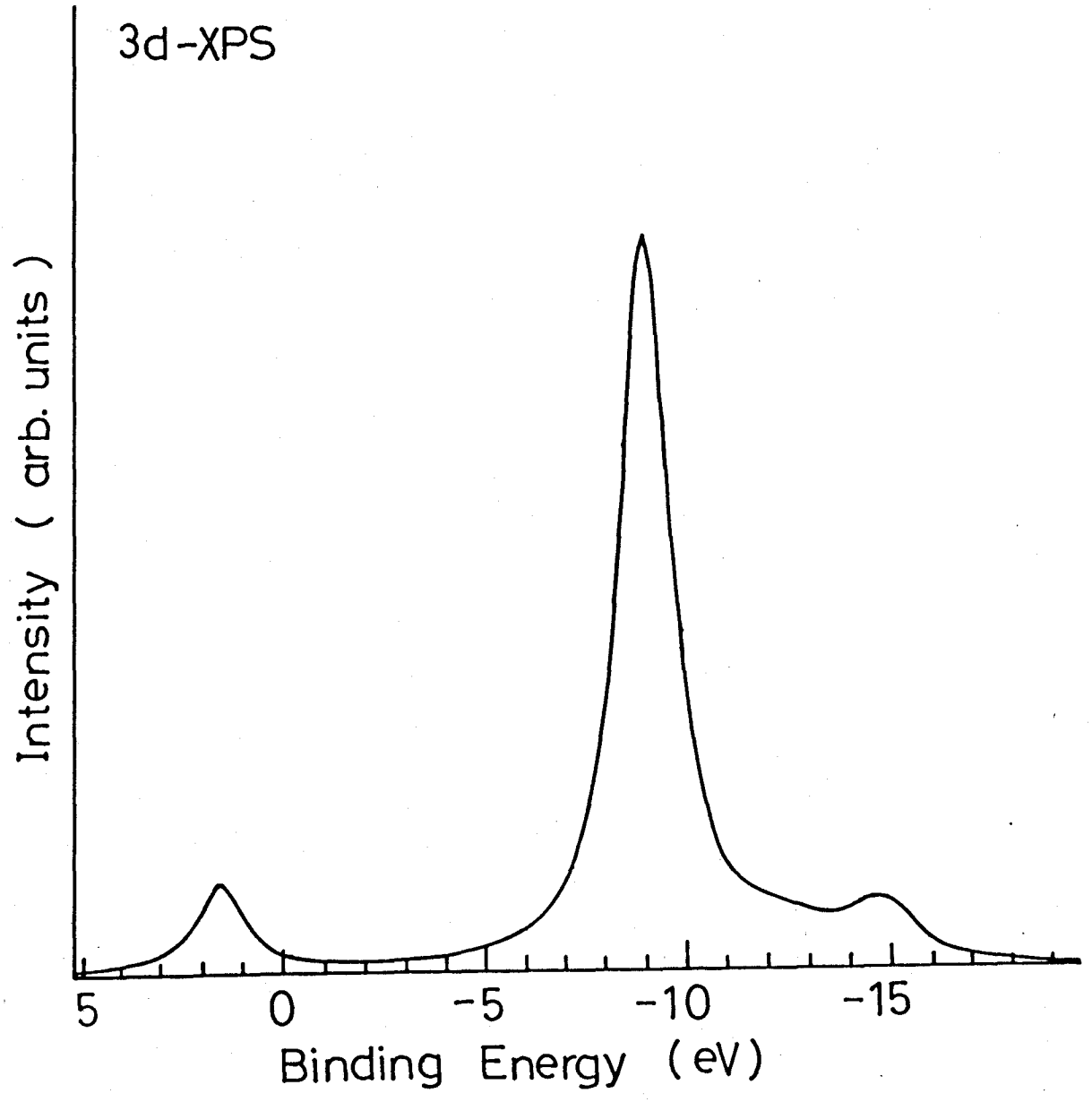
3d-XPS
Intensity ( arb. units )
5
0
-5
-10
-15
Binding Energy ( eV )

(a)

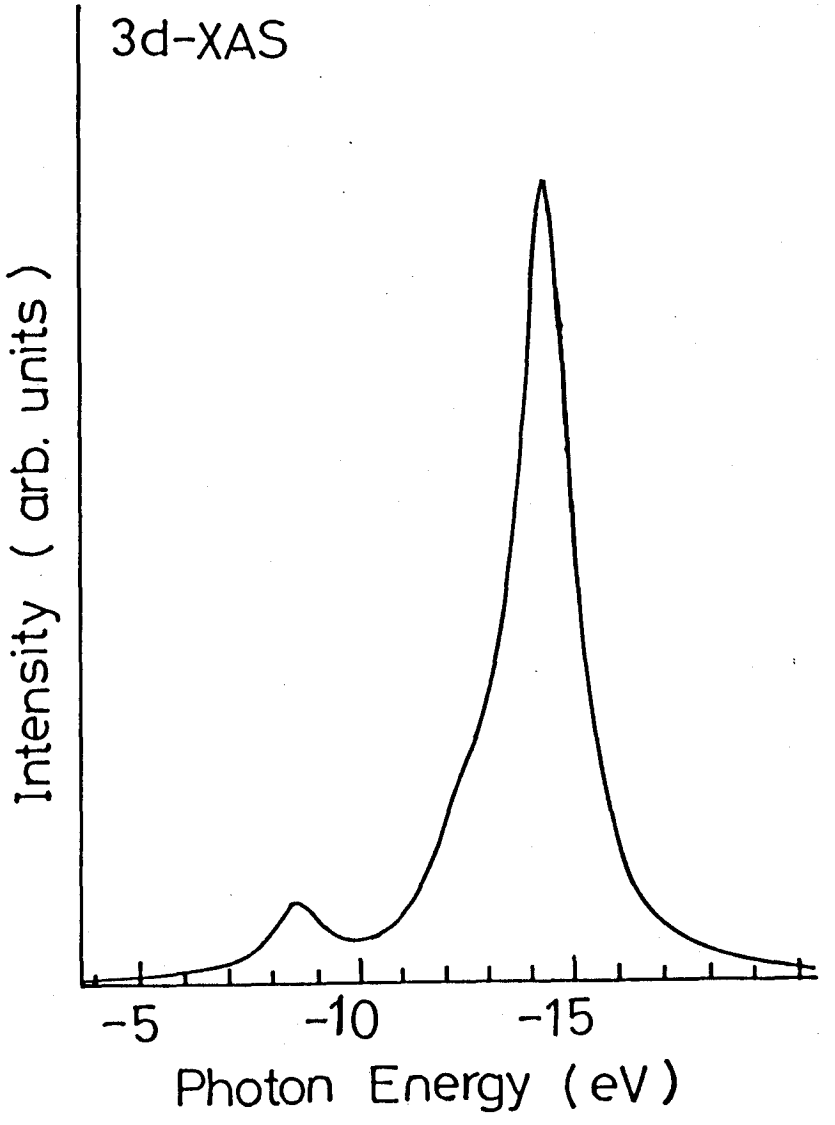
3d-XAS
Intensity ( arb. units )
-5
-10
-15
Photon Energy ( eV )

(b)

Fig. 22

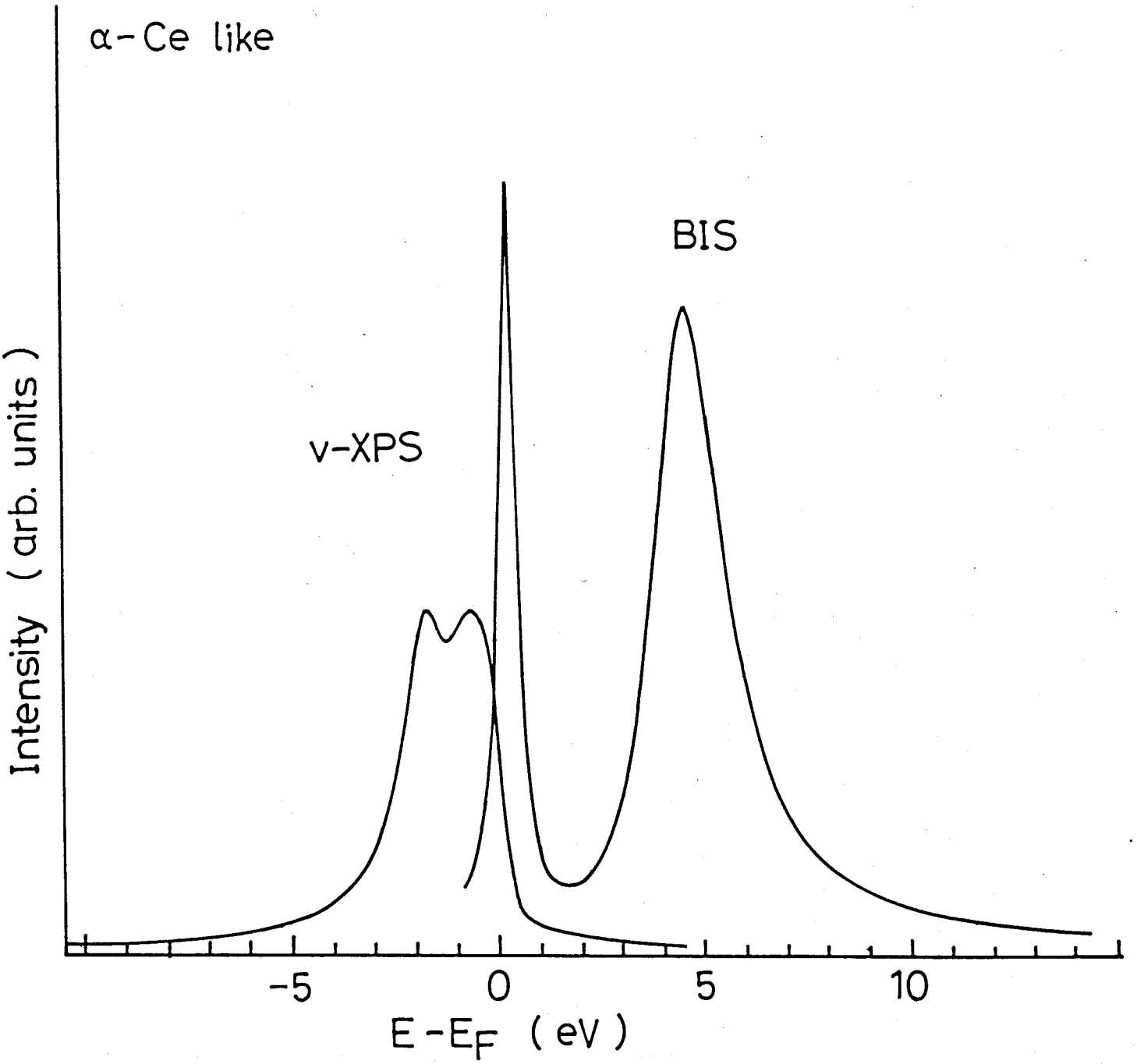


Fig.23

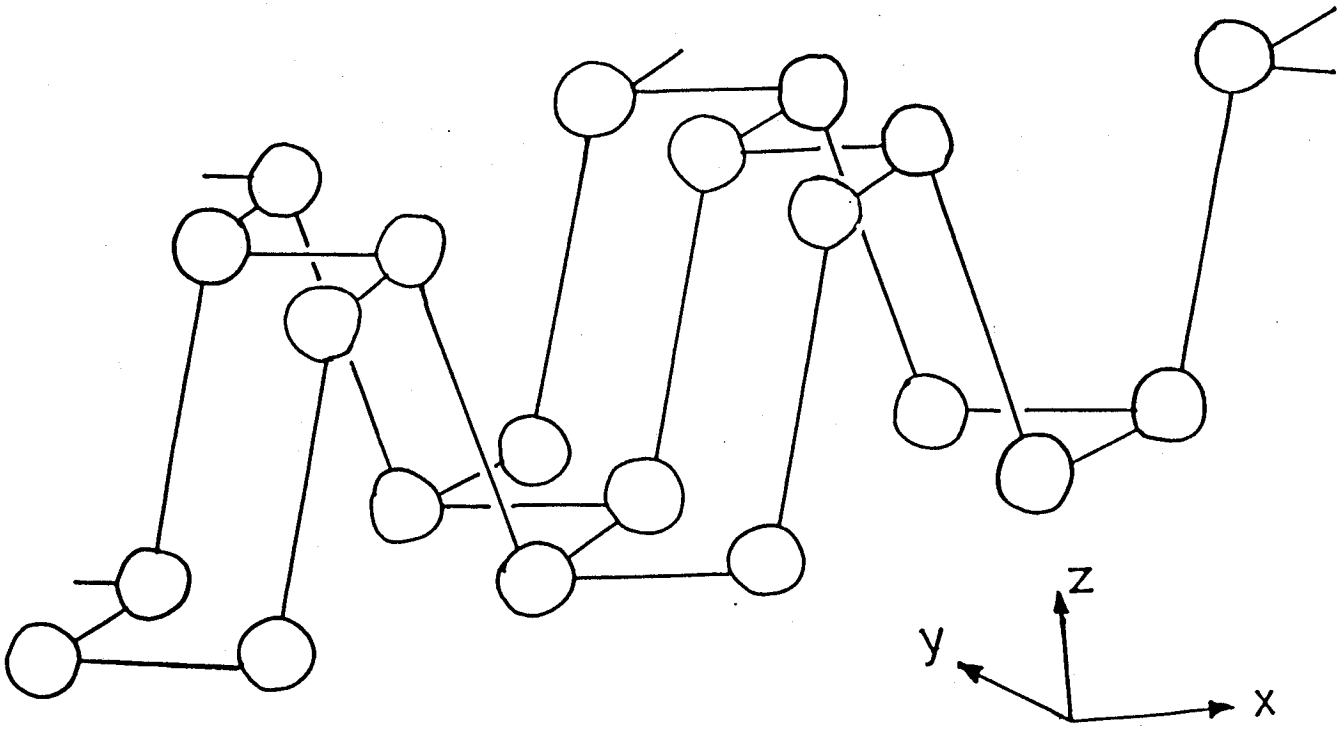


Fig.24

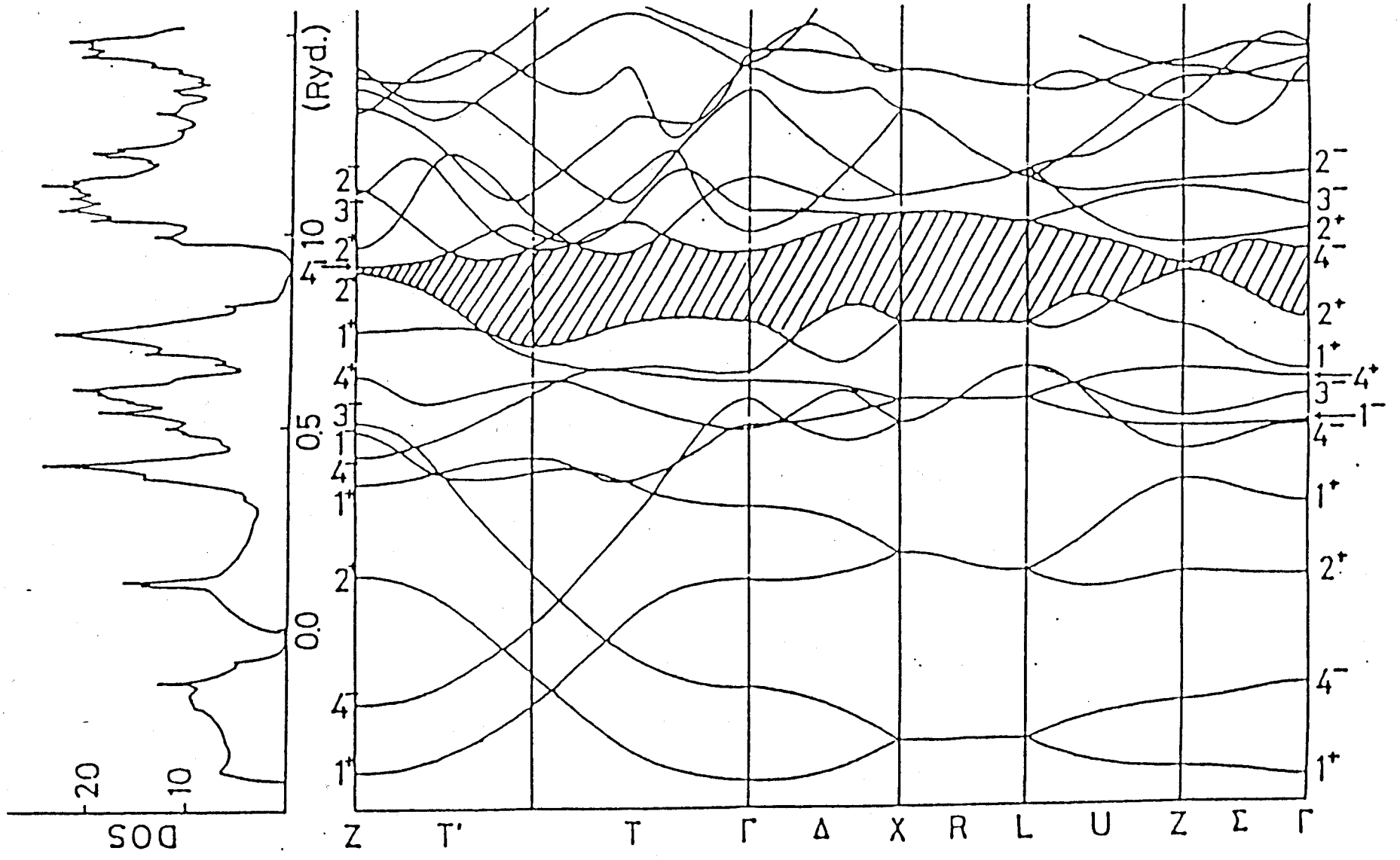
(Ryd.)
1.0
0.5
0.0
DOS
20
10
Z
T'
T
Γ
Δ
X
R
L
U
Z
Σ
Γ
2⁻
3⁻
2⁺
4⁻
2⁺
1⁺
4⁺
3⁻
1⁻
4⁻
1⁺
2⁺
4⁻
1⁺
2⁻
3⁻
2⁺
4⁻
2⁺
1⁺
4⁺
3⁻
1⁻
4⁻
1⁺
2⁺
4⁻
1⁺

Fig.25

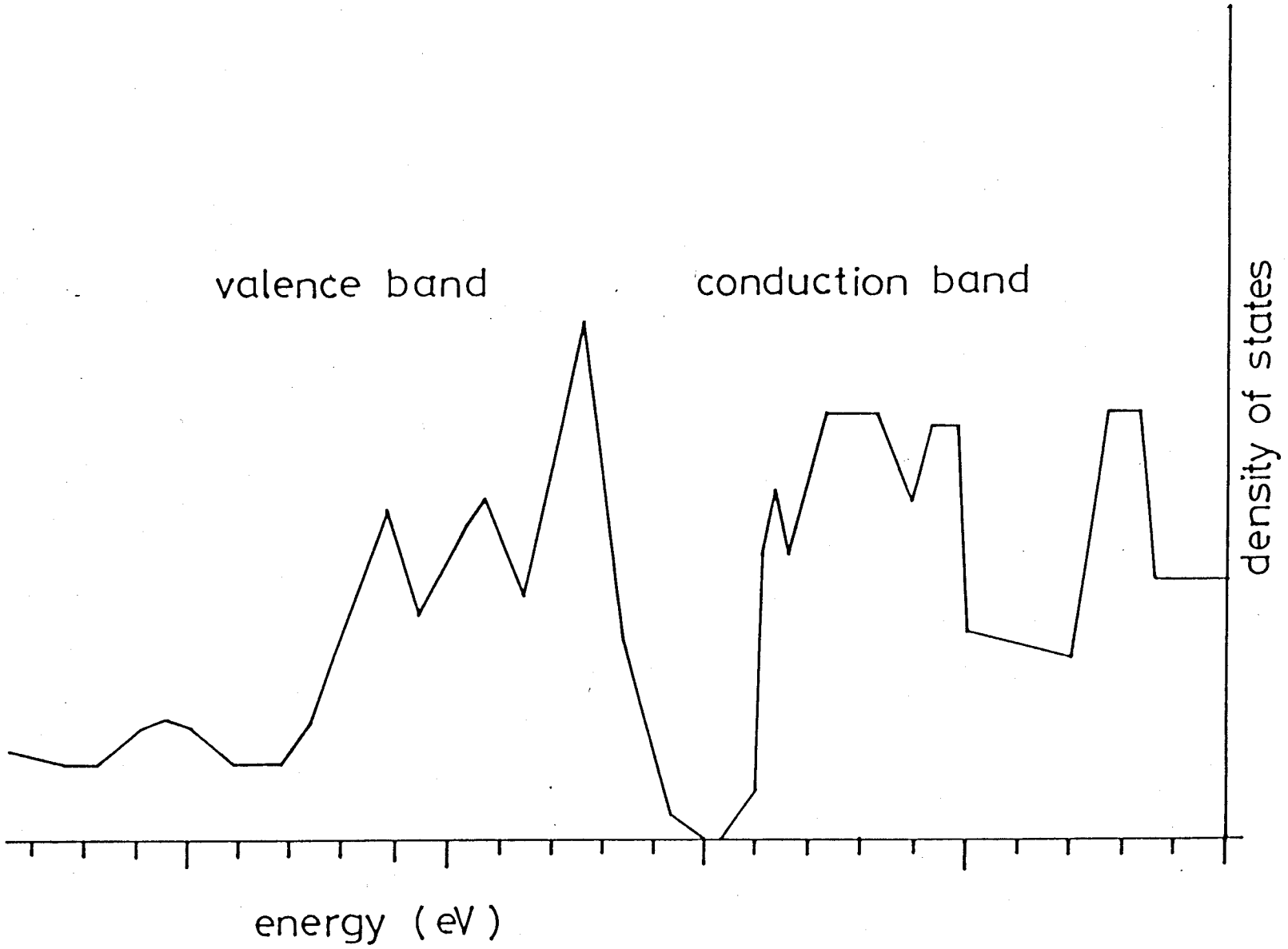


Fig.26

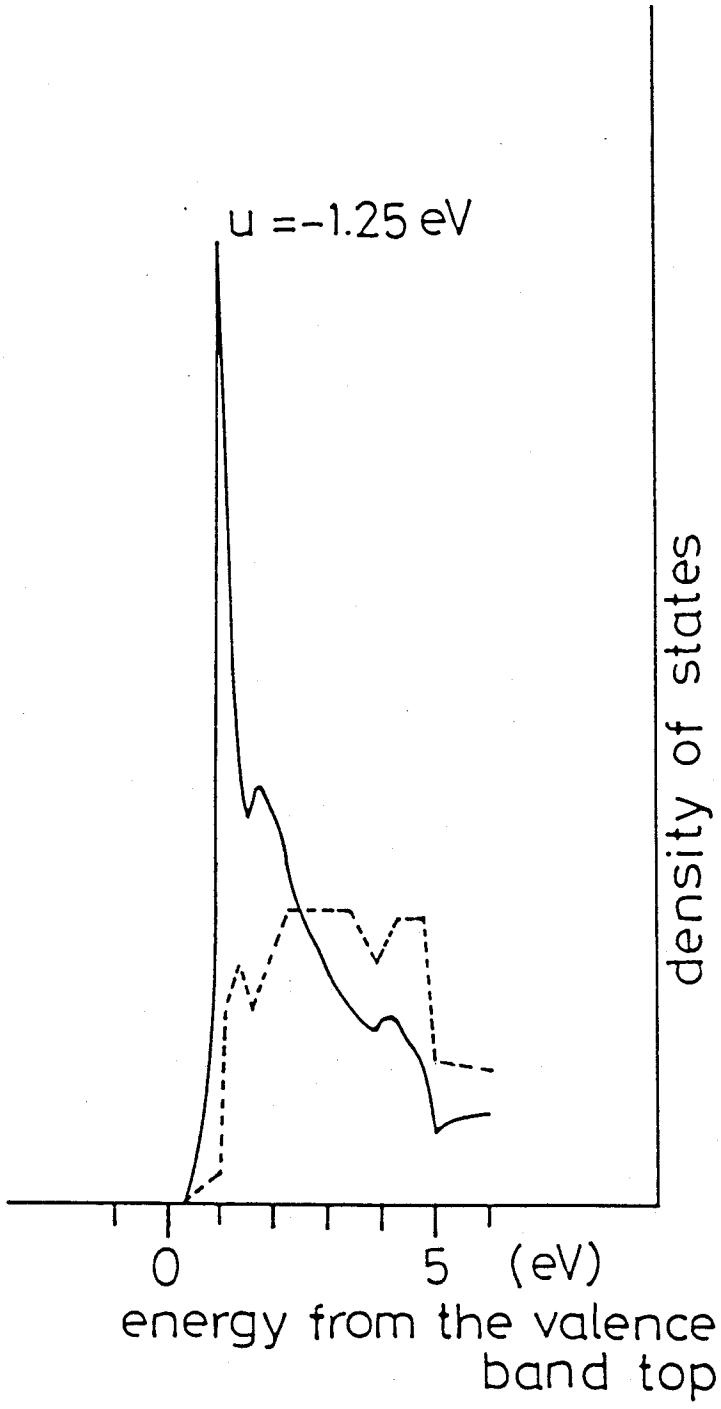
u =-1.25 eV
density of states
0
5
(eV)
energy from the valence band top

Fig.27

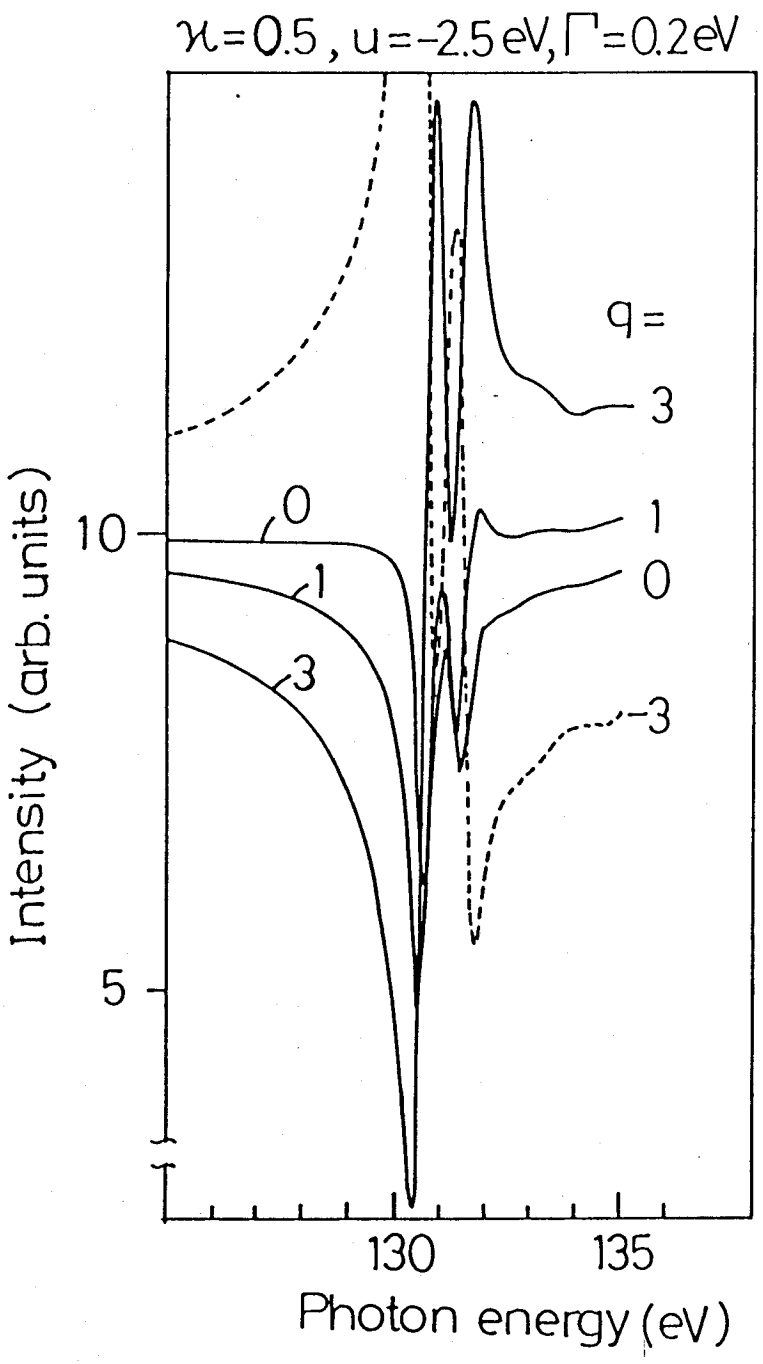
κ=0.5 , u=-2.5 eV, Γ=0.2eV
q=
3
0
1
0
-3
10
5
Intensity (arb. units)
130
135
Photon energy (eV)

(a)

Fig.28

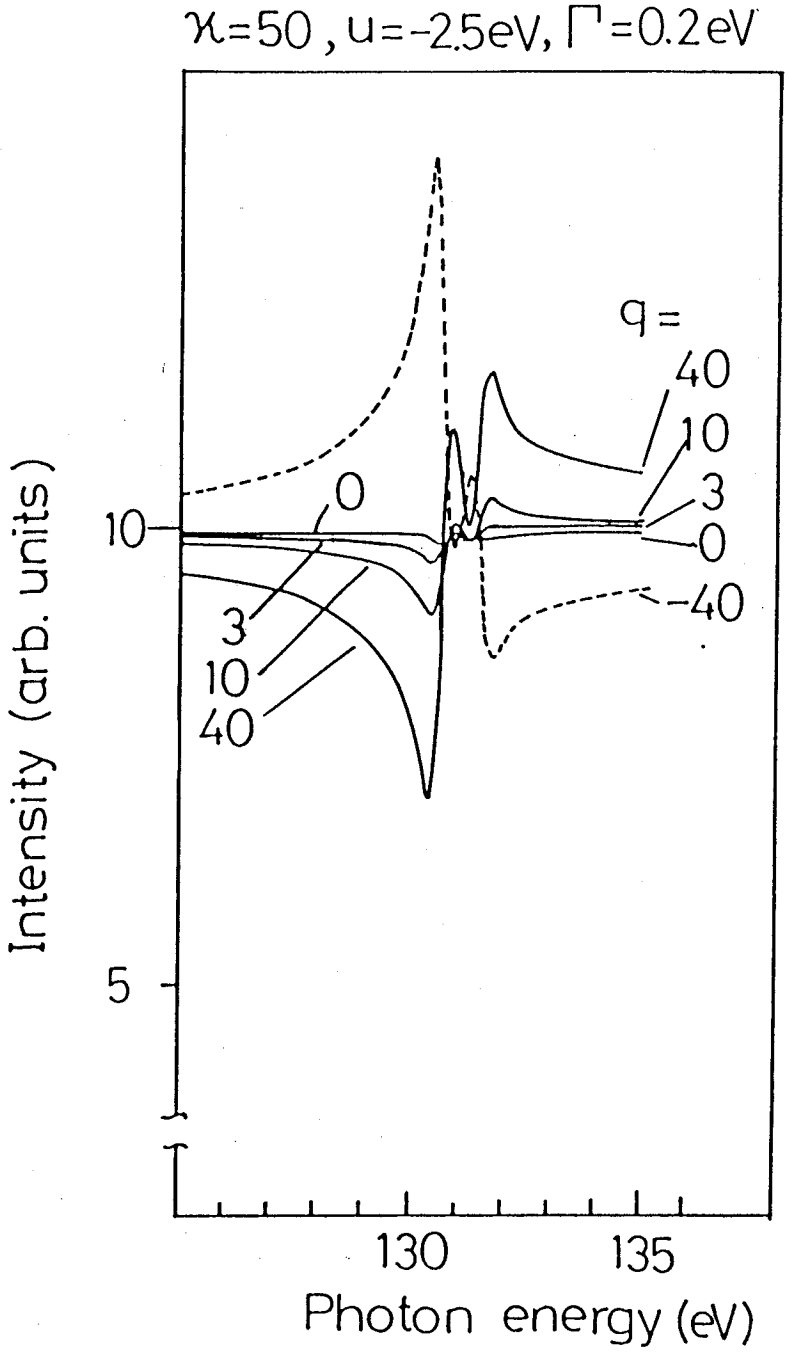
κ=50 , u=-2.5eV, Γ=0.2eV
q=
40
10
3
0
-40
10
5
Intensity (arb. units)
130
135
Photon energy (eV)

(b)

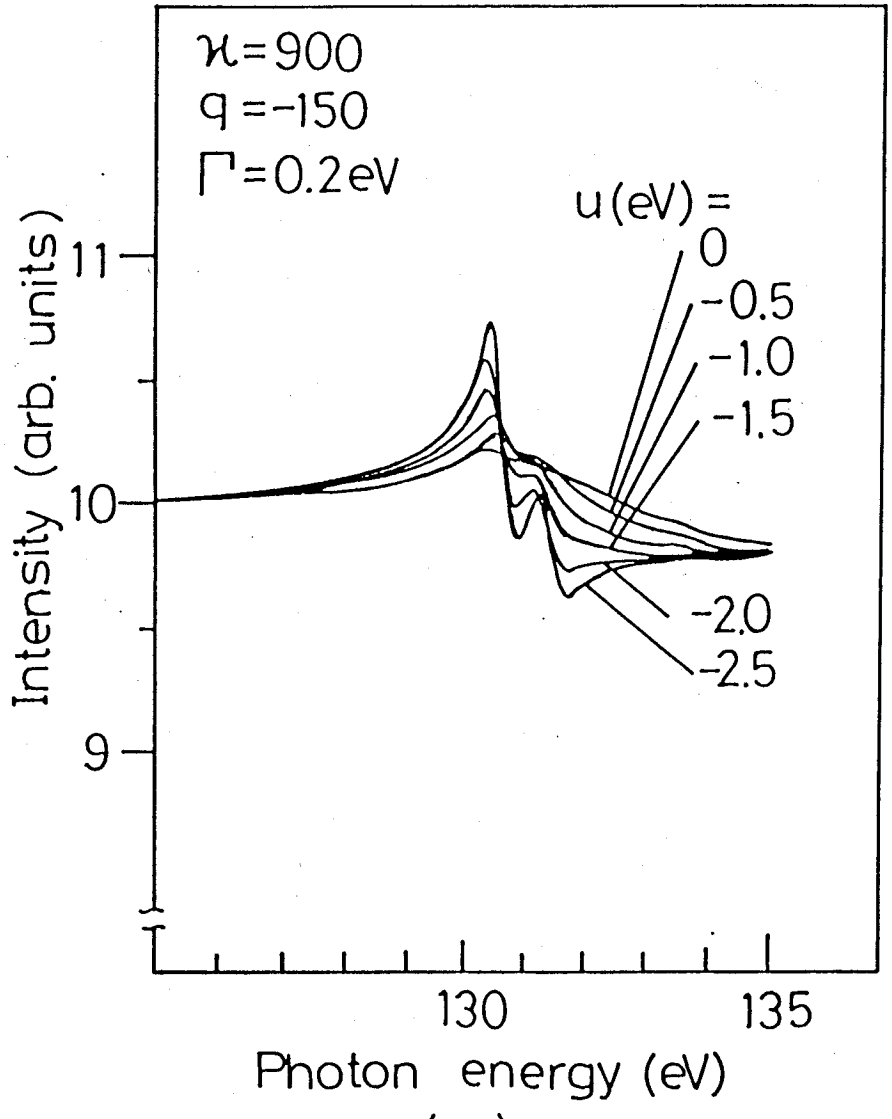
ϰ=900
q=-150
Γ=0.2eV
u(eV)=
0
-0.5
-1.0
-1.5
-2.0
-2.5
Intensity (arb. units)
11
10
9
130
135
Photon energy (eV)

( c )

Fig.28

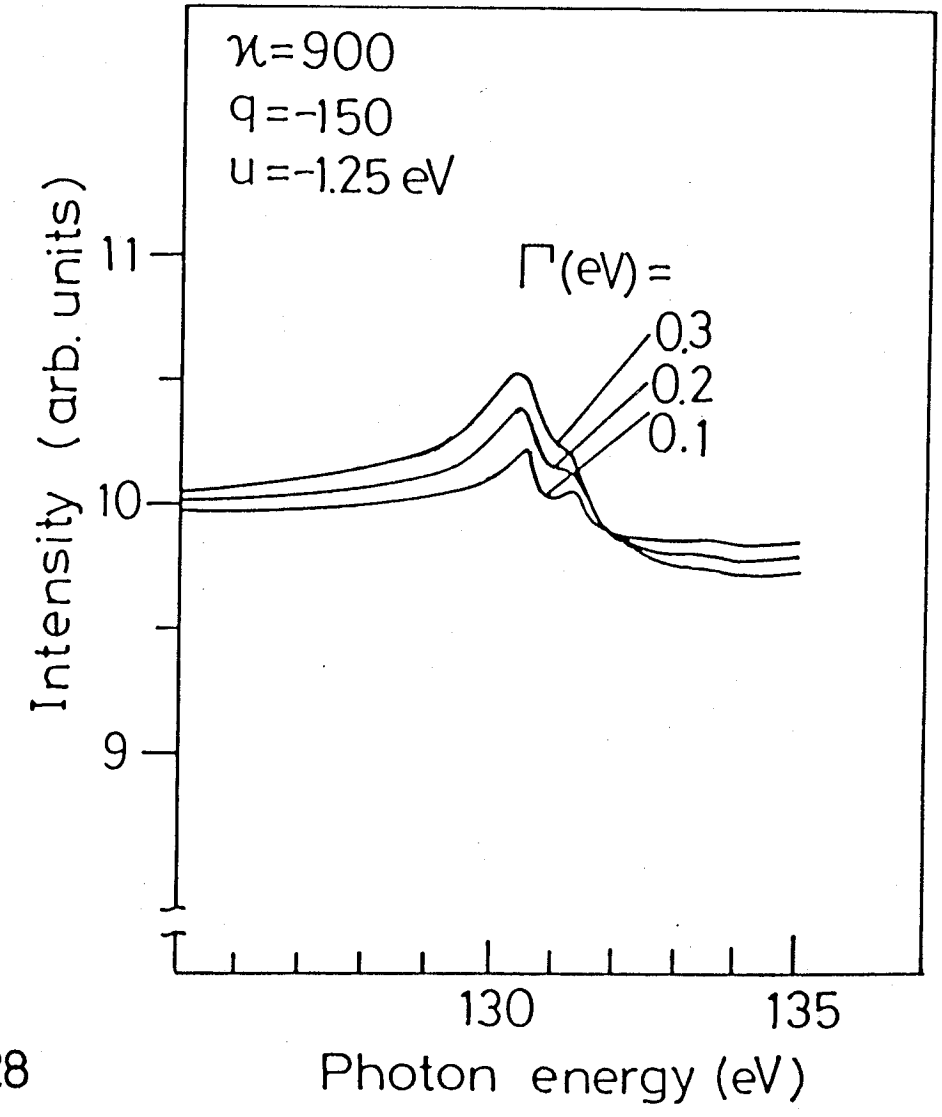
ϰ=900
q=-150
u=-1.25 eV
Γ(eV)=
0.3
0.2
0.1
Intensity (arb. units)
11
10
9
130
135
Photon energy (eV)

( d )

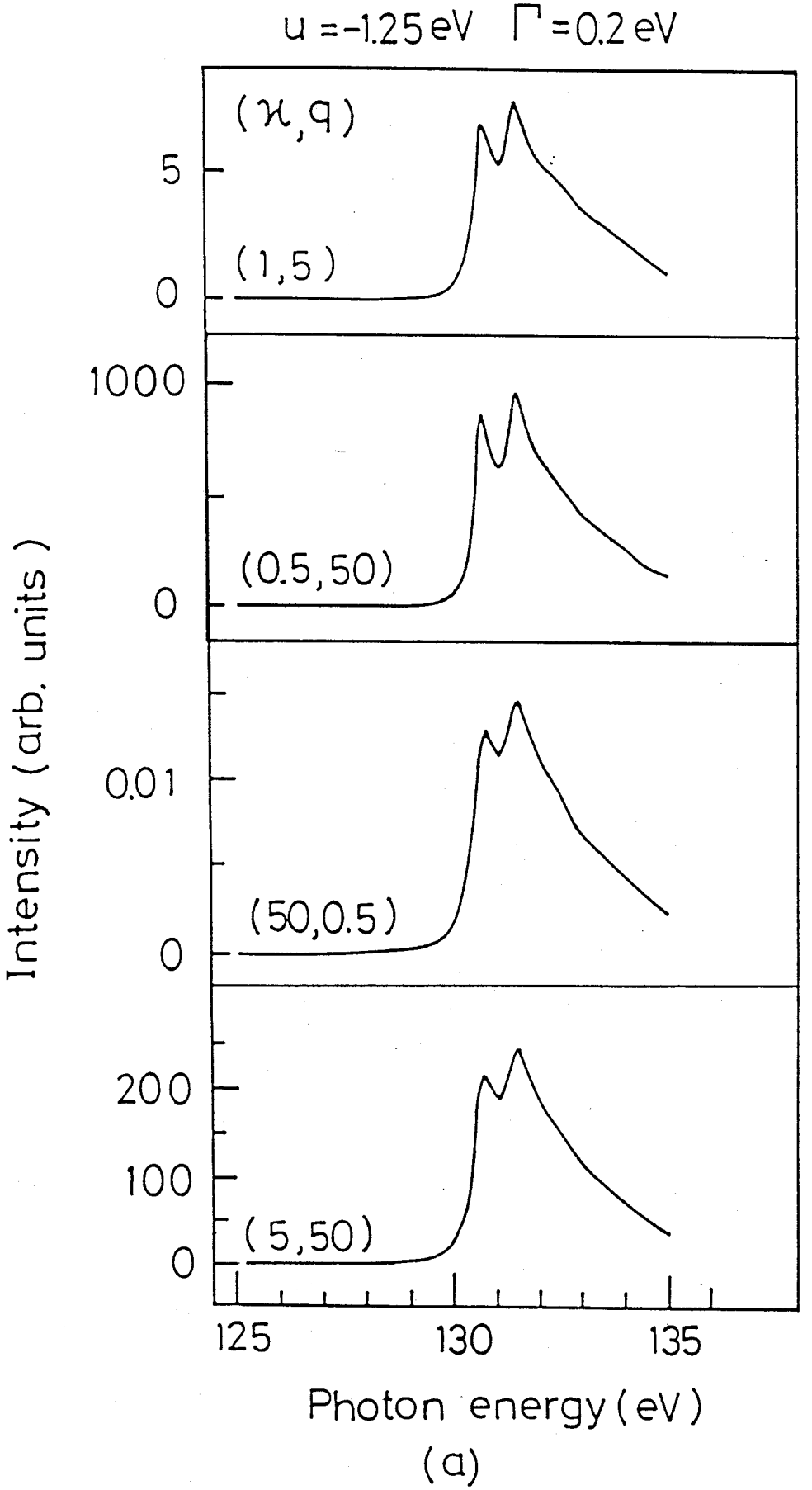
u =-1.25 eV Γ =0.2 eV
(ϰ,q)
5
(1,5)
0
1000
(0.5,50)
0
0.01
(50,0.5)
0
200
100
(5,50)
0
125
130
135
Photon energy (eV)
Intensity (arb. units)

(a)

Fig.29

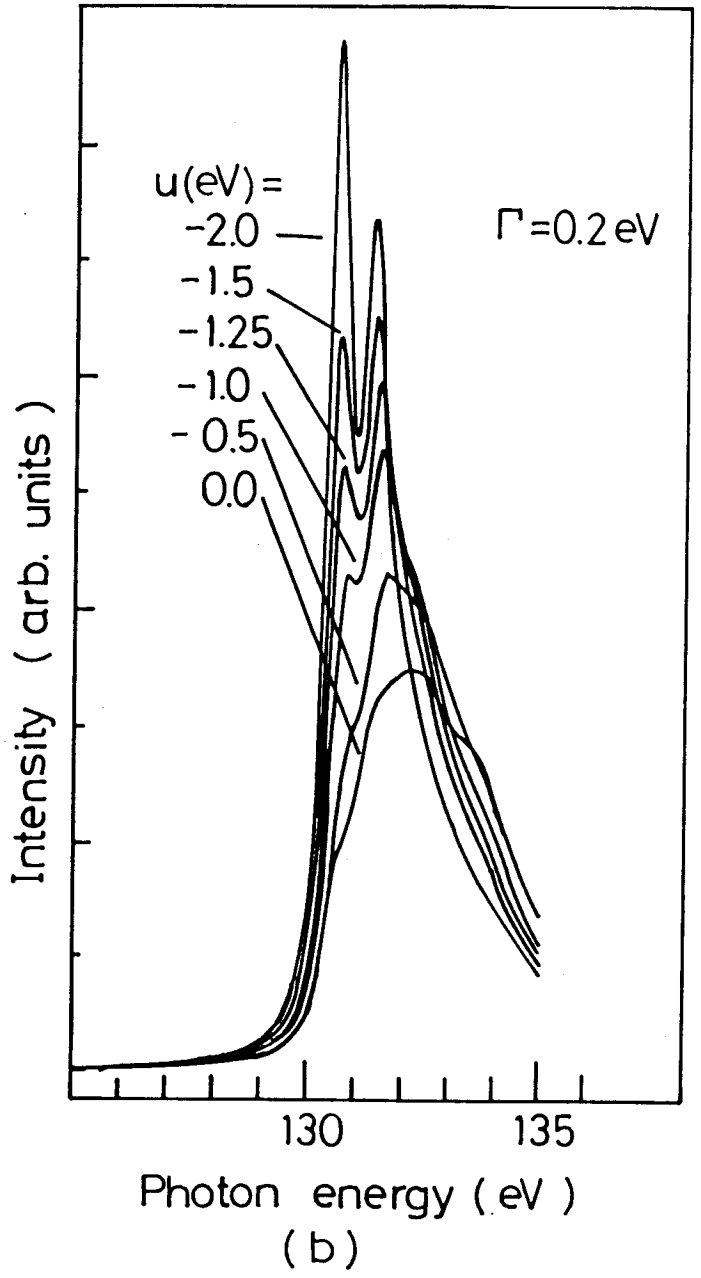
u(eV) =
-2.0
-1.5
-1.25
-1.0
-0.5
0.0
Γ=0.2 eV
Intensity ( arb. units )
130
135
Photon energy ( eV )
( b )

Fig. 29

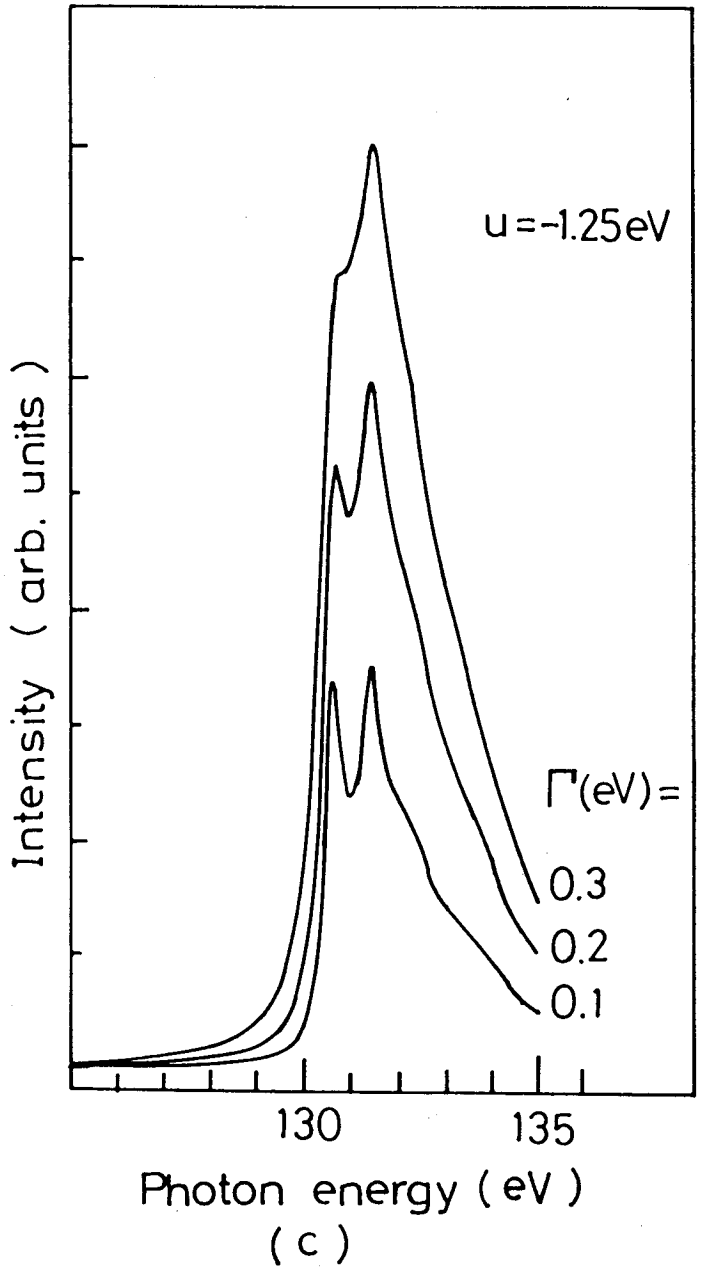
u=-1.25eV
Γ(eV) =
0.3
0.2
0.1
Intensity ( arb. units )
130
135
Photon energy ( eV )
( c )

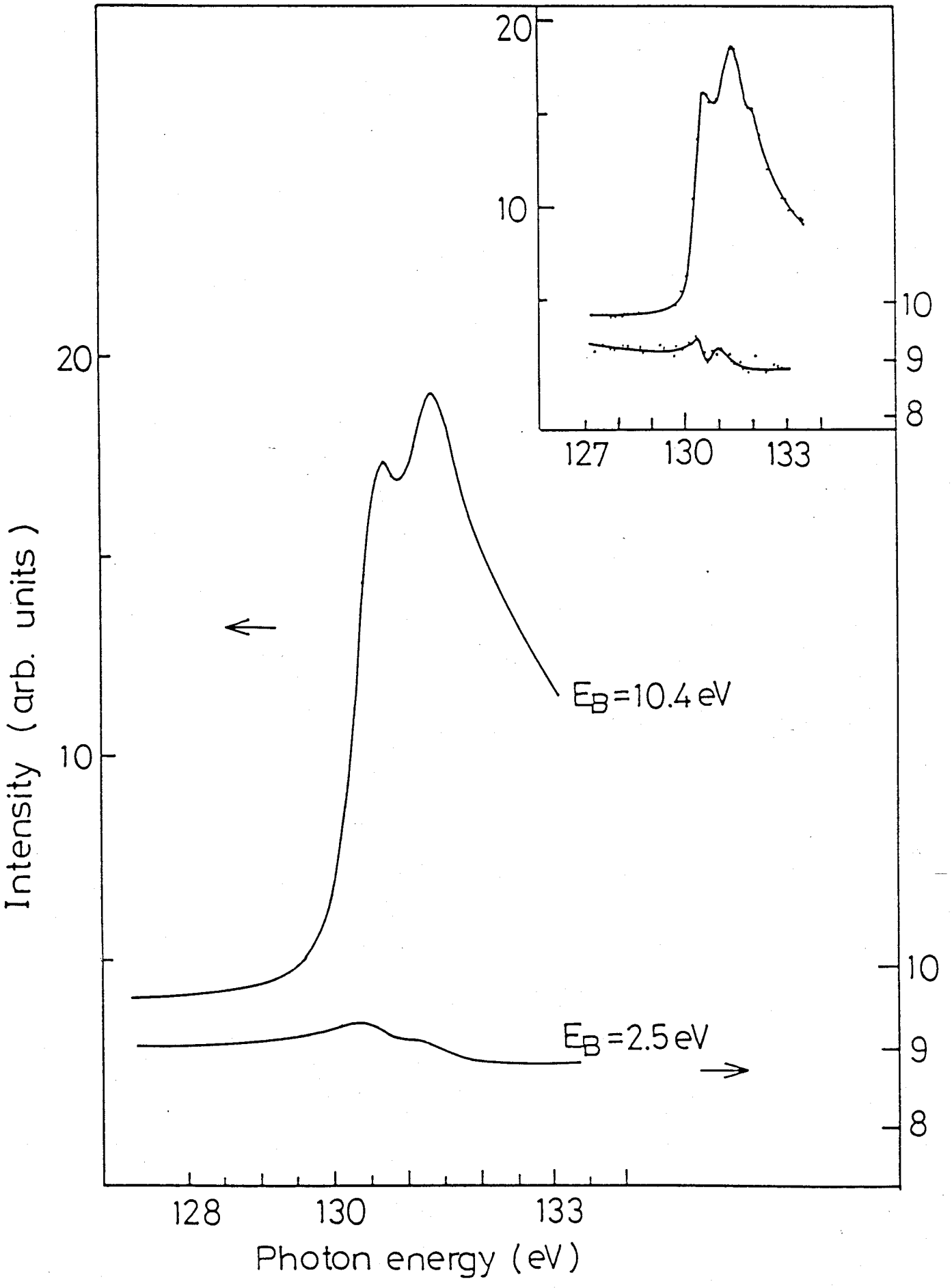
20
10
127
130
133
10
9
8
20
10
Intensity (arb. units)
$E_B$=10.4 eV
$E_B$=2.5 eV
10
9
8
128
130
133
Photon energy (eV)

Fig.30

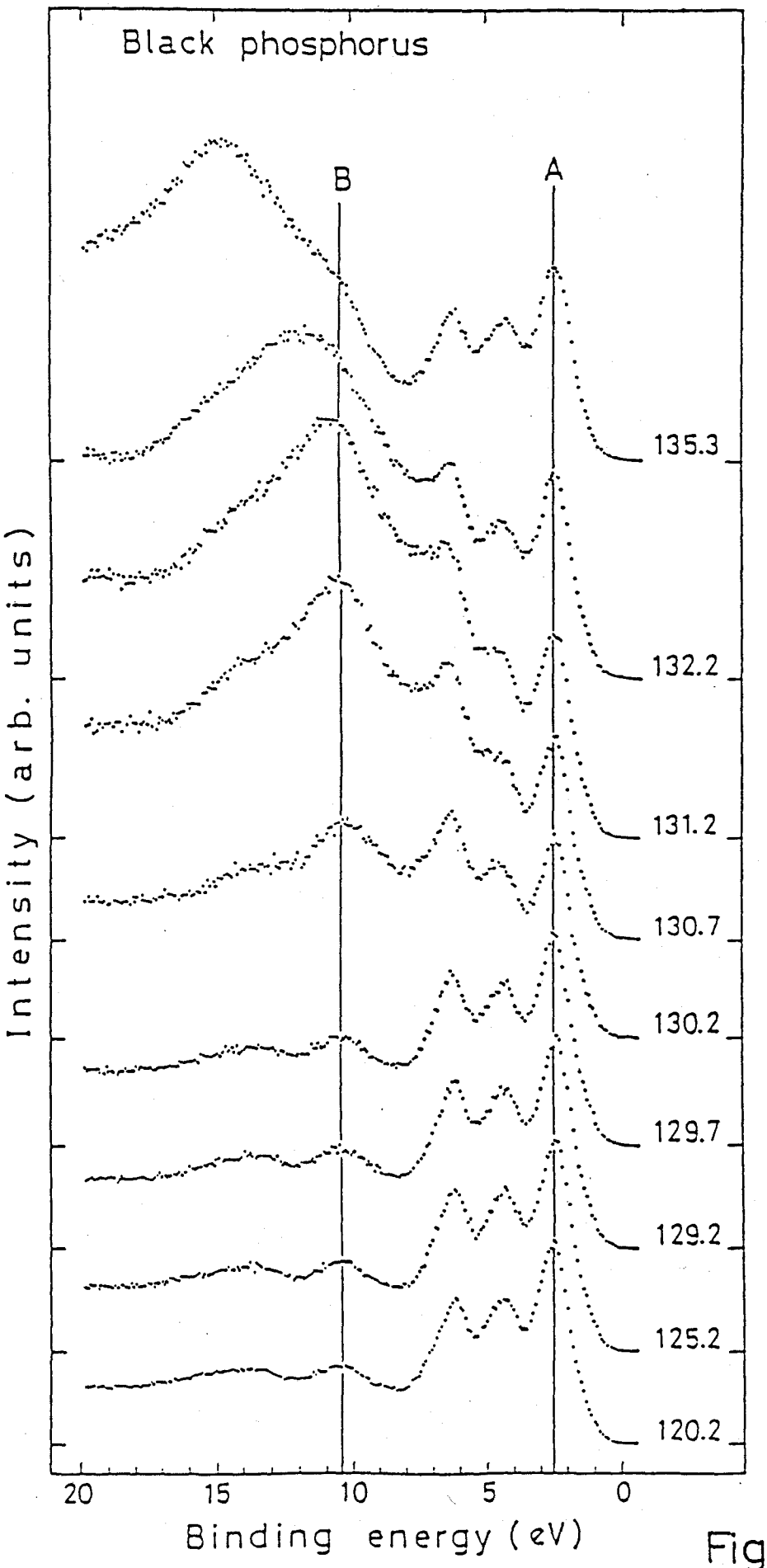
Black phosphorus
B
A
135.3
132.2
131.2
130.7
130.2
129.7
129.2
125.2
120.2
Intensity (arb. units)
20
15
10
5
0
Binding energy (eV)

Fig.31

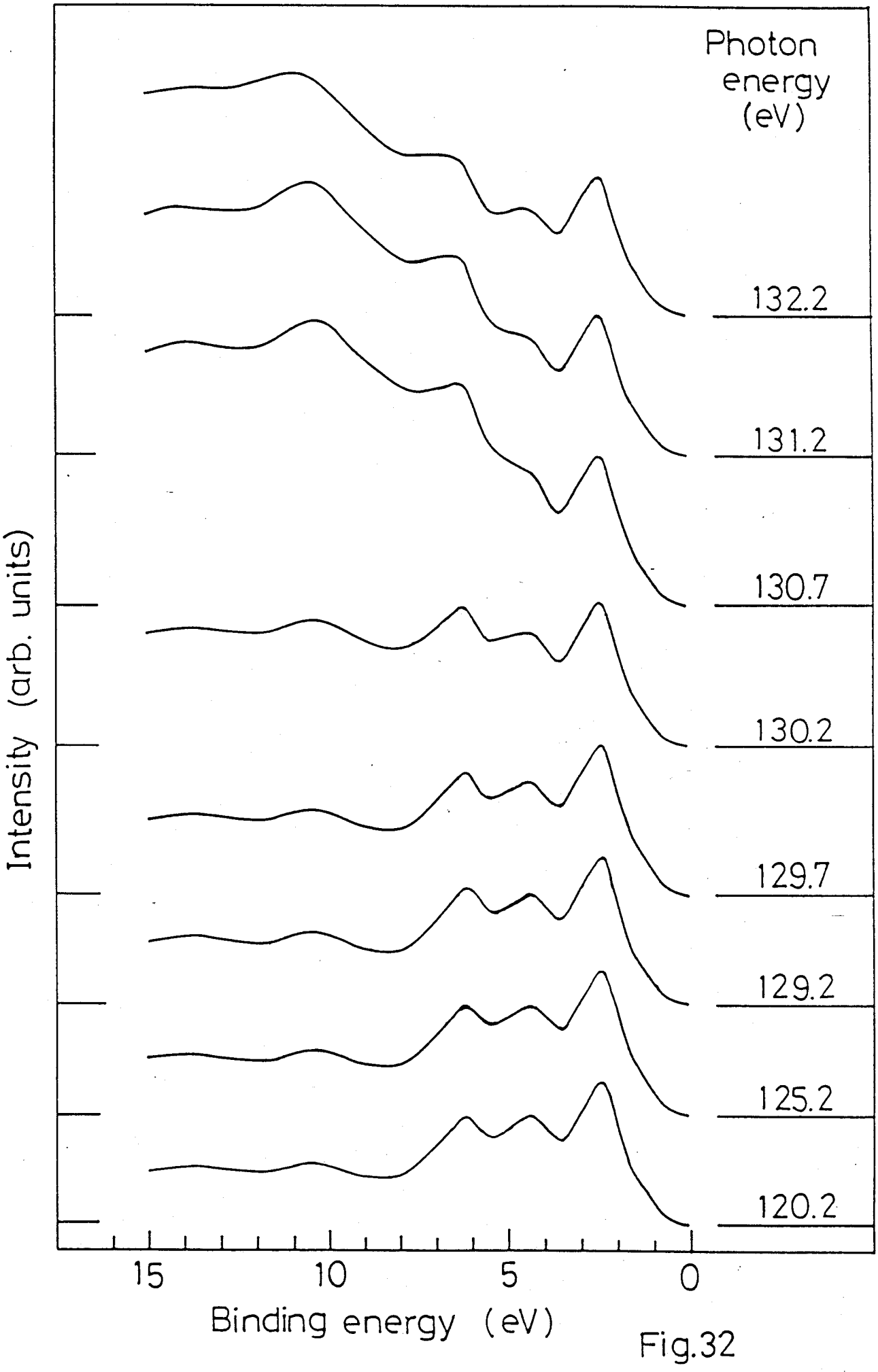
Photon energy (eV)
132.2
131.2
130.7
130.2
129.7
129.2
125.2
120.2
Intensity (arb. units)
15
10
5
0
Binding energy (eV)

Fig.32

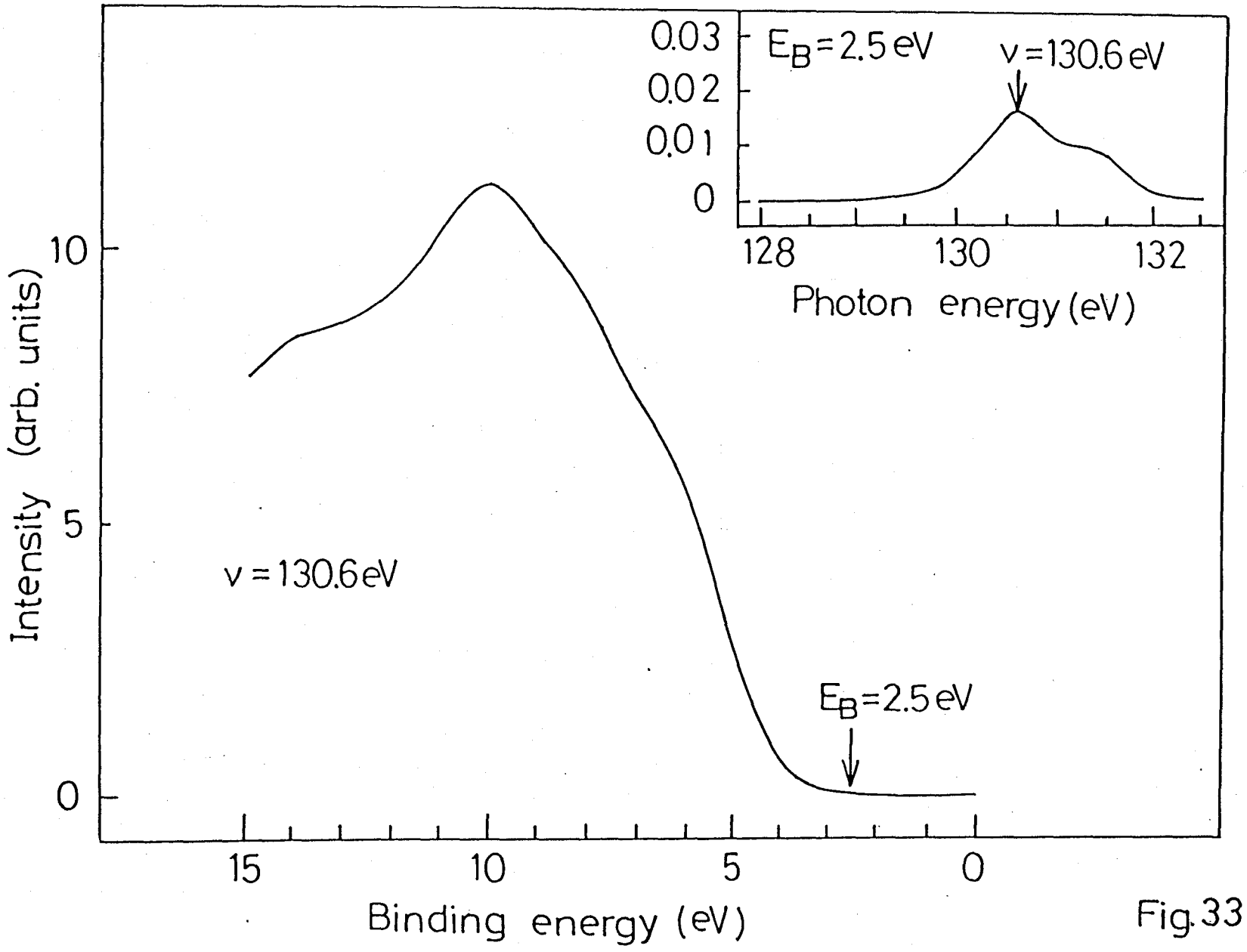
0.03
0.02
0.01
0
$E_B$ = 2.5 eV
ν = 130.6 eV
128
130
132
Photon energy (eV)
10
5
0
Intensity (arb. units)
ν = 130.6 eV
$E_B$ = 2.5 eV
15
10
5
0
Binding energy (eV)

Fig. 33

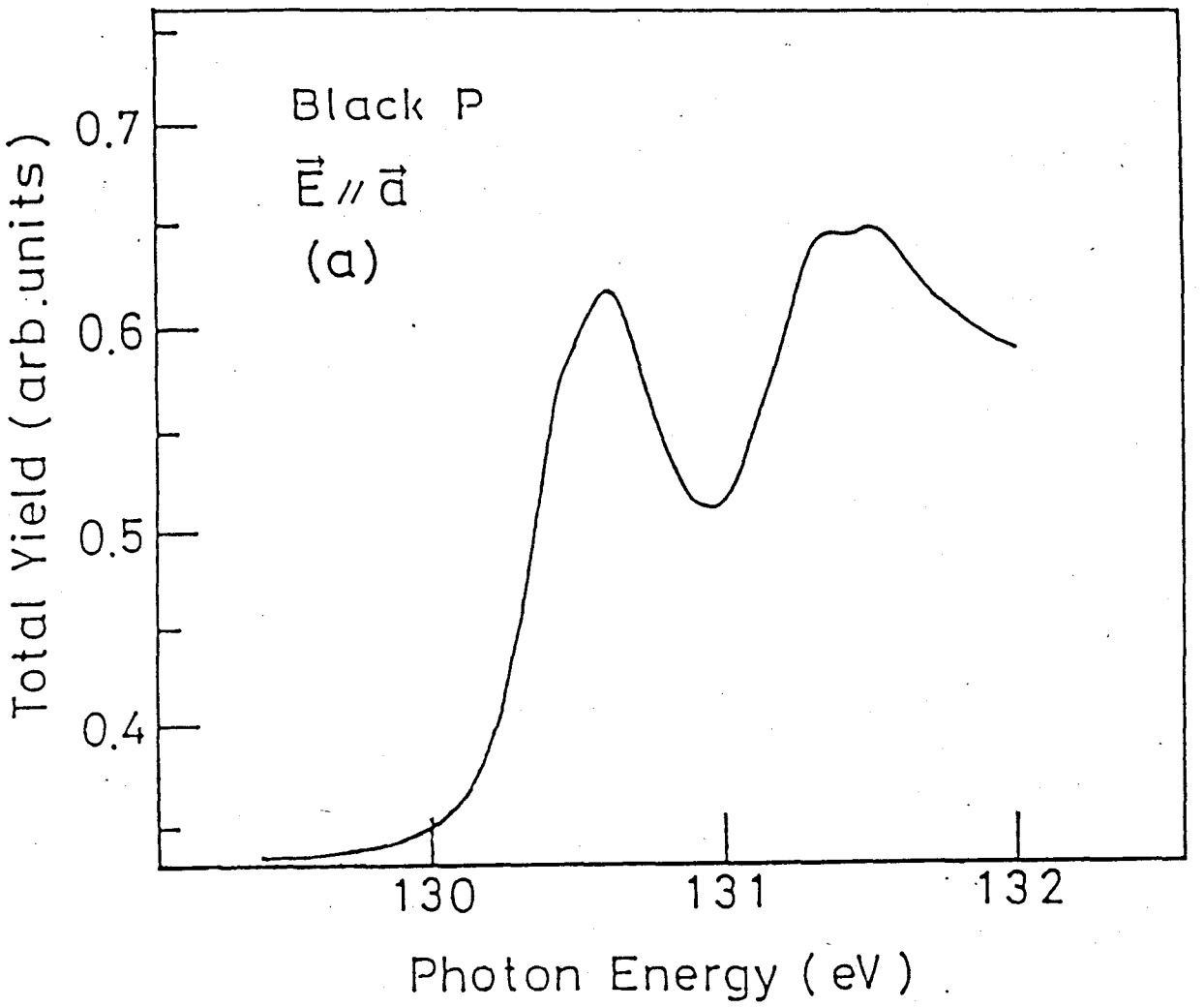
Black P
E // a
(a)
Total Yield (arb.units)
0.7
0.6
0.5
0.4
130
131
132
Photon Energy ( eV )

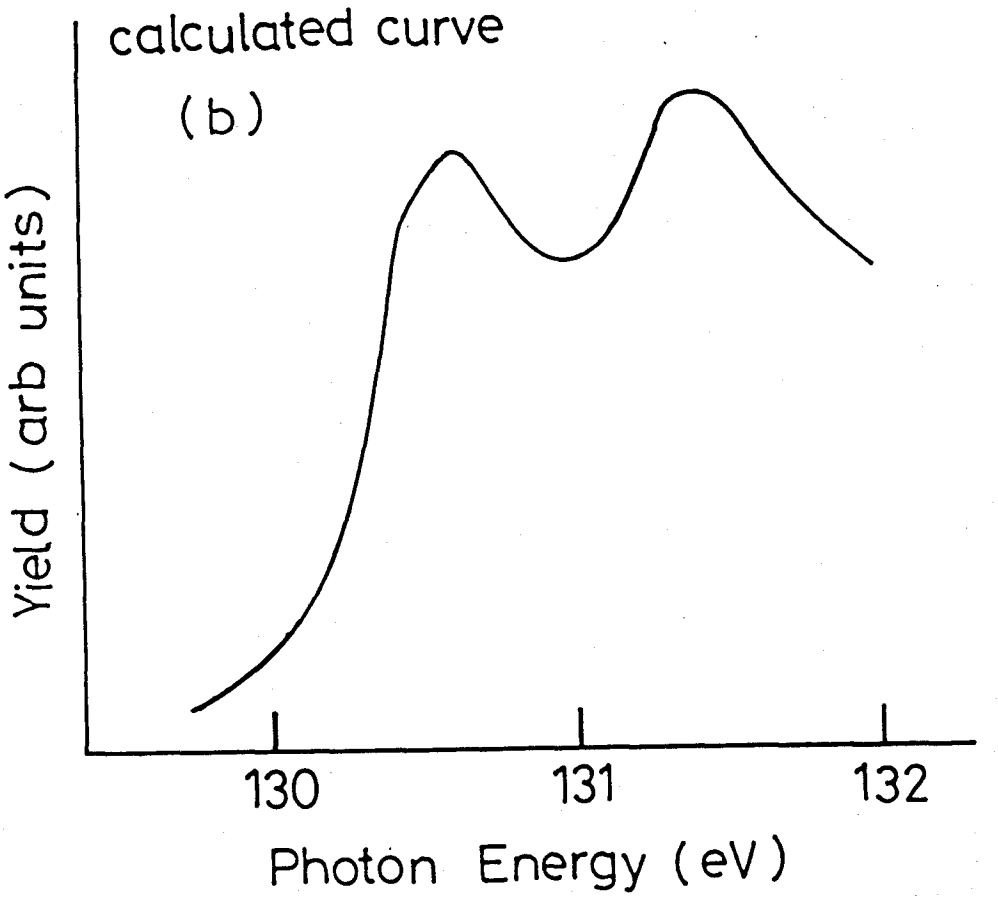
calculated curve
(b)
Yield (arb units)
130
131
132
Photon Energy (eV)

Fig. 34